

# Advanced Optimization of Organofunctionalized Silica Aerogels for Lightweight Insulations

Inaugural-Dissertation  
zur Erlangung des Doktorgrades  
der Mathematisch-Naturwissenschaftlichen Fakultät  
der Universität zu Köln



vorgelegt von  
M.Sc. Kai Steffens  
aus Mechernich

Köln, 2024

Die vorliegende Arbeit wurde von der Mathematisch-Naturwissenschaftlichen  
Fakultät der Universität zu Köln als Dissertation angenommen.

Berichterstatter: Prof. Dr. Barbara Milow  
Prof. Dr. Mathias S. Wickleder  
Vorsitzender: Prof. Dr. Elmar Behrmann  
Beisitzer: Dr. Danny Bialuschewski  
Tag der Promotion: 09.12.2024



*I have not failed. I've just found 10,000 ways that won't work.*

**Thomas Edison**



## Acknowledgment

An dieser Stelle möchte ich mich bei allen Personen und Institutionen bedanken, die durch ihre Unterstützung zum Gelingen der vorliegenden Arbeit beigetragen haben.

Zuallererst möchte ich mich bei Prof. Barbara Milow bedanken, die mir Durchführung dieser Arbeit überhaupt erst ermöglicht hat. Weiterhin bedanke ich mich für die fachliche Betreuung meiner Doktorarbeit, sowie für die stets hilfreichen fachlichen Diskussionen und Ideen, welche im wesentlichen zum Gelingen meiner Arbeit beigetragen haben.

Herrn Prof. Mathias Wickleder danke ich herzlich für die Übernahme des Zweitgutachtens.

Insbesondere bedanke ich mich bei meiner Mentorin Ass.-Prof. Andrea Heugenhauer, die mir in jeder Phase der Promotion für fachliche Diskussion, oder mit Hilfestellungen und Rat zur Seite stand.

Allen Kolleginnen und Kollegen der Abteilung Aerogele, allen voran Dr. Danny Bialuschewski, möchte ich für die angenehme Zusammenarbeit und die vielfachen Hilfestellungen und Unterstützung danken. Rebekka Probst danke ich für die Unterstützung bei den EDX und REM-Analysen und den wertvollen fachlichen Austausch hierzu. Lana Möltgen danke ich für die Durchführung der STA- und Partikelgrößen-Messungen. Auch möchte ich meinen zahlreichen damaligen Studenten für ihre Mithilfe zum Gelingen dieser Arbeit danken, hier insbesondere zu erwähnen ist Lara Albrecht.

Ich danke Frau Prof. Annette Schmidt und ihrem Team, insbesondere Benoît Rhein und Patricia Bach, für die Bereitstellung der Universalprüfmaschine und die Anleitung der Versuche an dieser.

Der größte Dank geht an meine Lebensgefährtin Hannah, meine Eltern sowie an meine Freunde, die mir über die gesamte Dauer meiner Promotion den Rücken freigehalten haben, mich ermutigt haben, und mich vom Arbeitsalltag abgelenkt haben.





## Abstract

Organic-inorganic hybrid-silica aerogels can be made of methyltrimethoxysilane (MTMS,  $\text{CH}_3\text{Si}(\text{OCH}_3)_3$ ) and dimethyldimethoxysilane (DMDMS,  $\text{Si}(\text{OCH}_3)_2(\text{CH}_3)_2$ ) in a typical sol-gel process yielding flexible and hydrophobic structures. They possess a low density, thermal conductivity, and high sound absorption, all a result of their highly nanostructured porous network, and are ideal candidates for lightweight insulation applications. Their synthesis depends on several fundamental parameters. One of these is the precursor-to-water ratio, which can be modified during the sol-gel process. With appropriate variation, the density of the final aerogel product can be systematically controlled, thus influencing the final aerogel properties. The incorporation of a fiber matrix exhibited improved stability and handling while maintaining lightweight properties. A flame-retardant agent (vinylphosphonic acid, VPA), chemically bound to the aerogel network *via* thiol-ene click reaction at the introduced VTMS (which partially substituted MTMS), was implemented to enhance fire resistance. This modification increased the fire resistance but also led to a higher density, an increase in thermal conductivity, and a loss of flexibility. A reduction in the proportion of VTMS and lower quantities of the flame retardant VPA were identified as future optimization potential. The synthesis of flexible hybrid-silica aerogel particles using emulsion technology was investigated. In this process, VTMS could be successfully integrated up to a proportion of 50%, which offers the potential for further functionalization. The produced particles exhibited densities of about  $0.05 \text{ g/cm}^3$ , which is less than half the density of monolithic reference samples, while still retaining a remarkable insulation performance. The inclusion of commercially available hydrophobic, highly insulating silica particles (Cabot ENOVA<sup>®</sup> IC3110) as fillers should result in silica aerogel-aerogel composites with lower thermal conductivities than their respective monoliths. Other than expected, this led to increased densities and thermal conductivities due to the collapse of the particles during the drying process. The resulting aerogels and composites have been carefully investigated regarding their density, microstructure, and surface chemistry by various characterization techniques, such as helium pycnometry, scanning electron imaging, water drop shape analysis, thermogravimetric/simultaneous thermal analysis, and spectroscopic methods, *e.g.*, energy-dispersive x-ray spectroscopy and solid-state nuclear magnetic resonance spectroscopy. The thermal conductivity was measured by transient-/steady-state methods and acoustic properties by an acoustic tube. The mechanical characteristics were investigated by uniaxial compression tests. The samples' reaction to fire was measured with a self-build test. Particle sizes were analyzed with a particle size analyzer and *via* digital microscopy.

## Kurzzusammenfassung

Organisch-anorganische Hybrid-Silica-Aerogele können aus Methyltrimethoxysilan (MTMS,  $\text{CH}_3\text{Si}(\text{OCH}_3)_3$ ) und Dimethyldimethoxysilan (DMDMS,  $\text{Si}(\text{OCH}_3)_2(\text{CH}_3)_2$ ) in einem typischen Sol-Gel-Verfahren hergestellt werden, das zu flexiblen und hydrophoben Strukturen führt. Sie besitzen eine niedrige Dichte, Wärmeleitfähigkeit und hohe Schallabsorption, die alle auf ihr stark nanostrukturiertes poröses Netzwerk zurückzuführen sind, und sind ideale Kandidaten für leichte Isolationsanwendungen. Die Synthese hängt von mehreren grundlegenden Parametern ab: Einer davon ist das Verhältnis von Präkursor zu Wasser, das während des Sol-Gel-Prozesses leicht verändert werden kann. Bei entsprechender Variation kann die Dichte des fertigen Aerogel-Produkts systematisch gesteuert werden, wodurch die endgültigen Eigenschaften des Aerogels beeinflusst werden. Durch den Einbau einer Fasermatrix wurden die Stabilität und die Handhabung verbessert, während die Leichtbaueigenschaften erhalten blieben. Ein Flammenschutzmittel (Vinylphosphonsäure, VPA), das über eine Thiol-En-Klick-Reaktion am eingebrachten VTMS (welches MTMS teilweise ersetzt) chemisch an das Aerogel-Netzwerk gebunden ist, wurde zur Verbesserung der Feuerbeständigkeit eingesetzt. Diese Modifikation führte aber auch zu einer höheren Dichte, einem Anstieg der Wärmeleitfähigkeit und einem Verlust an Flexibilität. Eine Verringerung des VTMS-Anteils und geringere Mengen des Flammenschutzmittels VPA wurden als zukünftiges Optimierungspotenzial identifiziert. Die Synthese von flexiblen Hybrid-Silica-Aerogel-Partikeln mittels Emulsionstechnologie wurde untersucht. Dabei konnte VTMS ebenfalls bis zu einem Anteil von 50% erfolgreich integriert werden, was das Potenzial für eine weitere Funktionalisierung bietet. Die hergestellten Partikel wiesen Dichten von ca.  $0,05 \text{ g cm}^{-3}$  auf, was weniger als die Hälfte der Dichte von monolithischen Referenzproben ist, wobei sie ihre bemerkenswerte Isolationsleistung beibehalten. Die Verwendung handelsüblicher, hydrophober und hochisolierender Silica-Partikel (Cabot ENOVA® IC3110) als Füllstoffe sollte zu Silica-Aerogel-Aerogel-Verbundwerkstoffen mit niedrigeren Wärmeleitfähigkeiten als die entsprechenden Monolithen führen. Anders als erwartet, führte dies zu höheren Dichten und Wärmeleitfähigkeiten, da die Partikel während des Trocknungsprozesses kollabierten. Die entstandenen Aerogele und Komposite wurden hinsichtlich ihrer Dichte, Mikrostruktur und Oberflächenchemie mit verschiedenen Charakterisierungstechniken wie Helium-Pyknometrie, Rasterelektronenmikroskopie, Wasser-Kontaktwinkelanalyse, thermogravimetrische/simultane thermische Analyse und spektroskopische Methoden, z. B. energiedispersive Röntgenspektroskopie und Festkörper-Kernresonanzspektroskopie, sorgfältig untersucht. Die Wärmeleitfähigkeit wurde mit Transienten-/Stationärmethoden und die akustischen Eigenschaften mit einem Schallrohr gemessen. Die mechanischen Eigenschaften wurden durch

einachsige Druckversuche untersucht. Das Brandverhalten der Proben wurde mit einem eigens entwickeltem Versuchsaufbau gemessen und verglichen. Die Partikelgrößen wurden mit einem Partikelgrößenanalysator und mittels digitaler Mikroskopie analysiert.



# Table of Contents

<b>1</b>	<b>Introduction .....</b>	<b>1</b>
<b>2</b>	<b>State of the Art.....</b>	<b>4</b>
2.1	Aerogels: From Synthesis to Application.....	4
2.1.1	Sol-Gel Process .....	4
2.1.2	Drying of Wet Gels.....	6
2.1.3	Aerogel Applications.....	7
2.2	Hybrid-Silica Aerogels .....	8
2.2.1	Synthesis.....	9
2.2.2	Functionalization .....	10
2.2.3	Materials and Structures .....	12
2.2.3.1	Monoliths .....	12
2.2.3.2	Fiber-Matrix Composites .....	13
2.2.3.3	Aerogel-Aerogel Composites .....	13
2.2.3.4	Aerogel Particles .....	14
2.2.4	Properties.....	15
2.2.4.1	Mechanical Behavior.....	16
2.2.4.2	Thermal Conductivity .....	16
2.2.4.3	Acoustic Performance .....	17
2.2.4.4	Hydrophobicity.....	18
2.2.4.5	Reaction to Fire .....	18
2.3	Thermal- and Acoustic Insulation Materials .....	19
2.3.1	Thermal Insulation .....	20
2.3.2	Acoustic Insulation.....	22
2.3.3	Commercial Products .....	25
<b>3</b>	<b>Results and Discussion .....</b>	<b>27</b>
3.1	Dilution of Precursors .....	28
3.1.1	Pure Aerogels .....	28
3.1.1.1	Density, Microstructure, and Surface Chemistry .....	28
3.1.1.2	Thermal Properties .....	31
3.1.1.3	Mechanical Properties .....	32
3.1.1.4	Sound Insulation Properties .....	34
3.1.2	Aerogel Composites .....	36
3.1.2.1	Density, Microstructure, and Surface Chemistry .....	36

3.1.2.2	Thermal Properties .....	39
3.1.2.3	Mechanical Properties .....	39
3.1.2.4	Sound Insulation Properties .....	40
3.1.3	Comparison of Aerogels and Aerogel-Composites .....	42
3.2	Vinyl Modification of Hybrid Aerogels .....	45
3.2.1	Density and Microstructure .....	46
3.2.2	Surface Chemistry .....	48
3.2.3	Thermal Properties .....	52
3.2.4	Mechanical Properties .....	53
3.2.5	Reaction to Fire .....	54
3.2.6	Thermal Decomposition .....	57
3.2.7	Comparison of Non-functionalized and Functionalized Aerogels .....	59
3.3	Synthesis of Particles .....	60
3.3.1	Density and Microstructure .....	60
3.3.2	Particle Size Distribution .....	62
3.3.3	Thermal Properties .....	64
3.3.4	Conclusion.....	65
3.4	Silica Aerogel-Aerogel Composites .....	66
3.4.1	Density, Porosity, and Shrinkage.....	66
3.4.2	Thermal Properties .....	67
3.4.3	Mechanical Properties .....	68
3.4.4	Conclusion.....	70
<b>4</b>	<b>Experimental Part.....</b>	<b>71</b>
4.1	Materials and Methods .....	71
4.1.1	Synthesis of MTMS-DMDMS-based Monolithic Aerogels.....	71
4.1.1.1	Aerogels .....	71
4.1.1.2	Aerogel Composites .....	73
4.1.2	Vinyl Modification of Monolithic Aerogels.....	74
4.1.2.1	Synthesis of Vinyl Containing Monoliths .....	74
4.1.2.2	Functionalization via Thiol-Ene Click-Reaction.....	75
4.1.3	Synthesis of Particles .....	75
4.1.4	Silica Aerogel-Aerogel Composites .....	77
4.2	Characterization .....	78
4.2.1	Density, Porosity, and Shrinkage.....	78
4.2.2	Thermal Conductivity .....	79
4.2.3	Acoustic Properties .....	79

4.2.4	Morphology and Energy-dispersive X-ray Spectroscopy .....	80
4.2.5	Mechanical Properties .....	80
4.2.6	Hydrophobicity.....	80
4.2.7	Solid-State Nuclear Magnetic Resonance Spectroscopy .....	80
4.2.8	Reaction to Fire Test.....	80
4.2.9	Thermogravimetric Analysis .....	81
4.2.10	Simultaneous Thermal Analysis .....	81
4.2.11	Particle Size.....	81
4.2.12	Digital Microscopy.....	82
<b>5</b>	<b>Summary and Outlook.....</b>	<b>83</b>
<b>6</b>	<b>References .....</b>	<b>86</b>
<b>7</b>	<b>Appendix .....</b>	<b>97</b>
7.1	Nomenclature .....	97
7.1.1	Abbreviations .....	97
7.1.2	Symbols.....	98
7.2	List of Figures .....	99
7.3	List of Tables .....	104
7.4	Experimental Results.....	106
7.4.1	Dilution of Precursors .....	106
7.4.1.1	Pure Aerogels .....	106
7.4.1.2	Aerogel Composites .....	108
7.4.2	Vinyl Modification of Hybrid Aerogels .....	108
7.4.3	Synthesis of Particles .....	111
7.4.4	Silica Aerogel-Aerogel Composites .....	111
7.5	Eidesstattliche Erklärung.....	113
7.6	Zugänglichkeit von Daten und Materialien.....	114
7.7	<i>Curriculum Vitae</i> .....	115





## 1 Introduction

Thermal and acoustic insulation materials are fundamental for modern construction and industrial applications. Thermal insulation materials are engineered to impede the transfer of heat energy, enhancing energy efficiency and reducing heating/cooling costs in the building and transportation sector. Further, insufficient thermal insulation can cause structural damages as well as uncomfortable and unhealthy conditions. [1, 2]

In contrast to thermal insulation materials, whose main purpose is to reduce energy losses, acoustic insulation materials primarily focus on dampening sound transmission by absorbing or reflecting sound waves, play a crucial role in controlling noise levels, helping to create a quiet and comfortable environment, especially in the area of occupational safety. [3]

Several requirements exist for both types of insulations, *e.g.*, the materials used should guarantee good performance throughout their whole life cycle, be fire resistant, have low water vapor permeability, and be eco-friendly. [2]

As shown in Figure 1, the global market sales for thermal insulation materials in *i.e.*, buildings, are continuously increasing. The increasing demand is driven by the need for the reduction of greenhouse gases as well as cost efficiency and governmental regulations [4]. The European Union shows the highest market sales followed by North America and Asia Pacific.

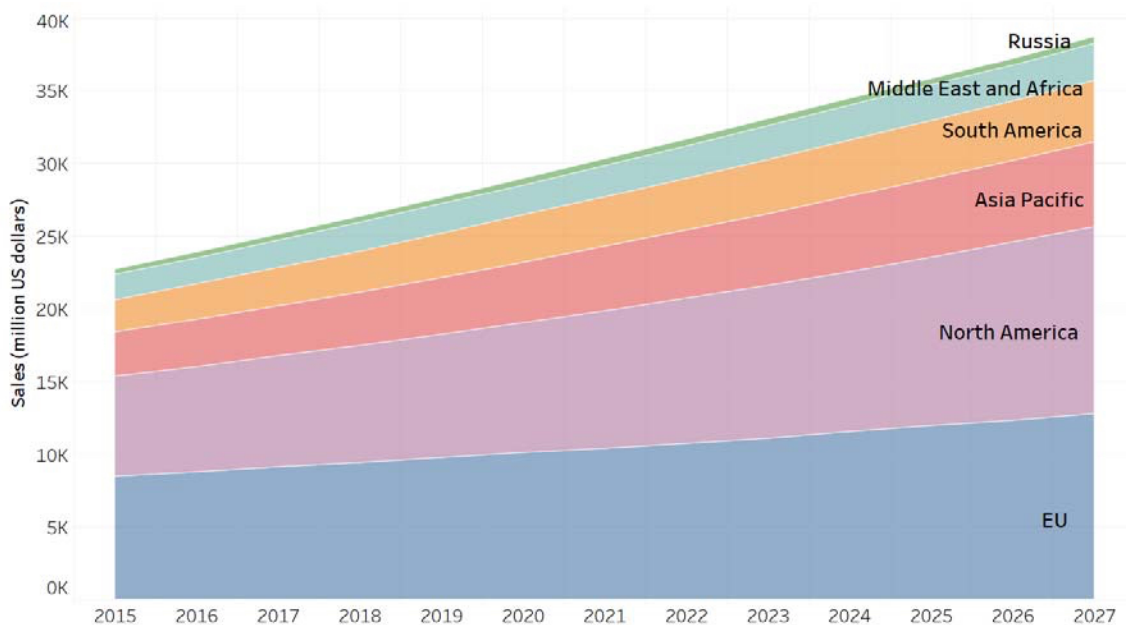


Figure 1: Global market forecast for building thermal insulation, by region [4]. Source: Joint Research Centre (JRC) representation with data from Visiongain, 2017.

In 2018 the World Health Organization (WHO) updated its “Environmental Noise Guidelines for the European Region” giving recommendations on environmental noise exposure [5], showing that noise is one of the top environmental risks for health and well-being and therefore

gaining growing concerns of public and policy [6, 7]. Among others, to reach specific noise levels, there is an increasing demand for acoustic insulation materials. This trend can be observed worldwide (cf. Figure 2) [8].

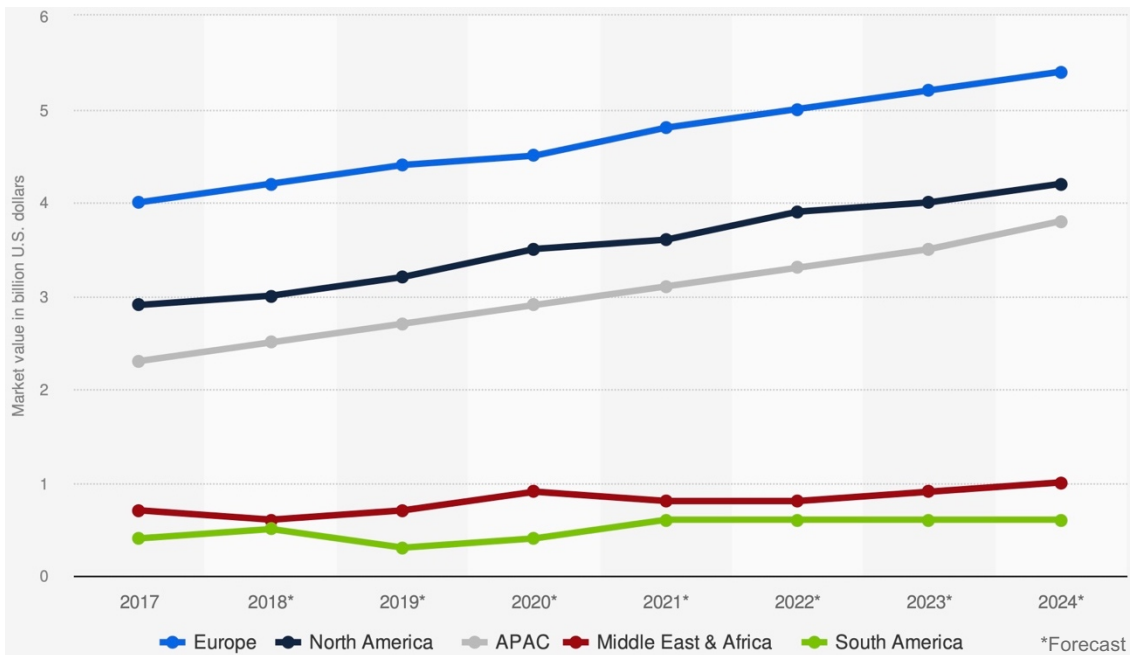


Figure 2: Market value of acoustic insulation worldwide from 2017 to 2024 (in billion U.S. dollars), by region. [8]

Especially in the transportation sector, lightweight insulation materials are crucial. Reducing the weight of vehicles, aircraft, and ships reduces fuel consumption, resulting in lower operating costs and reduced emissions. Lightweight materials help improve overall energy efficiency. By improving fuel efficiency, lightweight insulation materials help reduce greenhouse gas emissions and support global efforts to minimize the environmental footprint of the transportation industry. [9, 10] In aviation, shipping, and freight transportation, lighter materials allow increased payload capacities without exceeding weight limits, improving profitability and operational flexibility [11-13]. As electric vehicles become more prevalent, lighter insulation materials help offset the weight of batteries, improving their range and efficiency [14, 15].

In this context, silica aerogels, which possess remarkable properties including low density, low thermal conductivity, and high sound absorption, are optimal candidates for lightweight insulation materials [16-18]. Although classical pure silica aerogels are inherently brittle and challenging to handle, adapting the sol-gel process and implementing organic-inorganic alkoxysilane precursors can yield hybrid materials with enhanced mechanical flexibility and favorable hydrophobicity while maintaining their exceptional insulation performance [19, 20]. The implementation of organic-inorganic alkoxysilane precursors typically leads to an increased density compared to the classical silica aerogels. Therefore, the challenge is to decrease

the material's density while still retaining its properties. This work aims at the following main objectives:

- **Improvement of density:** Part of this work includes developing a simple and low-cost synthesis route based on the sol-gel process for ambient pressure dried aerogel light-weight insulation materials.
- **Improvement of reaction to fire:** Part of this research is to identify an effective flame-retardant agent that can overcome the disadvantage of the higher reactivity to fire of hybrid silica aerogels in comparison to pure silica ones.
- **Improvement of thermal conductivity:** Part of this work involves further reducing the thermal conductivity of the material so that less material is needed to achieve the same thermal conductivity, thereby reducing the weight of the insulation material.

This work is structured in a detailed and systematic way: The following chapter 2, “State of the Art”, reviews existing knowledge on silica aerogels and their various types, focusing on synthesis, functionalization, and their applications, with particular attention to the use as thermal and acoustic insulation materials. In chapter 3, “Results and Discussion”, experimental findings are presented concerning precursor dilution, hybrid aerogel modifications, and particle synthesis, comparing pure aerogels with aerogel composites. The “Experimental Part” (chapter 4) outlines the materials, methods, and characterization techniques used to synthesize and analyze the aerogels and their composites, followed by a “Summary and Outlook” (chapter 5) that highlights the key conclusions. Future research directions are proposed based on the experimental results.

## 2 State of the Art

### 2.1 Aerogels: From Synthesis to Application

The invention of Aerogels goes back to the 1930s when Samuel Stephens Kistler invented the first aerogel, which was made from silica. He defined aerogels as “gels in which the liquid was replaced with a gas, without collapsing the gel solid network”. [21] Since their invention, many experts have tried to find a sufficient definition for aerogels [22-25], but there has never been established such a definition in the aerogel community.

The aerogel properties stem from the microstructure of the solid network, typically composed of interconnected nanoparticles, resulting in a highly porous structure. Typical properties are high porosity (80 to 99.8%), very low bulk density (0.004 to 0.5 g cm<sup>-3</sup>), low thermal conductivity (0.017 to 0.021 W m<sup>-1</sup>K<sup>-1</sup>), high surface area (100 to 1600 m<sup>2</sup> g<sup>-1</sup>), high pore volumes and defined pore size distribution [23].

Aerogels can be made of a huge variety of materials, *i.e.*, metal and metalloid oxides, organic and biopolymers, minerals, and inorganic non-oxides. [26] In most cases, aerogels are synthesized *via* the sol-gel process but can also be prepared in other ways, for example, by the direct assembly of prefabricated nanoscale objects through freeze casting [27], chemical, and physical vapor deposition techniques [28, 29], polymer expansion in supercritical or near-critical fluids [30] and combustion synthesis [31].

The following chapters are mainly focused on silica aerogels.

#### 2.1.1 Sol-Gel Process

The sol-gel process consists of the terms sol and gel. A sol can be defined as a colloidal solution with macromolecules or particles dispersed in a liquid. Gels are porous, three-dimensional networks filled and surrounded by a liquid. They are formed by covalent bonding between the individual sol particles. The sol-gel synthesis can be either water- or alcohol-based, and resulting gels are therefore called hydrogels or alcogels.

With some exceptions, the sol-gel process can be divided into different stages [32]:

- formation of a sol from precursors through hydrolysis and condensation reactions,
- sol to gel transition,
- gel formation.

The last step for aerogel formation is the drying process to remove the liquid phase from the pores to get the solid dried material [33].

The choice of precursor is decisive for reaction kinetics and final material. The most common precursors are metal alkoxides, especially silicon alkoxides (cf. Figure 3). The properties of alkoxysilanes change according to their dimension, as larger side groups are responsible for steric hindrance. Tetramethyl orthosilicate (TMOS), therefore, has an almost six times faster hydrolysis reaction than tetraethyl orthosilicate (TEOS). [26]

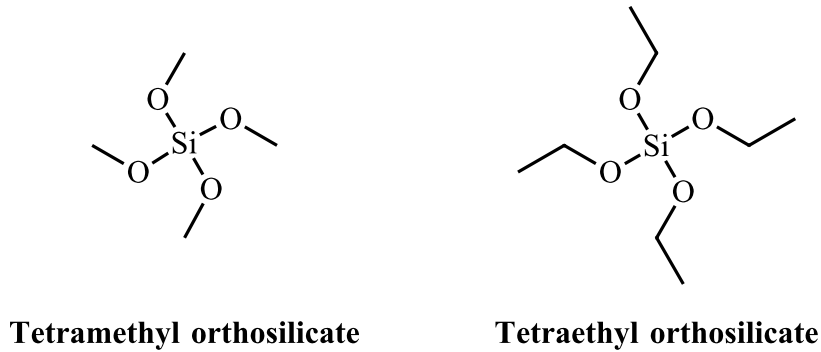
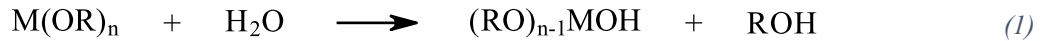


Figure 3: Common silicon alkoxide precursors tetramethyl orthosilicate (TMOS) and tetraethyl orthosilicate (TEOS).

The hydrolysis of silicon alkoxides in water-ethanol mixtures with sufficient catalyst leads to metal hydroxides (MOH) and the release of alcohol molecules. The hydroxy group (OH) substitutes the alkoxide group (OR) according to (1).



As soon as hydrolysis starts, the first hydrolyzed species are condensed. The pH value of the solution has a strong effect on the reaction speeds of the hydrolysis and the condensation reaction and, therefore, also influences the final structure of the gel.

The condensation of -OH releases water or alcohol and forms M-O-M units: two -M-OH groups give water (2) while -M-OH with -M-OR releases alcohol molecules (3). Further, polycondensation forms the solid backbone of the gel.



In the wet gels, further rearrangements and reactions take place. This step is called aging and is due to three main processes [34]:

- The liquid phase inside the pores still consists of unreacted precursor molecules and, therefore, can further react with the solid backbone.
- The backbone itself is still flexible and allows neighboring M-OH and M-OR groups to react further, causing contraction and shrinkage of the gel.

- Ostwald ripening: Mass is dissolved in regions with high positive curvature and small particles to particle necks, pores, and crevices because these regions are thermodynamically more favorable.

Aging is often a crucial step before drying the wet gels, which significantly increases the stiffness of the gels.

### 2.1.2 Drying of Wet Gels

During drying, the solvent present in the gel structure is removed through evaporation or other drying methods, leading to the network's consolidation and forming a porous structure. The drying process significantly influences the final characteristics of the gel-derived material, including its porosity, density, surface area, and mechanical strength. Three main drying techniques, ambient pressure drying (APD), freeze-drying, and supercritical drying (SCD), offer different advantages and are chosen based on the specific requirements of the final material. All techniques aim to prevent the gel from shrinkage and cracking during drying, caused by capillary pressure from solvent evaporation and often resulting in the collapse of the gel structure. SCD uses the fact that supercritical fluids show zero surface tension, preventing the gel network from cracking and collapsing. The most prominent fluid for SCD is carbon dioxide due to the relatively mild conditions needed to reach the supercritical state. Before SCD, often a solvent exchange process needs to be done. Since the liquid phase inside the pores needs to be soluble in CO<sub>2</sub>, a change to ethanol or acetone is often performed. Both solvents show good solubility in CO<sub>2</sub> [26] and are easy and safe to handle.

A typical SCD process looks the following [35]: (1) loading of wet samples, (2) feed of carbon dioxide in the autoclave to reach a pressure of 11 – 12 MPa, continuous or batch-wise feed of fresh carbon dioxide until all organic solvent is extracted, (3) release of pressure to transform supercritical CO<sub>2</sub> into the gas phase.

In freeze drying, sublimation of solvent is used to prevent the capillary forces inside the pores. Sublimation means the phase change from solid to gas phase without becoming a liquid. A typical freeze-drying process, therefore, looks the following [26]: (1) wet samples, (2) freezing to solid state, (3) applying vacuum to reduce the pressure below the triple-point pressure of the pore fluid, (4) continuous sublimation of solvent due to thermal energy.

The process of freeze drying can be cheaper than SCD but does not have to. Since freeze drying does not require high pressures, it is easy to handle. Especially in lab- and pilot-scale, there is a lower capital expense expected. The drawbacks of the technique are not as good material

properties of aerogels as for SCD ones and problems with the synthesis of monoliths of brittle materials. [26]

For APD, there exist some limitations: The gel network must be sufficiently strong so that it does not collapse despite the capillary forces. The pores should be as large as possible, and the pore size distribution as monomodal as possible to minimize the difference in capillary forces. [33] Capillary forces can be reduced due to the choice of evaporation solvent since the capillary pressure  $p_c$  is dependent on the liquid gas interfacial tension  $\sigma_{lg}$ , following the Young-Laplace equation shown in equation (4). Typical solvents for evaporation are water, ethanol, methanol, and 2-propanol since especially later ones show low liquid gas interfacial tension [36]. Gels with bigger pores are more favored for ambient pressure drying since the resulting capillary pressure is lower with bigger pore radius  $R$ .

$$p_c = \frac{2\sigma_{lg} \cos \theta_p}{R} \quad (4)$$

Further, the flexibility of the network and addition of non-polar groups on pore walls due to the choice of precursor or later functionalization can result in a “spring-back effect” during drying. This effect is caused by repulsion due to the surface groups so that the wet gels are allowed to initially shrink and later go back to their original dimensions (cf. Figure 4).

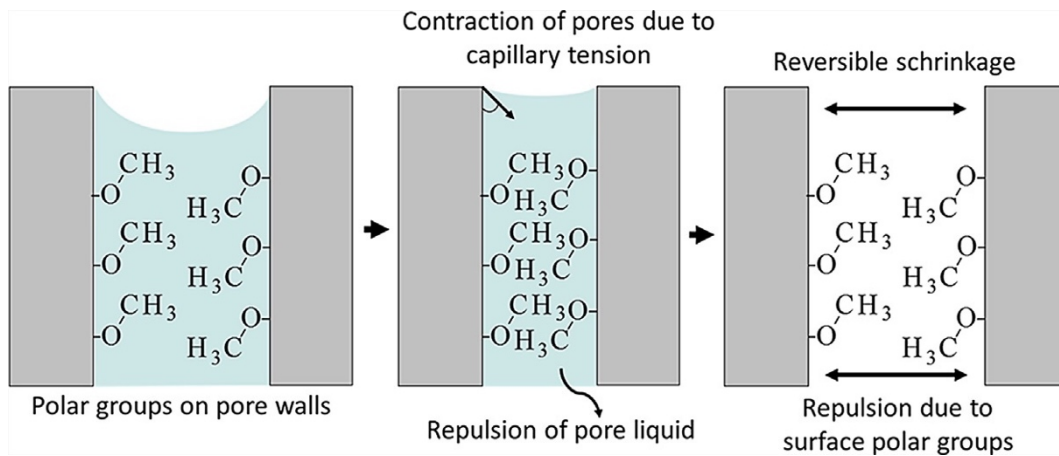


Figure 4: Polar groups on the pore surface result in reversible shrinkage (“spring-back”) of the sample during/after drying. Reprinted from [37], with the permission from Elsevier.

### 2.1.3 Aerogel Applications

Aerogels, with their remarkable properties, can be used in many different application fields. Because of their super-insulating properties, they can be used to reduce energy losses in many fields like cryogenic applications and building insulation. Further applications as insulation material are seen in window panes, solar collector covers, or high-temperature applications since some are temperature stable up to 1200°C and above. [37]

Additionally, their high surface area and porous structure make them ideal candidates for applications in catalysis, where they facilitate efficient chemical reactions by providing large active surface areas for catalyst deposition. They can be used for carbon capturing, as presented by Lin *et al.* [38] and Linneen *et al.* [39], or for the generation of hydrogen gas, as demonstrated by Domínguez *et al.* [40, 41]. Aerogels are also employed in environmental remediation efforts, acting as absorbents for oil spills and pollutants due to their high porosity and affinity for certain substances: Venkateshwara Rao *et al.* investigated the absorption and desorption capacities of super hydrophobic silica aerogels using different solvents and oils. [42, 43]

Due to their high surface area and good pore accessibility, they are ideal candidates for sensor applications: Wang *et al.* studied the performance of silica aerogels as potential humidity sensors [44], and Li *et al.* focused on biosensors for nucleotide acids [45].

As SiO<sub>2</sub> aerogels typically show low dielectric constants, their use as thin film interlayer dielectrics (for potential use in semiconductors) was investigated by the group of Park *et al.* [46, 47].

Furthermore, aerogels in general have been studied as materials in life science and biomedical applications, *i.e.*, as bone scaffolds [48], absorbable implants for drug release [49], or as biological sensors [50].

### 2.2 Hybrid-Silica Aerogels

By incorporating organic groups into the silica network, these types of aerogels can gain flexibility and resilience while retaining the low density, high porosity, and excellent thermal insulating properties characteristic of traditional silica aerogels. Furthermore, they can gain hydrophobic or hydrophilic properties depending on the organic groups introduced.

There exist several different methods for synthesizing organic-inorganic hybrid aerogels [20]:

- Combination of silica and organic polymers, *i.e.*, TMOS/TEOS and poly(2-vinyl pyridine) or silanol-terminated polydimethylsiloxane,
- organoalkoxysilanes, *i.e.*, methyltrimethoxysilane (MTMS), dimethyldimethoxysilane (DMDMS), 3-methacryloxypropyltrimethoxysilane,
- organobridged alkoxysilanes, *i.e.*, 1,6-bis(trimethoxysilyl)hexane, 1,2-bis(methyldiethoxysilyl)ethane.

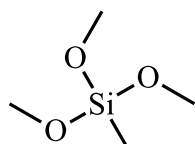
The replacement of alkoxy groups by other organic groups (such as alkyl groups) can lead to flexible and hydrophobic samples: The presence of non-polar alkyl groups attached to the silica polymer chains results in the minimization of inter-chain cohesion and reduced crosslinking density, thereby creating an elastic and flexible three-dimensional network.



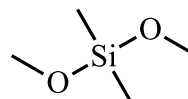
In the next paragraphs, aerogels made of organotrialkoxysilanes are explained in detail since these are most relevant for the study done in this thesis.

### 2.2.1 Synthesis

Flexible hybrid-silica aerogels can be synthesized from organotrialkoxysilanes such as MTMS and DMDMS (cf. Figure 5). Compared to TEOS or TMOS, alkyl groups replaced one or two alkoxy groups.



**Methyltrimethoxysilane**



**Dimethyldimethoxysilane**

Figure 5: Chemical structure of precursors methyltrimethoxysilane (MTMS) and dimethyldimethoxysilane (DMDMS).

For the synthesis of alkoxy silane-based aerogels, the pH is generally recognized as one of the most important factors influencing the final materials' porosity, density, strength, transparency, and chemical microstructure [51]. Other factors are water-to-precursor ratio, type and concentration of additives (surfactants and catalysts) which can influence the porous monolithic material from microporous transparent aerogels to opaque microporous ones [52].

Surfactants can be necessary to prevent the hydrophobic precursors and the forming network from phase-separation with the solvent: The use of surfactants, which typically consist of a coordinating head group and a long alkyl chain, provides an organic shell around the particles, thereby preventing their agglomeration during synthesis. This results in the colloidal stability of the nanoparticles in the solvent during network formation. Typical used surfactants are either nonionic or cationic ones. In the case of nonionic surfactants, poly(ethylene oxide)-block-poly(propylene oxide)-block-poly(ethylene oxide) (Pluronic<sup>®</sup> F127) and polyoxyethylene 2-ethylhexylether (Nonion EH-208) are typically used, for ionic surfactants, cetyltrimethylammonium salt (bromide CTAB or chloride CTAC) are widely used [53-58].

First aerogels based on MTMS as co-precursor were synthesized by Venkateswara Rao *et al.* in 1999 [59]. They further investigated pure MTMS aerogels with a two-step acid-base catalyzed process obtaining opaque aerogels within a density range from 0.04 to 0.1 g cm<sup>-1</sup> using methanol as solvent [42]. Kanamori *et al.* developed a process using water as the solvent and introducing the surfactant CTAC to prevent precursors from phase separation [60]. They further worked on co-precursor gelation of MTMS/DMDMS systems, resulting in opaque, strongly compressive, and bending flexible samples [61]. These aerogels are typically termed as

“marshmallow gels” and can easily be dried at ambient conditions due to their macroporous structure and superhydrophobicity.

### 2.2.2 Functionalization

As standard marshmallow-like aerogels already show high flexibility and bendability as well as hydrophobicity, there were several studies performed to further enhance these properties for desired applications. The idea is to introduce active functional groups at the surface of the aerogel after the sol-gel process for further functionalization. In the literature, there are few reports related to this topic [62-65].

Ehgartner *et al.* reported on the investigation of the co-condensation approach of MTMS and organofunctional alkoxy silanes with reactive functional groups, *e.g.* vinyl-, chloropropyl-, mercaptopropyl-, and methacryloxypropyltrimethoxysilane. All functional gels presented in this research showed excellent elastic compression behavior of up to 60% and had accessible functional groups for either redox, nucleophilic substitution, or click reactions. [65]

These types of reactions allow the application-related functionalization of the monolithic aerogels with further components, *e.g.* flame retardants, catalysts, absorbing agents, and further.

For chemical postprocessing of monolithic aerogel samples, active groups inside the monoliths need to be available. Standard marshmallow-like gels synthesized with the MTMS/DMDMS co-precursor method do not have any reactive groups inside their network. Therefore, these precursors need to be (at least partially) exchanged to have the opportunity for later functionalization steps. Vinyltrimethoxysilane (VTMS) and vinylmethyldimethoxysilane (VMDMS) are ideal candidates since their structure does not vary a lot from MTMS and DMDMS respectively (cf. Figure 6). It can be expected that their reaction kinetics and gelation behavior therefore are quite similar. For more bulky groups an incorporation of dangling bonds into the final network would lead to a lower crosslinking density and higher deformability [65]. Furthermore, steric and charge effects could occur and therefore change the kinetics a lot [66].



**Vinyltrimethoxysilane**

**Vinylmethyldimethoxysilane**

Figure 6: Chemical structure of precursors vinyltrimethoxysilane (VTMS) and vinylmethyldimethoxysilane (VMDMS).

Flame retardants are one possibility for later functionalization of vinyl-containing aerogel monoliths. In general, they can be divided into four main classes [67]:

- Inorganic compounds like aluminum hydroxide and magnesium hydroxide,
- halogenated compounds like organochlorines and organobromines,
- organophosphorus compounds like triphenyl phosphate and vinylphosphonic acid (VPA),
- organic compounds like carboxylic acid and dicarboxylic acid.

The class of organophosphorus compounds gains more and more interest since they are compared to the inorganic compounds typically light. Halogenated compounds are highly effective during pyrolysis but react to toxic vapors and gases. Organic compounds are often less durable than organophosphorus compounds, especially when the latter are intermolecularly bonded to the material. Organophosphate flame retardants act through several mechanisms to reduce the flammability of materials [68]:

- Char formation: when exposed to heat or flame, organophosphate flame retardants can decompose and form a protective layer of char on the surface of the material. This char acts as a barrier, insulating the underlying material from the heat and limiting the availability of combustible gases.
- Phosphorus radical scavenging: organophosphate flame retardants can release phosphorus-containing radicals during combustion. These radicals can interfere with the combustion process by scavenging other reactive radicals that are necessary for sustaining the flame. This interrupts the chain reaction of combustion and reduces the intensity of the fire.
- Dilution of combustible gases: some organophosphate flame retardants release non-flammable gases, such as carbon dioxide and water vapor, when exposed to heat or flame. These gases dilute the concentration of combustible gases in the vicinity of the flame, making it more difficult for the fire to propagate.
- Endothermic decomposition: during combustion, organophosphate flame retardants undergo endothermic decomposition, absorbing heat from the surrounding environment.

This reduces the temperature of the material and slows down the rate of combustion.

One example of an organophosphate that can be intermolecularly bonded to vinyl-containing aerogels is vinylphosphonic acid. Liu *et al.* invented a process for functionalizing VTMS containing monolithic columns with VPA. Therefore, they used thiol-ene click reactions twice: first, a radical addition of a dithiol compound was performed, and second, VPA was radically bonded to before added thiol-groups (cf. Figure 7). [69]

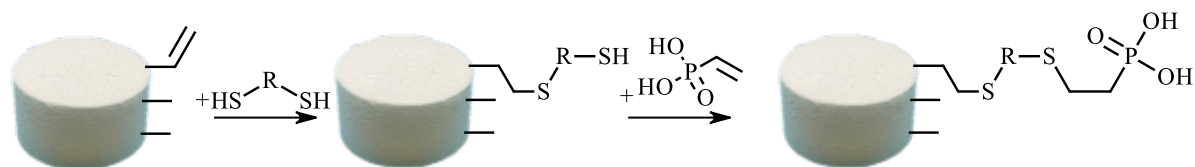


Figure 7: Illustration of two-step thiol-ene click reactions for radical addition of VPA to VTMS containing monolithic aerogel.

### 2.2.3 Materials and Structures

In general, flexible hybrid-silica aerogels can be synthesized in different sizes, shapes and variations, resulting in monoliths, composites or particles. In the following sections, strategies and important factors for synthesizing the before-listed variations of marshmallow-like gels and aerogels are explained in detail.

#### 2.2.3.1 Monoliths

In general, for the production of monolithic aerogel samples in several geometries there are important practical aspects for molding, aging, and demolding, which should be taken into account. Other aspects that should be considered may be the need for solvent exchange: larger samples with low surface area to solvent take much longer to reach equilibrium during the exchange process due to longer diffusion paths inside the monolithic sample.

For molding, a suitable container is needed in which the gelation and often aging process can occur. The reactive mixture (sol) is then poured into the container. The materials used for the mold should be tested for chemical compatibility. Since gelation is often done at higher temperatures, this should be taken into account too. Common materials are polymers like polyethylene, polypropylene or polytetrafluoroethylene, stainless steel, glass, and rubber materials. While glass can be suitable for many aerogel recipes, inorganic oxide aerogels are often very sticky to it. Generally, smooth surfaces are desirable for demolding. For fragile gel formulations sharp corners and high-aspect-ratio inclusions should be avoided. [26]

Suitable containers should also provide tightness to keep vapors generated by the sol-gel formulations to prevent exposed surfaces of the resulting gels from drying out and cracking during aging later [26]. Some recipes need a saturated atmosphere with solvent for proper gelation. On a lab scale, plastic syringes, plastic beakers, and glassware are often used.

For the synthesis of bigger monolithic samples, some recipes need to be optimized since local pH differences or temperature variations can lead to a change in the solid network structure. Others require longer aging or surface modifications [70].

### 2.2.3.2 Fiber-Matrix Composites

Fiber-matrix composites typically consist of reinforcing fibers and a bedding matrix which acts as the filler and adhesive between the fibers. Due to interactions between the two components, the overall material obtains higher quality properties than each of the two components alone. A well-known example is concrete, which is often reinforced with steel. Other fiber materials are made of glass, carbon, ceramics, aramid, nylon, boron, basalt, and steel. Fibers can also be obtained from nature, such as wood or linen fibers. The matrix often consists of polymers, concrete, metals, ceramics, or carbon. Composites often show a high degree of anisotropy and therefore their properties vary significantly within the material [71].

Since composite materials consist of at least two different materials, there has to be an interface region between the matrix and reinforcement. Mainly four different mechanism types exist that contribute to adhesion between those: Adhesion based on van der Waals forces, diffusional processes where atoms or molecules from the matrix material may diffuse into the reinforcement material and vice versa, chemical bonds between the molecules of the matrix, and reinforcement and mechanical interlocking, where the surface irregularities of one material mechanically engage with those of the other material. [71]

According to classical silica aerogels, Parmenter and Milstein first investigated glass fibers for reinforcement of silica aerogels and the mechanical as well as thermal properties of resulting composites [72]. Several other studies have reported on such reinforcement procedures [73-75]. Rege *et al.* studied the influence of fiber reinforcement on the mechanical and thermal properties of MTMS/DMDMS-based marshmallow-like aerogels in 2019 [76]. A common characteristic of the aforementioned composites is that the aerogel is employed as a matrix, rather than as a filler.

### 2.2.3.3 Aerogel-Aerogel Composites

In contrast to composites with aerogel materials as the matrix, aerogels can also be used as filler in several applications: Welsch *et. al* [77, 78] and Gao *et. al* [79] used silica aerogel particles with their low thermal conductivity as filler for high-performance concrete. Silica nanoparticles can also act as filler for typical polymer matrices, *e.g.* epoxy, polyurethane, nylon, polyester, polypropylene, or others [80]. Aminoroaya *et. al* focused on silica aerogel fillers to improve the fracture mechanics of methacrylate-based dental composites [81].

Only a few aerogel-aerogel composites are known in the literature in which an aerogel is used both as a matrix and as a filler. Milow and Ratke grant a patent for the synthesis of resorcinol-formaldehyde aerogels with hydrophobic silica aerogel particles as filler [82]. Laskowski *et. al*

further investigated the silica aerogel particles embedded within a matrix of resorcinol-formaldehyde or cellulose aerogels [83-85]. Niemeyer and Milow applied for a patent to produce silica- or carbon aerogels inside a polysaccharide aerogel as thin films or beads [86]. The previously mentioned composites are all designed to achieve the following primary targets: enhanced thermal/acoustic properties, increased mechanical stability, and/or reduced density.

To my knowledge, there are no publications to date that deal with silica aerogel-aerogel monolithic composites in which silica aerogels are used both as a matrix and as a filler.

### 2.2.3.4 Aerogel Particles

Compared to monolithic aerogel samples, particles are beneficial in terms of faster and more cost-efficient solvent exchange and drying processes because of their high surface area compared to their low volume. Further, they show lower bulk densities as monolithic samples by nature because of their packing density and inclusion of air inside a bulk.

Aerogel particles could be synthesized by breaking down wet gels using a high-power mixer or *via* ball dropping method by using hydrolyzed sol. Another method is called emulsification or emulsion method, which will be further explained in detail.

An emulsion is a mixture of two or more immiscible liquids, typically consisting of droplets of one liquid dispersed throughout another liquid. These liquids usually include a continuous phase (the medium in which the droplets are suspended) and a dispersed phase (the droplets themselves). Emulsions are stabilized by emulsifiers, which prevent the droplets from coalescing and separating. For the synthesis of silica aerogel particles, the aqueous sol acts as the water phase and is dispersed in hexane or other organic solvents as the oil phase to form a stable water-in-oil emulsion (W/O-emulsion). The emulsion process in general is well-known for polymer synthesis and enables large-scale production of microspheres with controllable particle sizes and distributions [87]. Parameters influencing the size and shape of particles typically are the choice and amount of surfactant as well as the rotation speed and the volumes of water/oil phase.

Several studies have been published in the literature in which organoalkoxysilanes were used as precursors [88-91]. For example, Yun *et al.* obtained silica aerogel particles based on MTMS as a precursor with a bulk density as low as  $0.08 \text{ g cm}^{-1}$  [89]. To my knowledge, there exist no publications using the co-precursor method with MTMS and DMDMS in an emulsion process for obtaining marshmallow-like hydrophobic aerogel particles so far.

### 2.2.4 Properties

Despite the reduction in transparency caused by the macroscopic phase separation resulting from increased hydrophobicity with rising DMDMS levels, "marshmallow-like" gels with low density (approximately  $0.10 \text{ g cm}^{-3}$ ) and excellent bending flexibility are achieved. The characteristic pore structure falls within the micrometer scale, and the macro-pore skeletons are non-porous. [20]

The material typically exhibits thermal conductivities of approx.  $30 \text{ mW m}^{-1}\text{K}^{-1}$ , showcasing their remarkable insulating capabilities. The unique microstructure of marshmallow-like aerogels contributes significantly to their low thermal conductivity values (cf. section 2.3.1 "Thermal Insulation"). [76, 92]

The marshmallow-like gels exhibit exceptional flexibility under diverse deformations, and this flexibility remains intact even at extremely low temperatures, such as the boiling point of liquid nitrogen ( $-196^\circ\text{C}$ ) [93]. The mechanical flexibility is advantageous for good sound absorption properties (cf. section 2.3.2 "Acoustic Insulation"). The material generally shows much higher values in the range of 200 – 1600 Hz than polyurethane-based materials [20].

Another interesting feature of marshmallow-like gels is their hydrophobicity up to superhydrophobic water contact angles of  $> 150^\circ$ . This is caused by the low free surface energy of the silicon backbone and the surface roughness of the macroporous structure. [93] The hydrophobicity exhibits selective absorption of oil (*e.g.*, n-hexane and mineral oil) from an oil-water two-phase system. This property renders it suitable for the extraction and collection of oil contaminants and pollutants, facilitating both cleanup efforts and analytical procedures. With simple compression (*e.g.*, by hand), the absorbed oil can be expelled, allowing the marshmallow-like gel to be reused for subsequent cycles. [93, 94] Methods and techniques for quantifying hydrophobicity are presented in section 2.2.4.4 "Hydrophobicity".

Flexible hybrid silica aerogels show a major disadvantage in terms of their reaction to fire. With an increasing number of organic side groups inside the solid backbone, the reactivity of the final material at higher temperatures increases. In interaction with oxygen, the material can start burning through a two-step combustion mechanism: First, the organic groups ( $\text{Si-CH}_3$ ) are decomposed and generate combustibles in the gas phase, then these combustibles in certain concentrations start reacting with oxygen [95]. In contrast to other solid combustible materials, the hybrid silica aerogel's surface experiences considerably prolonged flame development, demonstrating a distinct flame propagation phenomenon [96]. In literature, several techniques are known to analyze the material's reaction to fire, which are shown in detail in section 2.2.4.5 "Reaction to Fire".

### 2.2.4.1 Mechanical Behavior

The first flexible hybrid silica aerogels based on MTMS, invented by Venkateswara Rao *et al.*, showed high flexibility against compression as well as bending. In comparison to traditional silica aerogels, these flexible types with densities in the range from  $0.04 - 0.10 \text{ g cm}^{-3}$  showed about a factor of 10 lower Young's moduli for similar bulk densities and were measured in the range of  $30 - 141 \text{ kPa}$ . The samples showed remarkable spring-back effects after compression and bending: up to a load of 60% strain, the sample recovered after the load was removed to its original shape. [42] The notable flexibility exhibited under compression and bending conditions suggests that the material can be easily handled and that applications based on strain recovery are feasible (cf. Figure 8).

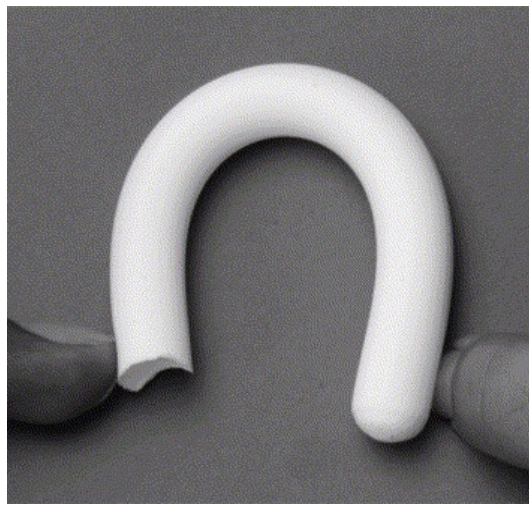


Figure 8: MTMS-based aerogel with notable flexibility allows easy handling. Reprinted from [42], with permission from Elsevier.

Further improvement could be observed using a co-precursor method with MTMS and DMDMS mixtures. The marshmallow gels invented by Hayase *et al.* typically had Young's moduli below  $10 \text{ kPa}$ . Furthermore, the compressive strength rarely exceeded  $0.10 \text{ MPa}$  at 80% strain. MTMS/DMDMS-based aerogels demonstrated improved flexibility when subjected to bending loads, withstanding bending at high curvatures without fracturing. The mechanical flexibility was given even at liquid nitrogen temperature ( $-196^\circ\text{C}$ ). [61, 63, 97]

### 2.2.4.2 Thermal Conductivity

Traditional, non-flexible silica aerogels synthesized by Kistler in 1932 showed thermal conductivities of approx.  $20 \text{ mW m}^{-1} \text{ K}^{-1}$  in air and in the order of  $10 \text{ mW m}^{-1} \text{ K}^{-1}$  when evacuated. [98] Flexible hybrid-silica aerogels typically exhibit slightly higher conductivities in the range of  $30 - 40 \text{ mW m}^{-1} \text{ K}^{-1}$ , depending on their chemical composition and resulting morphology.



As previously stated in section 2.2.1, the pH during gelation represents a significant influencing factor concerning the microstructure of aerogels. Consequently, it exerts a considerable impact on the thermal conductivity of these materials.

Al-sharuee investigated the relationship between pH and thermal conductivity for classical TEOS-based aerogels. He found out that for condensation reactions under basic conditions, the resulting thermal conductivity was much lower than for acidic condensed silica aerogels. [99] The thermal conductivity can also be influenced due to the aging process: Nadargi *et al.* found out that for MTMS-based aerogels the optimal aging time with the lowest thermal conductivity was observed after two days. Longer aging resulted in over-condensation, which consequently led to an increase in thermal conductivity. [100] Ambient pressure dried samples can lead to lower thermal conductivities when their surface is well modified, resulting in most likely hydrophobic silica aerogels. Kwon *et al.* prepared a low-thermal conductivity TEOS aerogel ( $13.6 \text{ mW m}^{-1} \text{ K}^{-1}$ ) after surface modification with trimethylchlorosilane before ambient pressure drying. [101]

#### 2.2.4.3 Acoustic Performance

The acoustic performance of aerogels is typically measured with the impedance tube method because of the small sample size requirements [102-110].

Schmidt *et al.* used hot-press-formed plates of dry-mixed silica aerogel with polyvinylbutyral (PVB), as well as silica aerogel bound with liquid vinylacetate/ethene. The observed absorption coefficients at frequencies above 600 Hz were around 0.6 – 0.7 for a 40 mm thick layer. 20 mm thick layers showed especially at lower frequencies better performance than mineral wool. [102] Dong *et al.* synthesized aerogel composites with variable concentrations of silica and polydimethylsiloxane and measured their acoustic absorption coefficient as a function of composition and average pore size. At certain frequencies, the aerogel composites showed better performance than the commercial fiberglass blankets. [103] Cai *et al.* compared monolithic aerogels based on MTMS/VTMS and two commercially available acoustic insulation materials: an open-cell polyurethane (PUR) foam with a non-woven scrim and a non-woven fiber material. The aerogel material exhibited maxima in the absorption coefficient within the frequency ranges of 540 – 830 Hz and 1570 – 1860 Hz. In contrast, the commercially available materials demonstrated enhanced acoustic absorption with increasing frequency. The strong absorption peaks in both low and high-frequency regions for the aerogel may suggest the presence of multiple resonances within the material. [104] Yan *et al.* synthesized polyimide-silica aerogel composites and studied the thickness-dependency of absorption maxima: For a thickness of 10 mm,

the peaks occurred between 5 – 8 kHz, whereas for a thickness of 30 mm, the peaks were observed at 2.5, 7 and 10 kHz. [105] Moretti and Buratti *et al.* analyzed the influence of the granule size of silica aerogels on acoustic performance. They found that the sound transmission loss was increased when the grain size was reduced, and the density and thickness of the samples were increased concurrently. [109, 110]

### 2.2.4.4 Hydrophobicity

In the literature, there exists a huge variety of methods for the quantification of hydrophobicity/hydrophilicity of aerogels, since many of their unique properties, *i.e.*, density, thermal conductivity, ..., are influenced by the adsorption of water.

Water uptake measurements are an easy way to estimate the hydrophobicity of aerogels. A sample is placed either in a controlled humidity chamber at high humidity (typically > 96% humidity) or directly placed on top of water. After some time, the mass increase is measured. Water uptake studies can typically take one to six months. Hüsing *et al.* observed for hydrophilic aerogel samples a mass increase of 10 – 60% within the first 5 days [111] while Venkateswara Rao *et al.* observed a 2% mass increase for hydrophobic samples after floating on water for three to six months [112]. Ingale *et al.* used Karl Fischer titration for the quantification of water uptake after the dissolution of humidified samples in anhydrous methanol [113].

Contact angle measurements are another option for measuring the hydrophobicity of aerogels. Therefore, a water drop is placed on top of the sample surface and analyzed with a goniometer consisting of a high-resolution camera and image processing software. Hydrophilic surfaces tend to have a contact angle of < 90°, while hydrophobic ones show contact angles of > 90°. Superhydrophobic surfaces are surfaces without any significant surface wetting and angles > 150°. [26]

Spectroscopic methods like Fourier-transform infrared (FT-IR) or solid-state nuclear magnetic resonance (NMR) spectroscopy can be used for structural analysis of samples and their available surface groups. They are often used as complementary methods to water uptake methods. Others used the calculation of surface energy [114] or special techniques for contact angles on granules and pieces of aerogels [115].

### 2.2.4.5 Reaction to Fire

The reaction to fire of materials is a critical aspect in general assessing their safety and suitability for various applications. When materials are subjected to fire, their behavior can vary significantly depending on their composition and structure. During combustion, materials undergo physical and chemical transformations, releasing heat, smoke, gases, and potentially toxic

substances. Understanding the reaction to fire involves studying parameters such as ignition temperature, flame spread, heat release rate, smoke production, and toxicity of combustion products [116].

Measurement techniques for reaction to fire play a pivotal role in accurately assessing the fire performance of materials. Various experimental methods are employed to characterize different aspects of a material's response to fire, *i.e.*, cone calorimetry, flame spread tests, smoke density measurements, and toxicity assessments. Cone calorimetry measures the heat release rate and other key parameters during controlled combustion, providing valuable data on a material's flammability and fire behavior. Flame spread tests evaluate the propensity of materials to propagate flames across surfaces, aiding in understanding their potential for fire spread. Smoke density measurements quantify the amount of smoke produced during combustion, crucial for assessing visibility and escape routes in fire scenarios. Additionally, toxicity assessments examine the chemical composition of combustion products to measure their potential health hazards. [116, 117]

In Europe, a widely used classification system categorizes materials based on their reaction to fire. Classes range from A1 (non-combustible) to F (materials not tested or classified) [118]. In the United States a “Standard Test Method for Surface Burning Characteristics of Building Materials” is used to measure the flame spread and smoke development of materials on a horizontal surface [119]. In research and development, a widely used system is a standard to specify a method for determining the heat release rate, smoke production rate, and other fire-related parameters of materials using a cone calorimeter [120].

Li *et al.* studied the combustion behaviors and oxidation kinetics of hydrophobic silica aerogels by cone calorimeter and thermal analysis. They proposed a two-step combustion mechanism: Initially, the organic groups (Si-CH<sub>3</sub>) undergo decomposition, releasing combustible substances when exposed to thermal radiation. Subsequently, the gasified combustibles accumulate to a specific concentration and undergo ignition-triggered reactions with oxygen gases. [96]

### **2.3 Thermal- and Acoustic Insulation Materials**

Thermal and acoustic insulation materials are of critical importance in controlling heat transfer and sound transmission in a variety of environments, including buildings, industrial facilities, transportation, and appliances. These materials are designed based on principles of heat transfer, wave propagation, and material science, ensuring energy efficiency, comfort, and noise reduction.

### 2.3.1 Thermal Insulation

To understand how materials can act as thermal insulators, it is necessary to understand the transfer of heat through material. In general, heat flows from hot environments to cold ones until the temperature difference is equalized and therefore follows the second law of thermodynamics. The heat can be transported by three mechanisms, which all occur at the same time and are therefore not easy to separate. According to equation (5), the total heat flow ( $\dot{Q}_{total}$ ) can be described as the sum of the heat flows due to conduction ( $\dot{Q}_{conduction}$ ), convection ( $\dot{Q}_{convection}$ ) and radiation ( $\dot{Q}_{radiation}$ ). [121]

$$\dot{Q}_{total} = \dot{Q}_{conduction} + \dot{Q}_{convection} + \dot{Q}_{radiation} \quad (5)$$

Conduction means the transport of heat by exciting neighboring particles. These particles stay in the same place; therefore, this kind of transport exists in solids, liquids at rest and gases at rest.

Heat flow due to convection is given by heat carriers which heat up at one place and move to another. These are often fluids such as gases and liquids. It can be divided further into free and forced convection. Free convection can be seen if a fluid heats up at one place and moves to the colder place due to density differences caused by the temperature difference. Forced convection is a result of the introduction of mechanical power as in a pump or ventilator. [1, 121]

Thermal radiation is the transport of heat by energy in the form of electromagnetic radiation, which is basically emitted by any object (solid, liquid, gas).

Many thermal insulation materials can be classified *via* various criteria which in the literature strongly depend on the authors [1, 4, 122-125]. Two types of classifications are shown below:

**By composition:**

- Organic, derived from natural sources or synthesized organically (cellulose, wool, synthetic foams);
- Inorganic, made from non-carbon-based substances (fiberglass, mineral wool);
- Composite, combination of organic and inorganic materials (foam glass and vacuum insulation panels).

**By structure:**

- Fibrous, consists of fibers that trap air pockets, reducing heat transfer (fiberglass and mineral wool);
- Cellular, composed of cells or voids that trap air or other gases (synthetic foams such as expanded polystyrene (EPS) or polyurethane foam);
- Granular, small particles or granules used to fill cavities (perlite and vermiculite).

Thermal insulation materials often show a complex internal structure which is crucial for the type of heat transfer through the material and typically occurs in all three states of aggregation: solid (fibers and matrix), liquid (condensed water from moisture) and gaseous (air or others). [123] The choice of material for certain kinds of applications strongly depends on the needed properties and the field of application, as well as economical and technical factors.

Aerogels, a class of porous nanomaterials and often considered in a category of advanced or high-performance insulation materials, represent a significant advancement in thermal insulation technology due to their unique structural properties. Comprising a network of nanoparticles with exceptionally high porosity (typically 90-99% air), aerogels exhibit ultra-low densities and thermal conductivities. The thermal conductivity within these materials is composed of three contributions, heat conduction through the solid backbone structure, heat transport through the pore space (typically filled with gas) and radiative heat transport (cf. Figure 9).

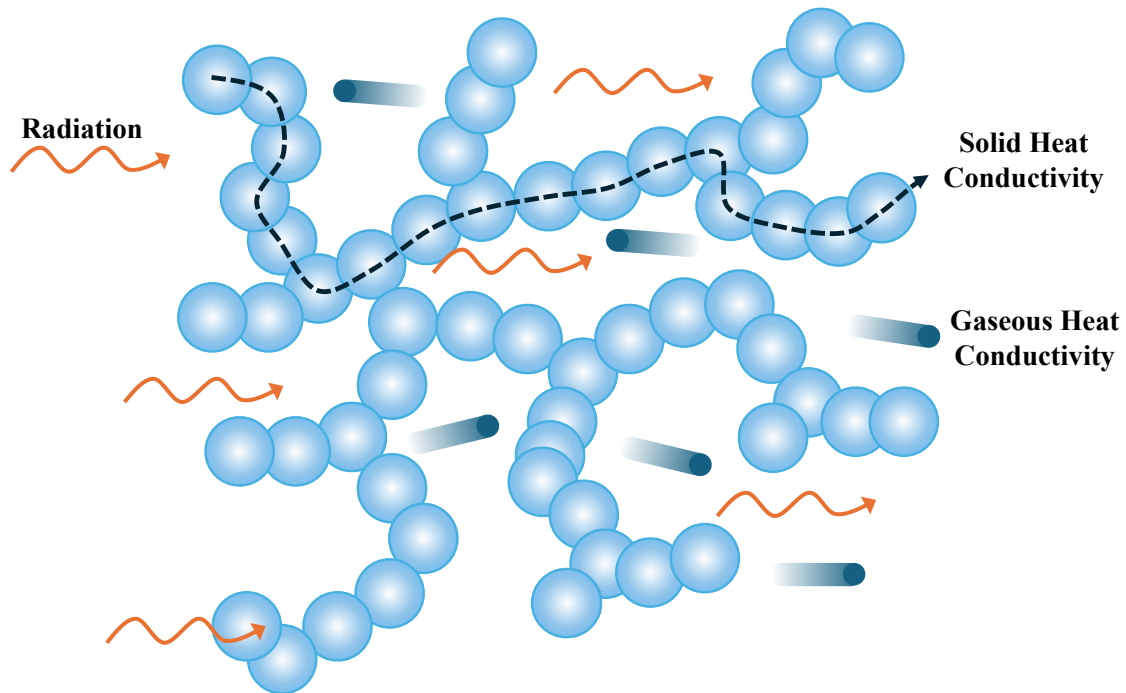


Figure 9: Heat transport mechanisms in aerogel structures due to solid heat conduction, gaseous heat conduction and radiation. Figure in the style of [126].

The amount of heat transferred through the solid backbone of aerogels depends on the structure and the connectivity, as well as the chemical composition. The heat is transferred by the diffusion of phonons along the backbone chain. The mean free path of the phonons (the average distance a phonon can move before colliding with another) is assumed to be far below the dimensions of primary particles of the network. For porous media, the solid thermal conductivity ( $\lambda_s$ ) can be derived by measuring the sound velocity of porous media ( $v$ ) and solid backbone material ( $v_0$ ) as shown in equation (6) [26]:

$$\lambda_s(T) = \lambda_0 \frac{\rho}{\rho_0} \frac{v}{v_0} \quad (6)$$

where  $\rho$  is the density of the porous media and  $\rho_0$  is the density of the backbone material. The amount of heat transferred through the gas phase inside an aerogel is mostly influenced by the size of pores inside the material. For many aerogels, this size is in the micron range or below and therefore aerogels show the potential to reach thermal conductivities below the conductivity of air, *i.e.*,  $0.026 \text{ W m}^{-1}\text{K}^{-1}$ . The heat transfer in the gas phase is typically characterized by the Knudsen number ( $K_n$ ) as shown in equation (7) [26]:

$$K_n = \frac{l_g}{D} \quad (7)$$

with  $l_g$  as mean free path of gas molecules and pore diameter  $D$ . In general, there exist three different cases [26, 35]:

- Molecular heat transfer,  $K_n \gg 1$ : The typical pore size is notably smaller than the average distance gas molecules travel without collisions. Gas molecules primarily collide with the solid structure of the aerogel, leading to a thermal conductivity contribution that increases with the number of gas molecules present.
- Diffusive heat transfer,  $K_n \ll 1$ : The average distance gas molecules travel without collisions is significantly shorter than the typical pore size. Gas molecules primarily collide with each other, representing the classical scenario of diffusive heat transfer. As a result, the thermal conductivity of the gaseous part equals that of free gas, remaining constant regardless of gas pressure under ambient and moderate pressures.
- Transition regime,  $K_n \approx 1$ : Gas molecules collide with both each other and the walls. This phenomenon can be elucidated by incorporating a statistical average mean free path that considers both factors.

In aerogel materials, radiation heat gets absorbed and dispersed from external sources or emitted by the solid skeleton within the porous structure. No scattering can be observed as the pore diameters are typically far smaller than the infrared wavelength [127].

In literature has been reported, that for porous materials with pore diameters smaller than 4 mm, heat transfer generated by convection can be basically ignored [128, 129].

### 2.3.2 Acoustic Insulation

In acoustic or sound insulation, the mechanisms of sound absorption, sound reflection and sound transmission play vital roles in determining the overall effectiveness of the final insulation system (cf. Figure 10). The total incident sound energy ( $E_{total}$ ) can be described as the sum

of energy being absorbed ( $E_{absorbed}$ ), reflected ( $E_{reflected}$ ) and transmitted ( $E_{transmitted}$ ) [130, 131] as shown in the following equation (8):

$$E_{total} = E_{absorbed} + E_{reflected} + E_{transmitted} \quad (8)$$

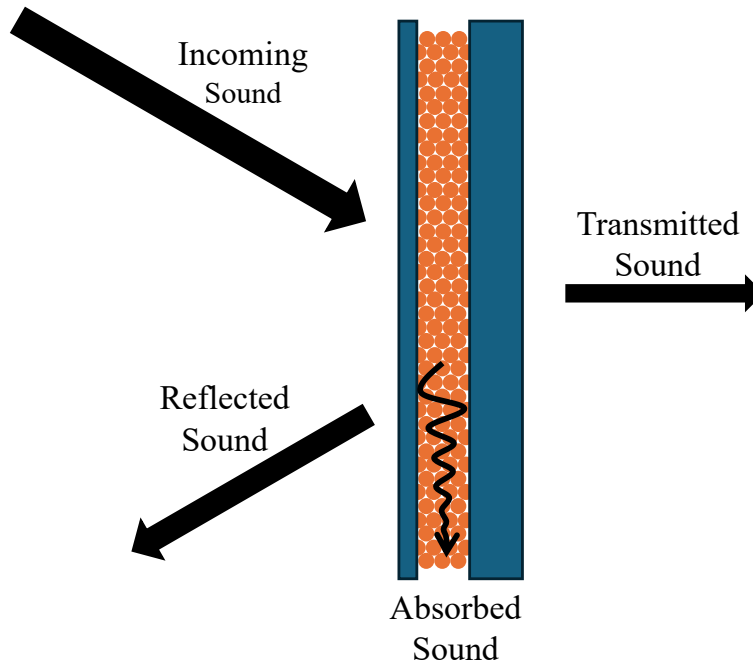


Figure 10: Scheme demonstrating sound reflection, sound absorption and sound transmission. The total incident sound energy is represented as incoming sound.

Sound absorption describes the conversion of sound into other forms of energy such as heat and thereby reducing the amount of energy going through the material. In porous media, the consumption of energy can be described through the following three principles [16, 132]:

- Air molecules vibrate inside the pores and come into contact with the pore walls, which leads to a conversion to thermal energy,
- air gets periodically compressed and released inside the pores due to incoming sound waves and heats up due to the compression,
- acoustic pressure can dissipate energy through the flexible motion of a solid structure and get converted into mechanical energy.

The sound absorption coefficient  $\alpha$  is used to quantify the frequency-dependent absorption behavior of a material and is defined as the ratio of absorbed energy ( $E_{absorbed}$ ) to total incident energy ( $E_{total}$ ) as shown in equation (9). It is typically measured by the use of impedance tubes.

$$\alpha = \frac{E_{absorbed}}{E_{total}} \quad (9)$$

The degree of sound reflection depends on several factors, including the angle of incidence, the nature of the surface material, and the frequency of the sound wave. Smooth, hard surfaces tend

to reflect sound waves more efficiently than soft or irregular surfaces. For instance, reflective surfaces such as concrete walls, glass windows, or metal panels exhibit higher levels of sound reflection compared to porous materials. [133]

Sound transmission refers to the passage of sound waves through the insulation material via various mechanisms, including direct transmission through solid materials, flanking transmission around the edges of barriers, and airborne transmission through leaks or gaps in the insulation system. [133]

Aerogels exhibit significant potential as acoustic insulators. As sound waves infiltrate the porous media, they induce oscillations in air molecules within the pores. The interaction between the gas and the solid framework results in sound energy losses through three distinct mechanisms (cf. Figure 11).

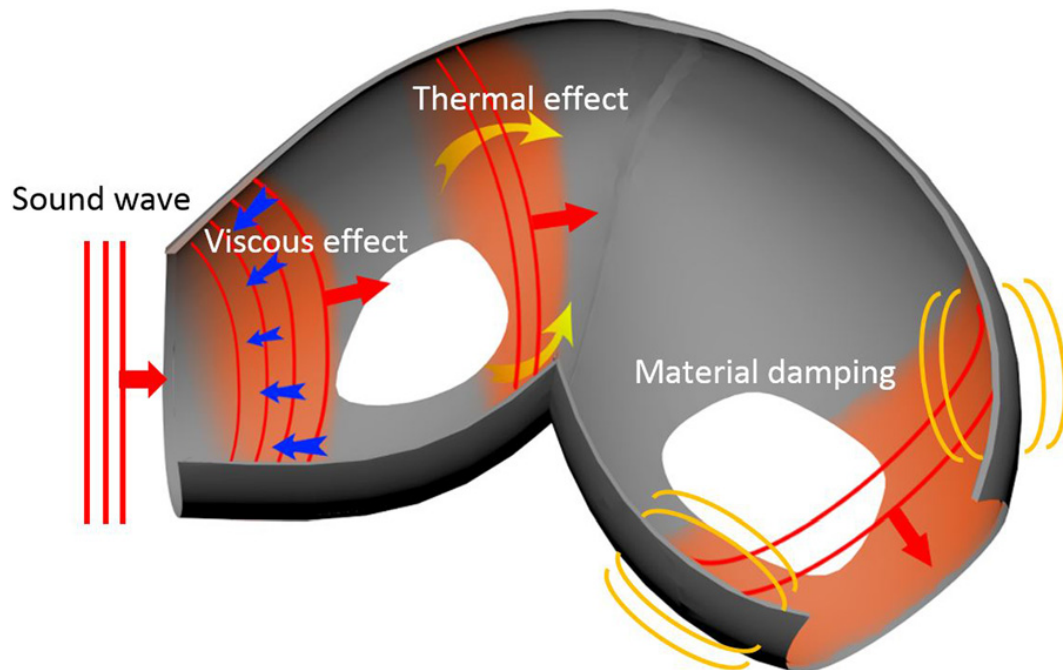


*Figure 11: Schematic presentation of typical sound-absorbing mechanism in porous sound-absorbing materials. Reprinted from [134], with the permission of AIP Publishing LLC.*

The molecules directly hitting the framework exchange energy that aims at thermal equilibrium between the gas and the solid frame. Molecules released from the boundary layer have lower velocity than before and therefore show reduced sound energy. The boundary layer is dependent on the sound frequency: the higher the frequency, the smaller the layer, resulting in a higher significance of this effect for lower frequencies. [135, 136]

Viscous losses are caused by upcoming shear forces at a viscous boundary layer and transfer some of the gas' kinetic energy into heat. These forces have the effect of increasing the gas density and strongly depend on the pore geometry, the dynamic viscosity of gas within the



pores, and the surface available for contact. The effect shows higher significance at lower frequencies. [135, 137]

Flexible motion of solid structure and therefore conversion into mechanical energy is the dominating effect at higher frequencies since viscous and thermal boundary layers are so thin that their contribution is negligible. [135, 136]

### 2.3.3 Commercial Products

Commercially available products depend on the sector in which the material is used, *i.e.* building, transportation, aircraft, or further.

In the building sector, there exists a huge variety of materials. Mineral wool products, mainly glass wool and stone wool, are the biggest classes of insulation materials, followed by expanded and extruded polystyrene (EPS and XPS respectively). Polyurethane (PUR) products are another type of polymeric material. Other materials are often biobased products like wood or straw (cf. Figure 12).

The demand and market value of insulation materials is continuously increasing for the last decades. Six of the ten top players in the thermal insulation market are located in Europe, namely BASF SE (Germany), Kingspan Group (Ireland), Knauf Insulation (Germany), Rockwool International (Denmark), Saint Gobain (France) and Synthos S.A. (Poland). The others are Beijing New Building Material (Group) Co. Ltd. (China), GAF (USA), Johns Manville (USA), and Owens Corning Corporation (USA). [4]

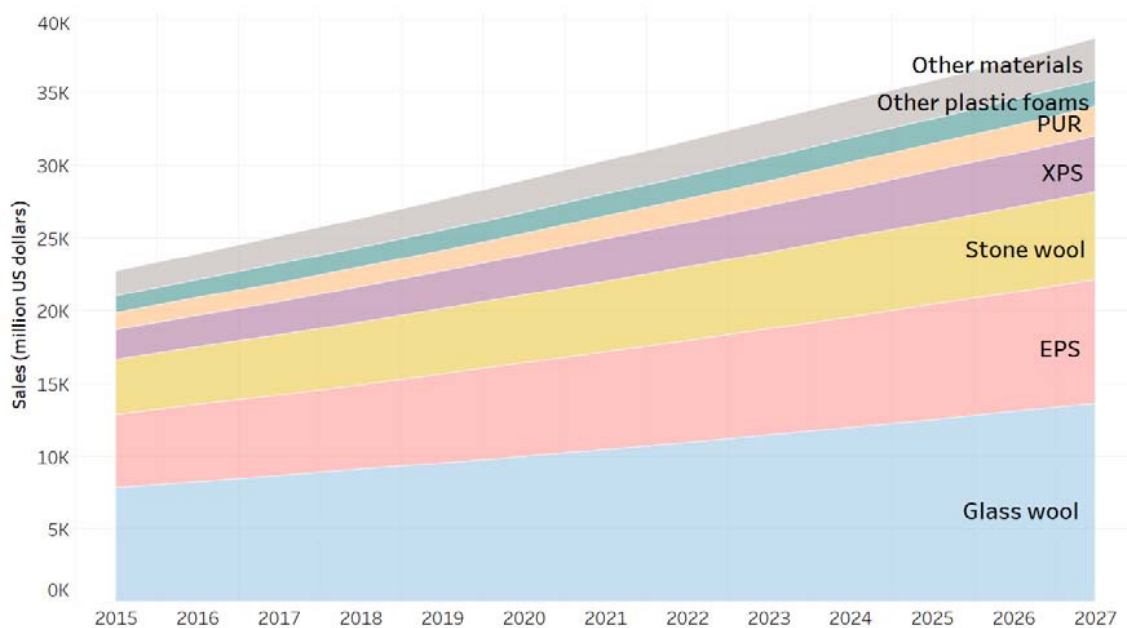


Figure 12: Building thermal insulation global market forecast, by material type. [4] Source: JRC representation with data from Visiongain, 2017.

As many manufacturers do not only sell thermal insulation materials but also acoustic materials, some of the top players are also represented here, *e.g.*, Knauf Insulation, Saint-Gobain, BASF SE, Kingspan Group, Rockwool International, Owens Corning and Johns Manville. Others are 3M (USA), Armacell (Luxembourg), and Huntsman International LLC (USA). [138]

For Aerogels, the total amount of manufacturers with commercially available products is much smaller. Some worldwide companies are listed below [139]:

- Active Aerogels
- Aerogels Technologies LLC
- Aerogel-it GmbH
- Armacell
- Aspen Aerogels Inc.
- Cabot Corporation
- Enersens
- Guangdong Alison Technology Co. Ltd
- Jios Aerogels
- Nano Tech Co. Ltd
- Ningbo Surnano Aerogel Co. Ltd
- Sino Aerogel
- Svenska Aerogel
- Taasi Corporation
- Thermablok Aerogels Limited

Two of the main players in the market are Aspen Aerogels and Cabot Corporation. Aspen Aerogels sells several different products for high temperature (*PYROGEL*<sup>®</sup>), cryogenic (*CRYOGEL Z*<sup>®</sup>), e-mobility batteries (*PYROTHIN*<sup>®</sup>), and subsea (*SPACELOFT*<sup>®</sup>) thermal insulation applications [140]. Cabot Corporation sells aerogel particles (*ENTERA*<sup>®</sup>, *LUMINRA*<sup>®</sup>, *ENOVA*<sup>®</sup>), blankets (*ThermalWrap*<sup>™</sup>), plasters, and compression packs for insulation purposes [141]. It can be observed that none of the aforementioned examples are optimized for the purpose of lightweight insulation in the context of the transportation sector.

### 3 Results and Discussion

This work aimed to reduce the density and optimize the reaction to fire of flexible hybrid-silica aerogels as thermal and acoustic insulation materials for lightweight applications. Therefore, the basic idea was to reduce the amount of the precursors (MTMS and DMDMS) per volume of sol to get a thinner and lighter silica network. The dilution of precursors should theoretically lead to lighter samples at the same volume which results in a reduction of density. To gain more stable samples, especially at a bigger scale (in possible further upscaling) the influence of fiber-matrix aerogel composites is studied. The synthesis of both is very similar and is described in section 4.1.1.

A flame-retardant agent should be incorporated into the aerogel's matrix to optimize the material's reaction to fire. The flame-retardant requirements were as follows: lightweight, durable and non-toxic at combustion. The precursor MTMS was partially substituted by VTMS for the possibility of chemically (and durable) binding the flame-retardant to the aerogel's matrix. The synthesis of vinyl-modified samples is described in section 4.1.2.

The second idea to reduce the density of the final insulation material was to use the natural packing density of spheres and particles. Therefore, a new synthesis procedure for flexible hybrid-silica aerogel particles should be investigated. The particles can be potentially packed and then applied as lightweight thermal and acoustic insulation material. Their synthesis is described in section 4.1.3.

The last idea was to reduce the material's thermal conductivity by incorporating a hydrophobic aerogel material with ultralow thermal conductivities as filler within the "marshmallow-like" hybrid aerogels. By fine-tuning the composition and internal architecture of the resulting aerogel-aerogel composite, the material's thickness can be reduced without compromising its insulating capabilities offering a more lightweight structure. One possibility to synthesize these types of silica aerogel-aerogel composites is described in section 4.1.4.

The following part is divided into first the "Dilution of Precursors", where the results of varying the precursor-to-water-ratio are analyzed. Second, the "Vinyl Modification of Hybrid Aerogels", where a new vinyl precursor is introduced and further functionalized with a flame-retardant agent. Third, the "Synthesis of Particles" is presented. Finally, the "Silica Aerogel-Aerogel Composites" are shown and discussed in detail.

### 3.1 Dilution of Precursors

For density reduction, samples are synthesized with increased water content compared to a standard recipe as a reference. The dilution is done for pure aerogels and aerogel composites, where PET fiber mats are incorporated into the aerogel's sol during synthesis. The synthesis is described in section 4.1.1 "Synthesis of MTMS-DMDMS-based Monolithic Aerogels".

In the following paragraphs, first, the results of the characterization of pure hybrid-silica aerogel samples are described. Second, the results of aerogel composite samples are discussed. Finally, pure and composite aerogels are compared with each other.

This chapter's samples are named alphabetically from **a** to **g**. The index "**\_f**" is added for composite samples containing fibers. For example, sample **a** represents the reference sample with a water-to-MTMS ratio of 39.65. Sample **a\_f** represents the reference sample as a composite with fibers.

#### 3.1.1 Pure Aerogels

The chapter "Pure Aerogels" is partly based on the following publication:

Steffens, K., Bialuschewski, D. and Milow, B., *Tuning density and morphology of organic-inorganic hybrid-silica aerogels through precursor dilution for lightweight applications*. J. Sol-Gel Sci. Technol., 2024. **112**(3): p. 768-775. doi:10.1007/s10971-024-06572-w [142]

The content is reprinted with permission from the Journal of Sol-Gel Science and Technologies. The content and structure are adjusted to the style and layout of this work by adapting the numbering of sections, references, and figures as well as the spelling. Additional data from the Supporting Information was included in the appendix and data of the sound insulation properties were added.

##### 3.1.1.1 Density, Microstructure, and Surface Chemistry

Table 1 shows the mean values for  $\rho_{env}$ ,  $\rho_{skel}$ ,  $\Phi$ , and  $S_R$  of all synthesized samples, per variation of at least eight in two different cylindrical shapes. The errors are calculated as standard deviation from mean values. With a higher amount of water, the samples resulted in lower envelope densities. For every dilution level the "all"-series shows slightly lower densities compared to the "water"-series. The lightest samples **e** exhibited a 38% lower density with  $0.066 \text{ g cm}^{-3}$  compared to references **a** having  $0.106 \text{ g cm}^{-3}$ . Skeletal density for all samples was observed in the same range of  $1.26$  to  $1.32 \text{ g cm}^{-3}$ . Since the solid composition of the final material (MTMS:DMDMS-ratio) is not varied, this result was expected. The porosity changes

similar to the envelope density, as it increases with dilution. The measured radial shrinkage is 2 – 3% for all samples within their error.

Table 1: Envelope and skeletal density of samples with their respective calculated porosity and measured radial shrinkage. The error of all skeletal density measurements is  $\pm 0.01 \text{ g cm}^{-3}$ .

Sam- ple	H <sub>2</sub> O: MTMS -ratio	Envelope density		Skeletal density		Porosity		Radial shrinkage	
		$\rho_{\text{env}}$ [g cm <sup>-3</sup> ]		$\rho_{\text{skel}}$ [g cm <sup>-3</sup> ]		$\Phi$ [%]		$S_r$ [%]	
		all	water	all	water	all	water	all	water
<b>a</b>	39.65	0.106 ± 0.002		1.26		91.6		2.3 ± 0.5	
<b>b / c</b>	50.00	0.086 ± 0.003	0.089 ± 0.004	1.29	1.28	93.3	93.1	2.5 ± 0.7	2.0 ± 0.3
<b>d / e</b>	55.00	0.079 ± 0.002	0.086 ± 0.005	1.26	1.32	93.8	93.5	1.7 ± 0.5	3.2 ± 1.2
<b>f / g</b>	60.00	0.071 ± 0.005	0.077 ± 0.006	1.31	1.27	94.6	94.0	2.4 ± 1.2	3.0 ± 1.3
<b>h / i</b>	65.00	0.066 ± 0.003	0.073 ± 0.002	1.29	1.29	94.9	94.3	2.7 ± 0.9	2.2 ± 0.6

Scanning electron images of the flexible silica aerogels are shown in Figure 13. It can be observed that each sample consists of micrometer-sized spherical particles connected via inter-particle necks. The dilution of the precursors led to smaller particles, as the total mass, coming solely from the amount of precursor used, stayed constant while the total volume increased. The diameter of the particles is determined by averaging the size of 20 particles for each sample as shown in Table 2 ( $D_{SEM}$ ). It decreased with increasing dilution of siloxane precursors from 8.2  $\mu\text{m}$  for reference a down to 3.2 and 3.3  $\mu\text{m}$  for samples **h** and **i**. Every level of dilution shows comparable morphology and particle diameters for each dilution in both “water” and “all”-series. Both samples with water:MTMS-ratio of 65.00 showed a rougher particle surface (Figure 13, **h** and **i**). The thickness of inter-particle necks seems to be stable for all synthesized samples due to the adjusted aging time from one up to seven days for higher diluted samples. Higher diluted samples without increasing the aging time could not successfully be synthesized during the experiments due to their very fragile structure. While demolding and washing the samples break apart very easily. After longer aging the particle necks grow due to Ostwald ripening [143, 144] and the samples can withstand higher external forces.

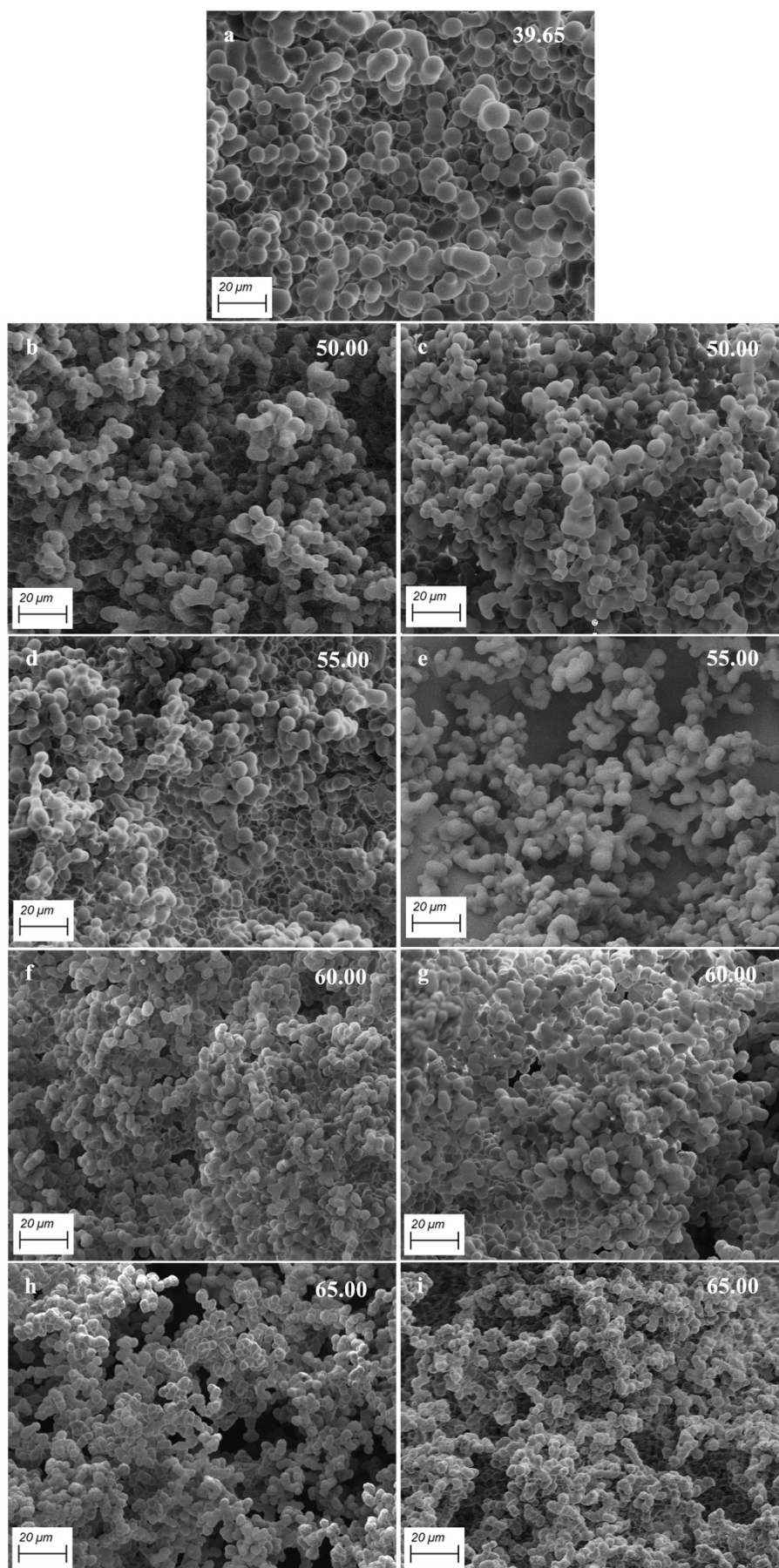


Figure 13: Scanning electron microscope images derived from reference sample **a** and modified samples (**b – i**). The left column represents the “all”-series and the right column the “water”-series. The particle size decreased with increasing dilution.

The water drop contact angles  $\theta_c$  of the samples are listed in Table 2. The measured angles are in the range from  $129^\circ$  up to  $140^\circ$  for all synthesized samples (**a** – **i**). These results lead to the assumption that the hydrophobicity of the final material is not influenced by the dilution of siloxane precursors during synthesis, as expected, as the amount of hydrophobic Si-CH<sub>3</sub> groups covering the surface should not be influenced significantly. Venkateswara Rao *et al.* observed similar behavior for pure MTMS-based systems [145]. In Figure 14 are shown a 5.0  $\mu$ L water droplet on top of the samples **a** – **i**. The high hydrophobicity prevents the material from gaining weight due to moisture condensation and influences other properties such as thermal conductivity or acoustic properties.

Table 2: Mean particle size calculated from SEM images and water drop contact angle determined by drop shape analyzer.

Sample	H <sub>2</sub> O:MTMS -ratio	Mean particle size		Water drop contact angle	
		$D_{SEM}$ [ $\mu$ m]		$\theta_c$ [ $^\circ$ ]	
		all	water	all	water
<b>a</b>	39.65	8.2 $\pm$ 1.2		136	
<b>b / c</b>	50.00	5.6 $\pm$ 1.0	5.3 $\pm$ 0.9	140	129
<b>d / e</b>	55.00	5.2 $\pm$ 0.8	4.7 $\pm$ 0.7	127	138
<b>f / g</b>	60.00	3.9 $\pm$ 0.6	3.9 $\pm$ 0.4	140	129
<b>h / i</b>	65.00	3.3 $\pm$ 0.5	3.4 $\pm$ 0.6	137	135

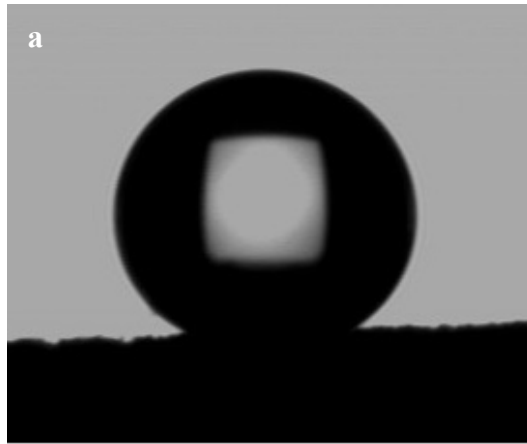


Figure 14: Image of 5.0  $\mu$ L water droplet on sample **a**. All calculated water drop contact angles are listed in Table 2. Further images of samples **b** – **i** are shown in the appendix (cf. Figure A 2).

### 3.1.1.2 Thermal Properties

HFM studies were carried out in the range of 0 – 60 $^\circ$ C and are shown in Figure 15. Samples **a** – **e** and **g** could be synthesized in the required dimensions of minimum 200 x 200 mm<sup>2</sup> in a special self-made mold. Samples **f**, **h** and **i** were broken during the washing steps due to their very fragile nature caused by bigger dimensions. In general, smaller samples are easier to handle. The thermal conductivity increases with higher temperatures for all samples, as known

from the literature [128, 146, 147]. Dai *et al.* observed the same temperature dependency for other types of silica aerogels as the gas thermal conductivity, solid thermal conductivity and radiative thermal conductivity are all related to the temperature and, therefore, show the before observed behavior on the effective thermal conductivity [148]. The dilution seems to have no major influence on the measured thermal conductivities. Within the precision of the system, all samples show similar values, which vary in a range from minimum  $\sim 30 \text{ mW m}^{-1} \text{ K}^{-1}$  at  $0^\circ\text{C}$  up to  $\sim 37 \text{ mW m}^{-1} \text{ K}^{-1}$  at  $60^\circ\text{C}$  for all samples. For sample g with the lowest density of all synthesized mats ( $0.077 \text{ g cm}^{-3}$ ) a thermal conductivity of  $\sim 32.5 \text{ mW m}^{-1} \text{ K}^{-1}$  at  $25^\circ\text{C}$  was measured, which is in the lower range. The measured conductivities could be confirmed with values from the literature [76, 92].

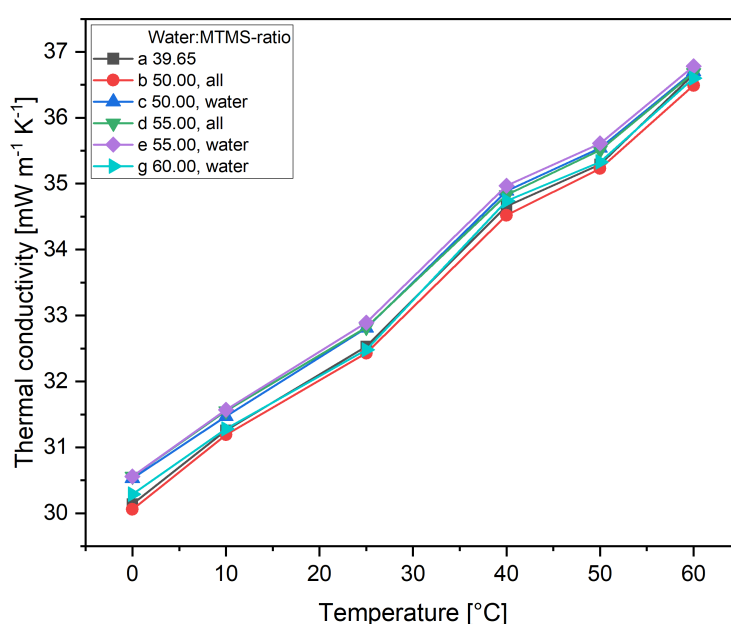


Figure 15: Thermal conductivity of samples in the temperature range of  $0 - 60^\circ\text{C}$ . The thermal conductivity is increased with increasing temperature. Diluted samples and standard ones did not differ much from each other.

### 3.1.1.3 Mechanical Properties

While classical silica aerogels show a hard and brittle nature, organic-inorganic hybrids are soft and flexible. Therefore, the samples are compressed uniaxially up to a strain ( $\epsilon$ ) of 60%. After compression, the samples were unloaded and immediately recovered to their original height without any visible macroscopic damage. The measured stress-strain curves are shown in Figure 16 (left). All samples showed a linear elastic behavior up to  $\epsilon < 20\%$ . As visible in Figure 16 (right), a buckling of the sample occurs at some point, which leads to an increase in the diameter of the sample. This influences the stress as it is calculated via the force divided by the cross-sectional area. For lower strains, this effect can be neglected and therefore Young's



modulus  $E$  was calculated from the stress-strain curves in the linear range from 0 to 10% compression strain (cf. Table 3).

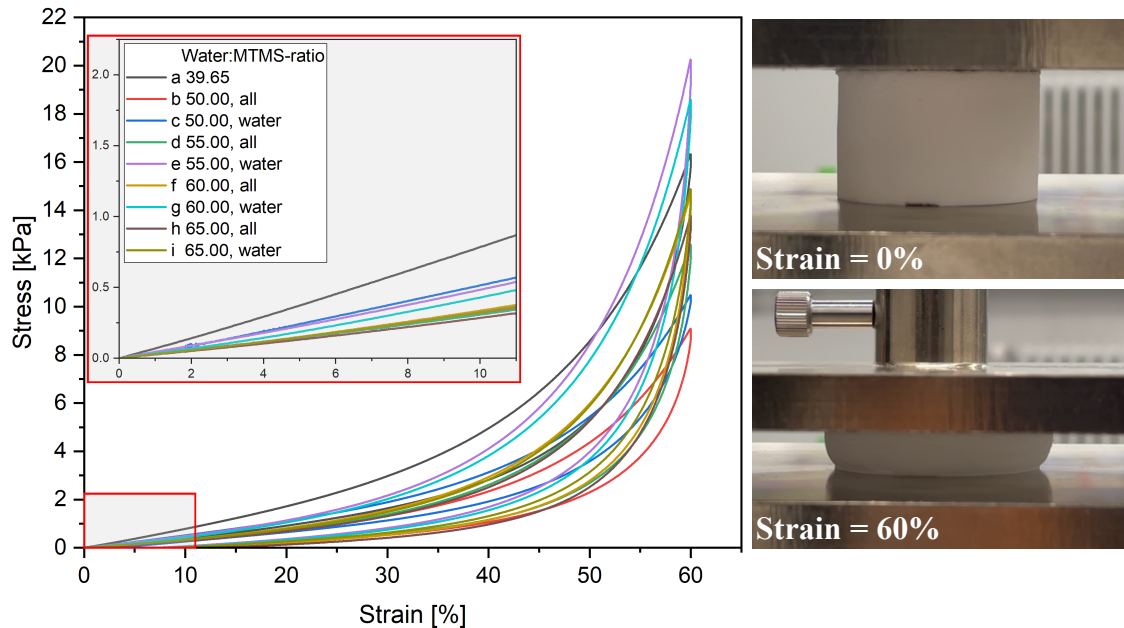


Figure 16: Uniaxial stress-strain curve (left) and sample images of compression testing at 0% and 60% strain (right). After testing the samples spring back to their original height. More detailed single stress-strain curves are shown in the appendix (cf. Figure A 3)

The highest Young's modulus (7.89 kPa) compared to the diluted samples was measured for the reference sample a. Samples from the "water"-series (**c**, **e**, **g**, **i**) show generally higher values than samples from "all"-series (**b**, **d**, **f**, **h**). A decrease in Young's modulus with increasing water:MTMS-ratio for samples **c**, **e**, **g** and **i** was measured (from 5.22 to 3.23 kPa), for samples **b**, **d**, **f** and **h** no influence of dilution could be observed on the calculated Young's moduli ( $\sim 3$  kPa). A decrease in Young's modulus with increasing dilution was expected because of the weaker solid backbone structure. The samples' elastic moduli are comparable to literature values: Even though Hayase *et al.* as well as Rege *et al.* did not calculate Young's moduli, the slopes of measured stress-strain curves are comparable to the herein investigated samples [61, 76]. Ehgartner *et al.* presented Young's moduli in the range of 4 – 12 kPa for comparable organofunctional flexible silica aerogels [65].

Table 3: Young's modulus  $E$  calculated in the linear range of stress-strain-curves from 0 to 10% strain for samples  $a - i$ .

Sample	H <sub>2</sub> O:MTMS -ratio	Young's modulus $E$ [kPa]	
		all	water
<b>a</b>	39.65	7.89	
<b>b / c</b>	50.00	3.08	5.22
<b>d / e</b>	55.00	3.03	4.81
<b>f / g</b>	60.00	3.36	4.30
<b>h / i</b>	65.00	2.82	3.23

To study the influence of aging on the mechanical behavior of samples, reference sample **a** was additionally synthesized with three and seven days of aging. The resulting stress-strain curves are presented in the appendix (cf. Figure A 4). Differing the aging time can lead to slightly harder material.

#### 3.1.1.4 Sound Insulation Properties

To gain information on the sound insulation performance of the synthesized pure flexible silica aerogels, the sound absorption coefficients and transmission loss were measured and calculated. The results are shown in Figure 17 and Figure 18 respectively. It can be seen that all measured sound absorption curves were in the same range even though they differ in mass with one exception: sample **d** showed higher absorption at  $\sim 600$  Hz and  $\sim 900 - 1200$  Hz, but lower absorptions in the range from  $\sim 1400 - 1900$  Hz.

Beside sample **d**, samples **c** and **e** with a higher mass show higher absorptions in the range of  $700 - 1400$  Hz than **a**, **b** and **g**. This can be explained due to the mass effect which typically leads to higher adsorptions at lower frequencies combined with their specific microstructure [136]. Samples **c**, **d** and **e** show the highest masses even though their density is lower than for sample **a** for example. The higher masses for the cut samples are caused by the difficult preparation of flexible samples for the measurement.

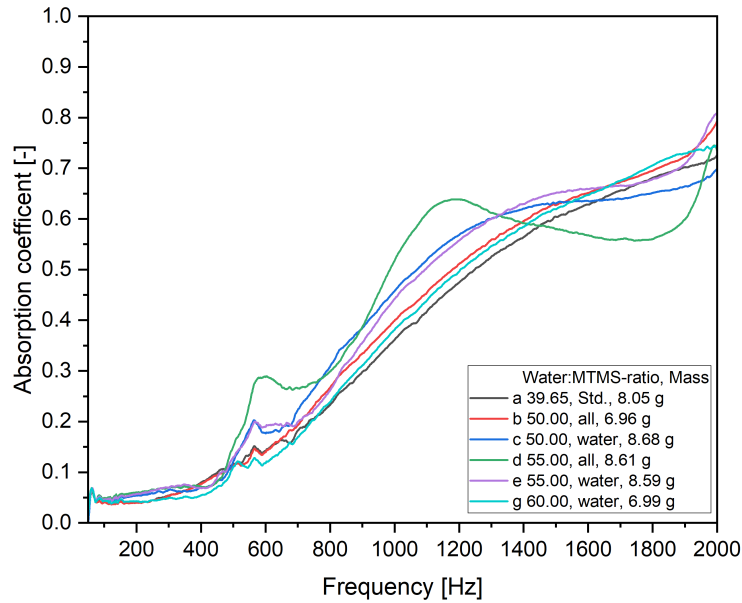


Figure 17: Frequency-dependent sound absorption coefficient  $\alpha$  of pure aerogel samples in the range of 50 – 2000 Hz. The absorption coefficient increased with increasing frequencies as expected.

For the sound transmission loss shown in Figure 18, it could be observed that especially at lower frequencies  $< 500$  Hz the obtained curves differ a lot. While samples **a** and **b** show low transmission loss (2 – 8 dB), samples **c** – **g** show much higher values (2 – 14 dB). Samples **a** and **b** had a maximum at  $\sim 75$  Hz followed by a minimum of around 100 Hz. For samples **c** – **g** this maximum was wider at around 50 – 200 Hz, followed by a minimum at around 350 Hz. This shift can be explained as follows: Since it was observed that samples **a** and **b** were slightly thinner than the others, they were not as compressed as samples **c** – **g** inside the sample holder which resulted in different stiffnesses of the samples inside the sample holder. Since the transmission loss is strongly stiffness-controlled at lower frequencies, this could have caused the observed effect. The observed minima are typical and represent the first resonance frequencies of the samples. At higher frequencies, the transmission loss followed primarily a function of its mass: Merli *et. al* observed similar behavior for TMOS-based aerogels, in agreement with others. [108, 136, 149]

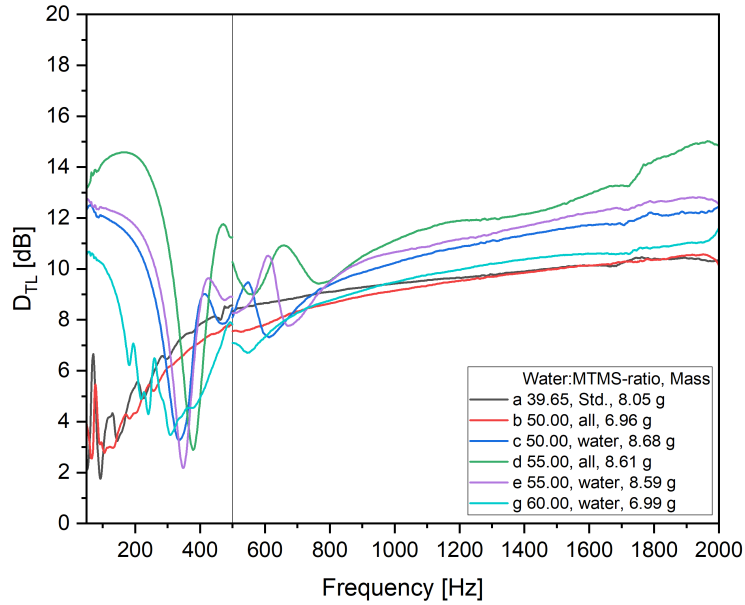


Figure 18: Frequency-dependent sound transmission loss of pure aerogel samples in the range of 50 – 2000 Hz. At 500 Hz the measurements of low frequency and high frequency were combined, resulting in small deviations at this point. The sample *d* showed the highest transmission loss values. The first resonance frequency of samples *a* – *b* could be observed at ~ 100 Hz and at 300 – 400 Hz for samples *c* – *g*.

### 3.1.2 Aerogel Composites

#### 3.1.2.1 Density, Microstructure, and Surface Chemistry

Table 4 shows the mean values for  $\rho_{env}$ ,  $\rho_{skel}$ ,  $\Phi$ , and  $S_R$  of all synthesized samples, per variation at minimum six in cylindrical shapes. The errors were calculated as standard deviations from their mean values. With a higher amount of water, the samples resulted in lower envelope densities. For every dilution level the “all”-series shows slightly lower densities compared to the “water”-series. The lightest samples *f*–*f* exhibited a 31% lower density with  $0.070 \text{ g cm}^{-3}$  compared to references *a*–*f* with a density of  $0.102 \text{ g cm}^{-3}$ . Skeletal density for all samples was observed in the range of  $1.32$  to  $1.49 \text{ g cm}^{-3}$ . Since the solid composition of the final material (MTMS/DMDMS-ratio to PET matrix) is varied, this result was expected. The skeletal density of the pure PET-fiber matrix was measured at  $1.53 \text{ g cm}^{-1}$ . With a lower concentration of precursors per volume but still the same amount of PET fibers, the skeletal density has to increase, following the rule of mixtures. The porosity changes similar to the envelope density, as it increases with dilution. The measured radial shrinkage is low with  $0$  –  $1.4\%$  for all samples within their errors. The fiber matrix leads to improved spring-back properties during/after ambient drying resulting in generally lower radial shrinkage and stable geometries.

Table 4: Envelope and skeletal density of samples with their respective calculated porosity and measured radial shrinkage. The error of all skeletal density measurements is  $\pm 0.01 \text{ g cm}^{-3}$ .

Sample	$\text{H}_2\text{O}:$ MTMS -ratio	Envelope density		Skeletal density		Porosity		Radial shrinkage	
		$\rho_{\text{env}}$ [g cm <sup>-3</sup> ]		$\rho_{\text{skel}}$ [g cm <sup>-3</sup> ]		$\Phi$ [%]		$S_r$ [%]	
		all	water	all	water	all	water	all	water
<b>a_f</b>	39.65	0.102 $\pm$ 0.002		1.32		92.3		0.3 $\pm$ 0.5	
<b>b_f / c_f</b>	50.00	0.084 $\pm$ 0.002	0.088 $\pm$ 0.002	1.38	1.33	93.9	93.4	0.1 $\pm$ 0.4	0.4 $\pm$ 0.3
<b>f_f / g_f</b>	60.00	0.070 $\pm$ 0.002	0.072 $\pm$ 0.004	1.42	1.49	95.1	95.2	1.4 $\pm$ 1.2	0.7 $\pm$ 0.5

Scanning electron images of the flexible silica aerogel composites are shown in Figure 19. It can be observed that for each sample the micrometer-sized spherical particles kind of embed the fiber matrix. A shell is formed around the fibers. Defects in this shell can be a result of the sample preparation process since the flexible and soft aerogel composites are hard to cut for this measurement. The dilution of the precursors was leading to smaller particles, as expected. Every level of dilution shows comparable morphology and particle diameters for each dilution in both “water” and “all”-series.

The water drop contact angle  $\theta_c$  was measured exemplary six times for samples **a\_f** (cf. Figure 20) and a mean value of  $132^\circ$  is determined. Since the water droplet itself does not get in contact with the fiber matrix, a change in the hydrophobicity of the fiber-reinforced samples and the non-reinforced ones is not given.

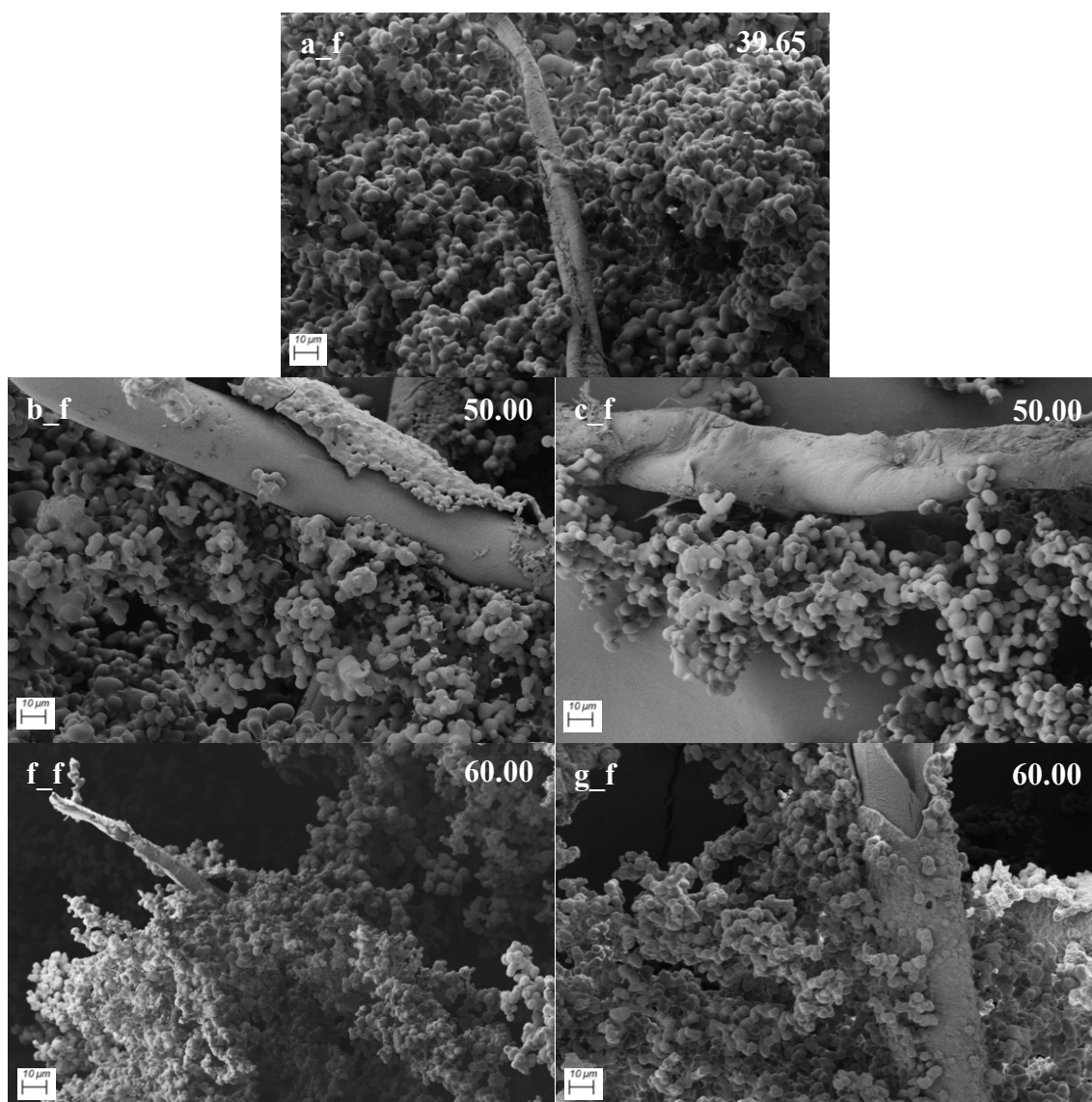


Figure 19: Scanning electron microscope images derived from reference sample **a\_f** and modified samples (**b\_f**, **c\_f**, **f\_f**, **g\_f**). The left column represents the “all”-series and the right column the “water”-series.

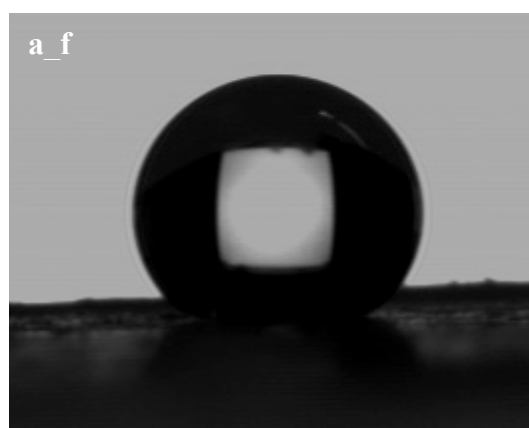


Figure 20: Photograph of 5.0  $\mu\text{L}$  water droplet on reference sample **a\_f**. A water drop contact angle of  $132^\circ$  is determined for this sample.

### 3.1.2.2 Thermal Properties

HFM studies were carried out for samples **a\_f** – **c\_f** in the range of 0 – 60°C and are shown in Figure 21. As expected, the thermal conductivity increased at higher temperatures for all samples and for the diluted samples no major effect on the measured thermal conductivities is observed. Within the expected precision of the system, all samples show similar values, which vary in the range of around 31.5 mW m<sup>-1</sup> K<sup>-1</sup> at 0°C up to 38.5 mW m<sup>-1</sup> K<sup>-1</sup> at 60°C for all samples. Samples **b\_f** and **c\_f** with the lowest density for all synthesized mats (0.084 and 0.088 g cm<sup>-3</sup> respectively) show a thermal conductivity of ~ 34 mW m<sup>-1</sup> K<sup>-1</sup> at 25°C, which is in the lower range. The measured conductivities could be confirmed with values from the literature: Rege *et al.* measured thermal conductivities for several kinds of marshmallow fiber-composites in the range of 33 – 35 mW m<sup>-1</sup> K<sup>-1</sup> at 25°C [76].

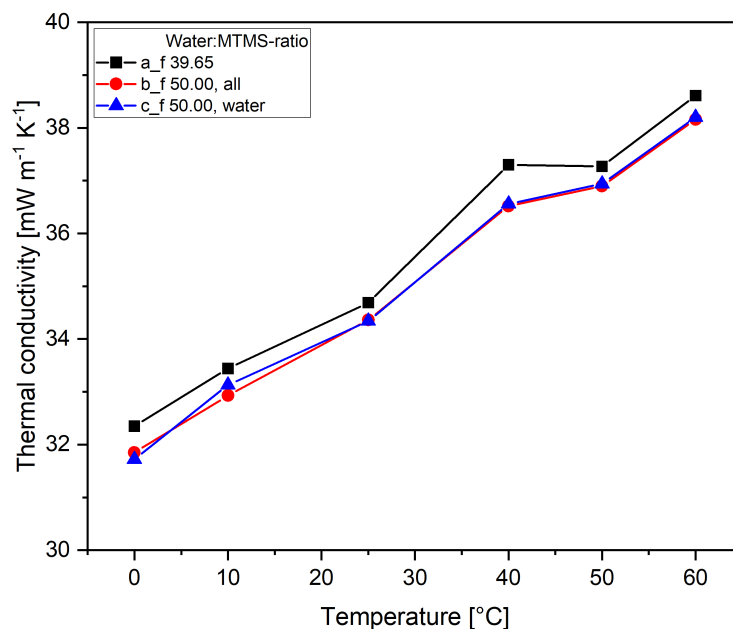


Figure 21: Thermal conductivity of composite samples **a\_f** – **c\_f** in the temperature range of 0 – 60°C. The thermal conductivity increased with increasing temperature as expected. All samples showed similar values in the range of the measurement precision.

### 3.1.2.3 Mechanical Properties

To determine the mechanical properties of the synthesized aerogel composites the samples could be compressed uniaxially up to 60% strain. After compression, the samples were unloaded and immediately recovered to their original height without any visible damage. The measured stress-strain curves are shown in Figure 22. All samples show a linear-elastic behavior up to  $\epsilon < 20\%$ . The final composite samples noticeably benefit from improved handling and possibly easier application.

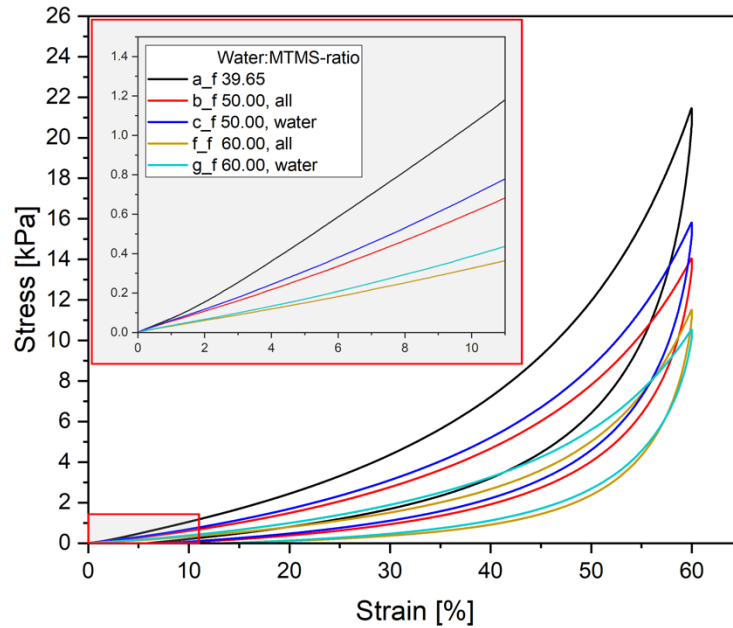


Figure 22: Uniaxial stress-strain-curve of composite samples **a\_f**–**c\_f**, **f\_f** and **g\_f**. More detailed single stress-strain curves are shown in the appendix (cf. Figure A 6).

From the stress-strain curves the Young’s modulus  $E$  is calculated in the linear range from 0 to 10% compression strain as shown in Table 5. For reference sample **a\_f** the highest Young’s modulus with 9.01 kPa was observed. With increasing dilution, the samples get softer and the calculated Young’s moduli get therefore smaller. For the “all”-series generally smaller values than the “water”-series were obtained. The measured Young’s moduli dropped down to 2.97 kPa for sample **f\_f** and 3.67 kPa for **g\_f**.

Table 5: Young’s modulus  $E$  calculated in the linear range of stress-strain-curves from 0 to 10% strain for samples **a\_f**–**c\_f** and **f\_f**–**g\_f**.

Sample	H <sub>2</sub> O:MTMS -ratio	Young’s modulus $E$ [kPa]	
		all	water
<b>a_f</b>	39.65	9.01 ± 1.92	
<b>b_f / c_f</b>	50.00	5.74 ± 0.74	6.11 ± 0.77
<b>f_f / g_f</b>	60.00	2.97 ± 0.23	3.67 ± 0.72

### 3.1.2.4 Sound Insulation Properties

To obtain information on the sound-insulating properties of the synthesized composite silica aerogels, the sound absorption coefficients and transmission loss were measured and calculated. The results are shown in Figure 23 and Figure 24 respectively. The measured values of the samples **a\_f** to **c\_f** show similar sound absorption properties even though they differ in mass. In the lower frequency region from 50 to 300 Hz, the three curves did not differ from each other.



In the frequency region from 300 to 1300 Hz, sample **a\_f** with the highest mass showed the highest absorption coefficient. This could be explained by the typical shift of absorption coefficients to higher values with increasing mass [136]. In the upper region from 1300 to 2000 Hz, the samples **b\_f** and **c\_f** showed higher absorption coefficients. This can be explained due to their higher porosity and potentially smaller pores (smaller than that of the mean-free path of the air molecules), which led to improved sound absorption [136].

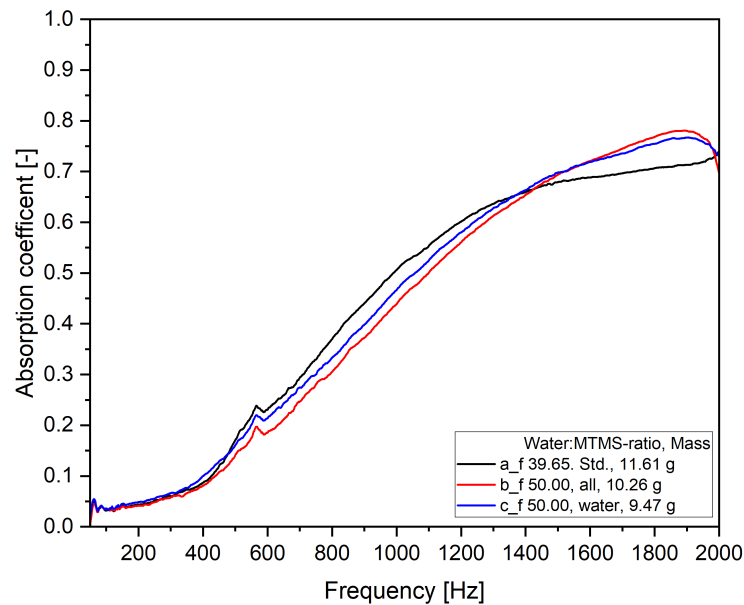


Figure 23: Frequency-dependent sound absorption coefficient  $\alpha$  of composite aerogel samples in the range of 50 – 2000 Hz. The absorption coefficient increased with increasing frequencies, as expected.

For the sound transmission loss shown in Figure 24, it could be observed that the sample **a\_f** with the highest mass showed the highest transmission loss in the full measured frequency range (50 – 2000 Hz). Long and others have reported on this phenomenon, stating that absorbing materials follow the law of mass [108, 149, 150]. Samples **b\_f** and **c\_f** show similar values since their mass does not differ as much as compared to **a\_f**.

The curves generally showed typical progressions: High transmission loss values at low frequencies represent the higher stiffness-controlled region. The greater the bending stiffness and the shorter the span, the higher the transmission loss. This region is followed by a drop in transmission loss at the first resonance frequency of the sample. Above this, the transmission loss primarily followed a function of its mass, as Merli *et al.* showed for TMOS-based monolithic aerogels. [149]

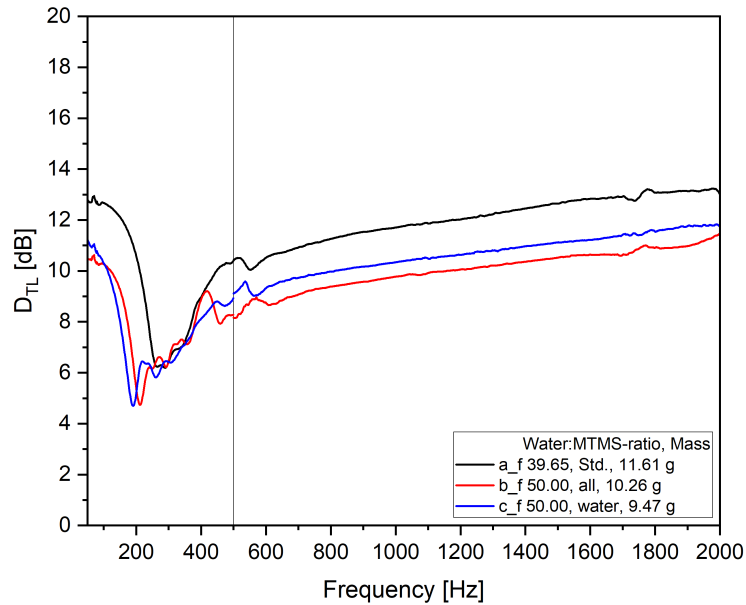


Figure 24: Frequency-dependent sound transmission loss of composite aerogel samples in the range of 50 – 2000 Hz. At 500 Hz, the measurements of low frequency and high frequency were combined, resulting in small deviations. The sample *a\_f* with the highest mass showed the highest transmission loss values. The first resonance frequency of the samples could be observed at 200 – 300 Hz.

### 3.1.3 Comparison of Aerogels and Aerogel-Composites

In Figure 25 the mean values for  $\rho_{skel}$  from Table 1 and Table 4 are shown. The density decreased with increasing water ratio for series “all” and “water”. Within their errors, samples with fiber matrix showed the same densities as samples without fiber matrix. This can be explained by the slightly less shrinkage of composite samples (0 – 1.5 % compared to 2 – 3 %) due to improved spring-back effect after drying. This resulted in lower densities compared to the pure aerogel samples, although the weight is higher due to the additional fiber matrix.

The general trend of density decrease for both series was expected since there is less material (precursors) to form the solid backbone for the same volume. This could also be seen in the SEM images, which were taken from pure aerogel samples (cf. Figure 13) and composite samples (cf. Figure 19). They all showed comparable morphology and particle diameters for each dilution.

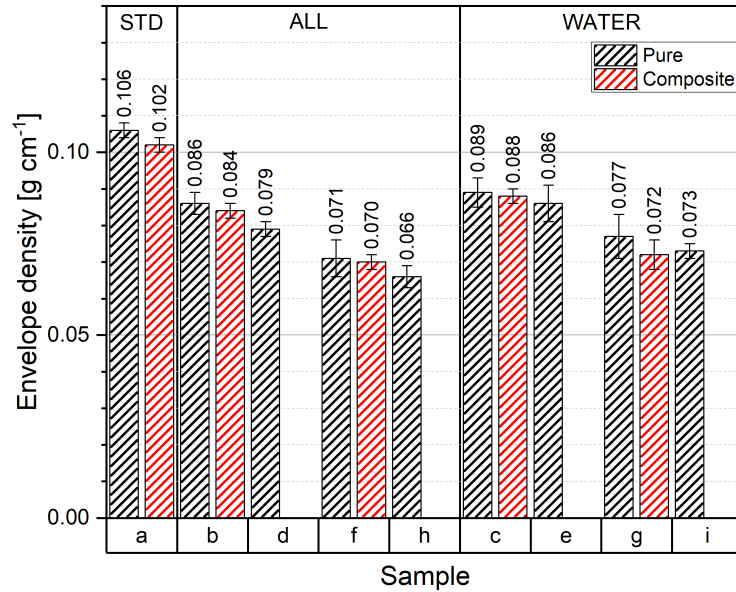


Figure 25: Comparison of envelope density for pure and composite aerogels. The higher the dilution, the lower the densities, as it was expected. Composite samples showed at the same dilution identical densities within their errors.

The observed thermal conductivities of composite materials are about  $2 \text{ mW m}^{-1} \text{ K}^{-1}$  higher than for the pure aerogel samples in the measured range from  $0 - 60^\circ\text{C}$ . Nevertheless, the dilution shows no significant change in thermal conductivity for either composite or pure aerogel samples, as shown in Figure 26 for  $25^\circ\text{C}$  as an example, and was not influenced by the different densities within the range of all studied samples. While Iswar *et al.* observed a change in thermal conductivities with decreasing densities for another type of silica aerogels, this could not be confirmed for the here synthesized samples [151]. A potential reason for this can be found in the structure of the synthesized aerogels: As the particle necks inside the structure were observed at almost the same thickness (as discussed in 3.1.1.1 “Density, Microstructure, and Surface Chemistry”), the main heat transfer through the solid network structure was expected in the same range for all samples resulting in similar measured thermal conductivities. The thermal conductivity of pure aerogels is given  $32.5 \text{ mW m}^{-1} \text{ K}^{-1}$  at  $25^\circ\text{C}$  while for composites at around  $34.5 \text{ mW m}^{-1} \text{ K}^{-1}$  at  $25^\circ\text{C}$ . Both could be confirmed with values from literature observed by Rege *et al.* for a quite similar system [76].

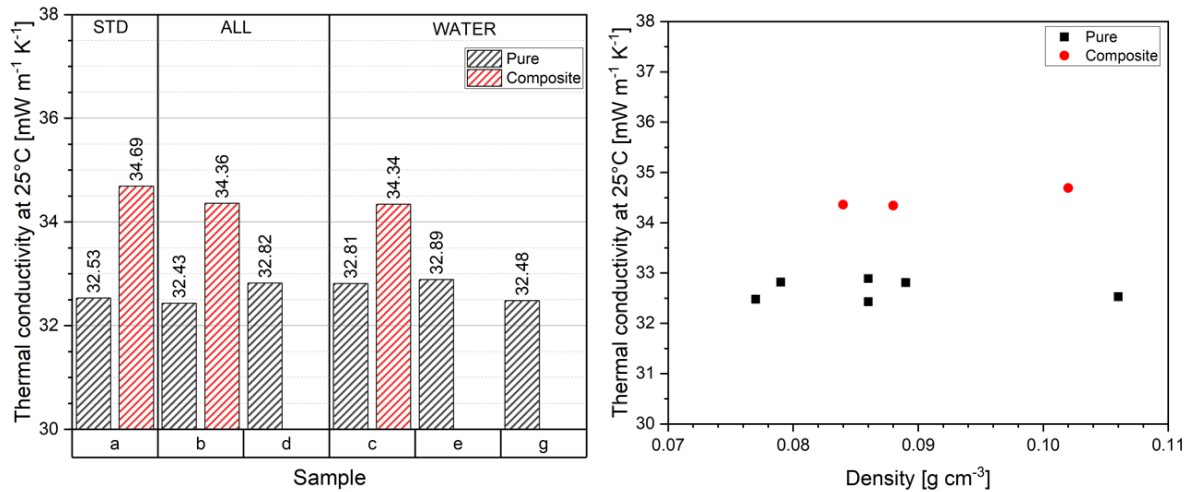


Figure 26: Comparison of thermal conductivity at 25°C for pure and composite aerogels. The change in densities did not influence the measured thermal conductivities, neither for pure aerogels ( $\sim 32.5 \text{ mW m}^{-1} \text{ K}^{-1}$ ) nor for composite samples ( $\sim 34.5 \text{ mW m}^{-1} \text{ K}^{-1}$ ).

Composites, as well as pure aerogels, showed a soft and flexible nature. With increasing dilution, the samples became perceptibly softer. This could be confirmed with the calculated Young's moduli: the higher the dilution, the lower the Young's modulus of the sample. Composites, due to their additional fiber matrix, show slightly higher or identical values for  $E$  within their errors.

The obtained Young's moduli followed somehow a function of density. Fricke as well as Pekala *et al.* presented a power law relationship ( $E \sim \rho_{bulk}^\alpha$ ) between the mechanical properties of silica aerogels and their bulk density ( $\rho_{bulk}$ ) [152, 153]. Several similar studies are known and came to the same results with other silica-based aerogels [151, 154]. Especially for larger-sized mats, it can be observed that the implementation of fibers is beneficial for the handling and application of the final material.

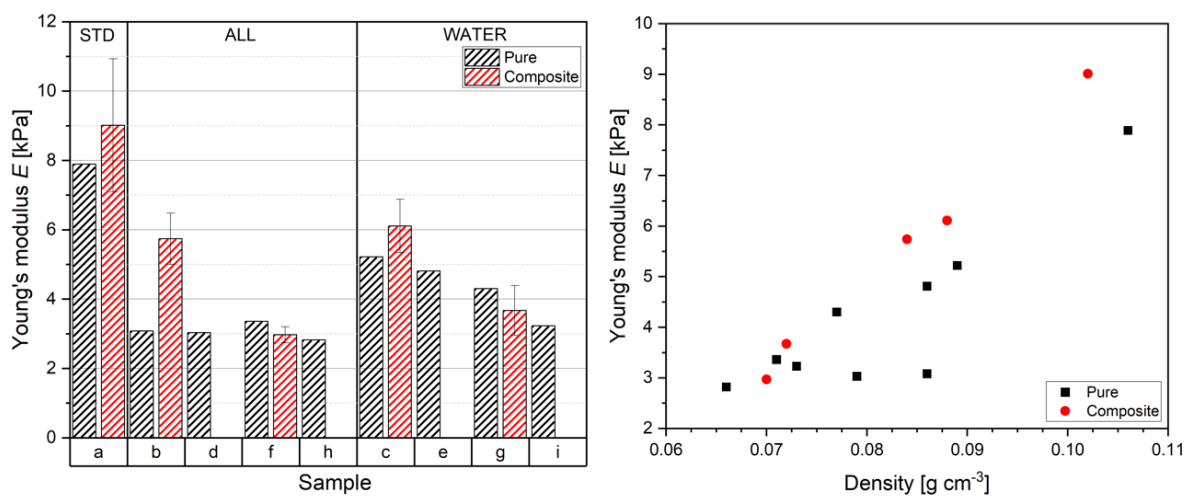


Figure 27: Comparison of Young's modulus  $E$  for pure and composite aerogels. Samples with lower densities showed lower Young's moduli in general.

The observed sound properties of pure and composite samples can be described as follows:

The sound absorption coefficient for pure and composite samples did not differ a lot for the measured range from 50 – 2000 Hz. Even though the mass of measured composite samples was higher, the absorption at frequencies > 400 Hz was just slightly higher.

The sound transmission loss was measured for all samples in the same range within the expected measurement precision. The first resonance frequency for pure samples could be observed at ~ 100 Hz for two samples and 300 – 400 Hz for four samples. The resonance frequency for composites was measured around 200 – 300 Hz.

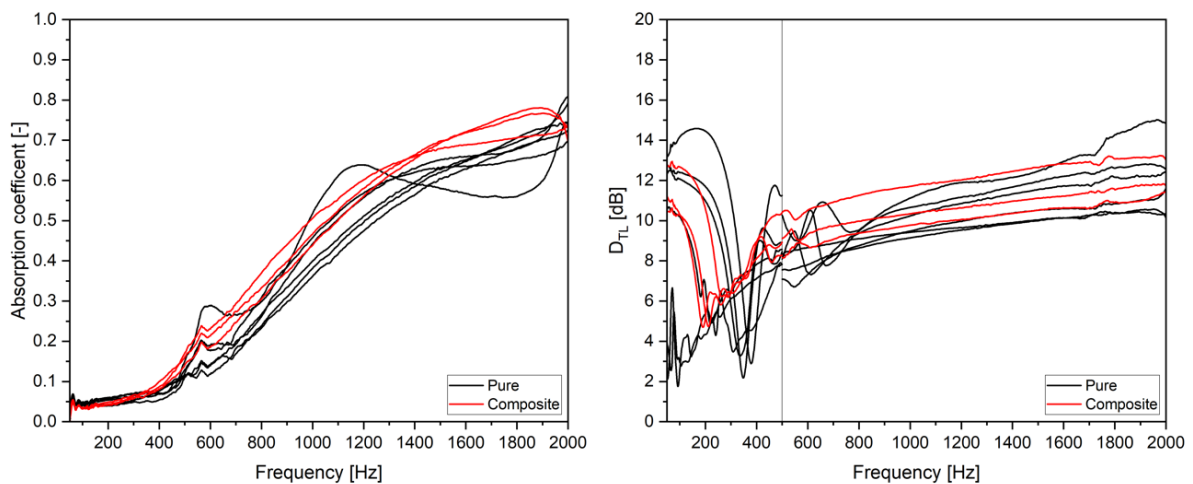


Figure 28: Comparison of sound absorption (left) and transmission loss (right) of pure and composite aerogels in the measured range from 50 – 2000 Hz. The sound absorption coefficient for pure and composite samples did not differ a lot for the measured range. The sound transmission loss was measured for all samples in the same range.

### 3.2 Vinyl Modification of Hybrid Aerogels

To study the influence of the introduction of VTMS to the given standard recipe, MTMS was gradually substituted against 5, 10, and 50% of VTMS, giving the opportunity to further functionalize the samples.

In preliminary experiments, it could be observed that the partial substitution of DMDMS against VMDMS would also lead to the successful introduction of vinyl groups inside the monolithic aerogels [155, 156]. Still, for economic reasons, it focused on VTMS in this work.

In the following paragraphs, first, the density and microstructure of VTMS-containing samples and their functionalization are analyzed. Then, surface chemistry and thermal- as well as mechanical properties are discussed. Finally, their reaction to fire is studied.

The samples in this chapter are named “**V**” followed by a number representing the VTMS content in percent. The index “\_Thiol” is added for samples after the first functionalization step, indicating the addition of a functional thiol group. The index “\_VPA” is added for samples after

the second functionalization step, indicating the addition of VPA. For example, **V05\_VPA** represents a sample where 5% of MTMS were substituted by VTMS and which was further functionalized with VPA.

### 3.2.1 Density and Microstructure

In Table 6 the mean values for  $\rho_{env}$ ,  $\rho_{skel}$ ,  $\Phi$  and  $S_R$ , of non-functionalized VTMS containing samples are shown, per variation at minimum 18 in cylindrical shapes. The errors were calculated as standard deviations from their mean values. The measured envelope density ( $0.108 - 0.111 \text{ g cm}^{-3}$ ) seemed to be unaffected by the concentration of VTMS within the studied range of 5 – 50% VTMS.

The same could be observed for skeletal density ( $1.31 - 1.33 \text{ g cm}^{-3}$ ). Since porosity is calculated out of both before-named values, it is quite constant for all samples. The shrinkage varies from 2.5 to 3.9%.

Table 6: Envelope and skeletal density of unfunctionalized VTMS containing samples with their respective calculated porosity and measured radial shrinkage. The error of all skeletal density measurements is  $\pm 0.01 \text{ g cm}^{-3}$ .

Sample	VTMS content [%]	Envelope density $\rho_{env}$ [ $\text{g cm}^{-3}$ ]	Skeletal density $\rho_{skel}$ [ $\text{g cm}^{-3}$ ]	Porosity $\Phi$ [%]	Radial shrinkage $S_r$ [%]
<b>V05</b>	5	$0.108 \pm 0.005$	1.31	91.8	$2.5 \pm 0.6$
<b>V10</b>	10	$0.110 \pm 0.003$	1.33	91.8	$3.9 \pm 0.9$
<b>V50</b>	50	$0.111 \pm 0.003$	1.31	91.5	$3.9 \pm 0.7$

In Table 7 the mean values for  $\rho_{env}$ ,  $\rho_{skel}$  and  $\Phi$  of VTMS containing samples after the first functionalization step with dithiol are shown, at minimum twelve samples for each composition in cylindrical shapes. The envelope density is increased for **V05\_Thiol** with  $0.110 \text{ g cm}^{-3}$  to **V50\_Thiol** with  $0.124 \text{ g cm}^{-3}$  with the concentration of VTMS within the studied range of 5 – 50% VTMS. As expected, the higher VTMS concentration afforded the dithiol greater opportunities to react and bind to the aerogel network. Furthermore, the total mass of the samples is increased to a greater extent with a higher VTMS concentration (**V05\_Thiol** with 2.6% and **V50\_Thiol** with 10.3% compared to the non-functionalized samples **V05** and **V50**, respectively). The skeletal density was measured in the same range of  $1.32 - 1.36 \text{ g cm}^{-3}$  for all samples and did not increase compared to non-functionalized samples. The calculated porosity decreased for higher thiol concentrations. No change in shrinkage compared to non-functionalized samples was observed, and therefore, the shrinkage was not recalculated.

Table 7: Envelope and skeletal density of VTMS containing samples after the first functionalization step with their respective calculated porosity. The error of all skeletal density measurements is  $\pm 0.01 \text{ g cm}^{-3}$ .

Sample	VTMS content [%]	Envelope density $\rho_{env}$ [ $\text{g cm}^{-3}$ ]	Total mass increase [%]	Skeletal density $\rho_{skel}$ [ $\text{g cm}^{-3}$ ]	Porosity $\Phi$ [%]
V05_Thiol	5	$0.110 \pm 0.005$	$2.6 \pm 0.2$	1.36	91.9
V10_Thiol	10	$0.115 \pm 0.003$	$4.7 \pm 0.5$	1.33	91.3
V50_Thiol	50	$0.124 \pm 0.004$	$10.3 \pm 0.9$	1.32	90.6

In Table 8 the mean values for  $\rho_{env}$ ,  $\rho_{skel}$ ,  $\Phi$  and  $S_R$  of VTMS containing samples after the first functionalization step with dithiol are shown, at minimum six samples for each composition in cylindrical shapes. The envelope density strongly increased for V05\_VPA with  $0.156 \text{ g cm}^{-1}$  to V50\_VPA with  $0.167 \text{ g cm}^{-1}$  with the concentration of VTMS within the studied range of 5 – 50%. The total mass compared to unfunctionalized samples increased up to 19 – 28% after the second functionalization step with VPA. The skeletal density was for all samples in the same range of  $1.43 - 1.48 \text{ g cm}^{-1}$  and increased compared to unfunctionalized and thiol-functionalized samples. The calculated porosity, therefore, decreased for higher VPA concentrations to  $\sim 89\%$ . Bigger changes in shrinkage compared to unfunctionalized samples were observed and therefore recalculated:  $S_R$  was observed between 4.3 and 6.8% after the final functionalization step.

Table 8: Envelope and skeletal density of VTMS-containing samples after the second functionalization step with their respective calculated porosity and measured radial shrinkage. The error of all skeletal density measurements is  $\pm 0.01 \text{ g cm}^{-3}$ .

Sample	VTMS content [%]	Envelope density $\rho_{env}$ [ $\text{g cm}^{-3}$ ]	Total mass increase [%]	Skeletal density $\rho_{skel}$ [ $\text{g cm}^{-3}$ ]	Porosity $\Phi$ [%]	Radial shrinkage $S_R$ [%]
V05_VPA	5	$0.156 \pm 0.006$	$19 \pm 6$	1.43	89.1	$6.7 \pm 0.5$
V10_VPA	10	$0.167 \pm 0.008$	$23 \pm 5$	1.48	88.7	$6.8 \pm 0.3$
V50_VPA	50	$0.167 \pm 0.005$	$28 \pm 2$	1.45	88.5	$4.3 \pm 1.1$

In Figure 29 SEM images of V50, V50\_Thiol, and V50\_VPA are exemplarily shown to check the microstructure for structural changes in the aerogels network during the functionalization steps. For all samples, no change in the network structure could be observed. The particle size, as well as the connectivity, was unaffected by functionalization itself. The same applied within V05- and V10-series.

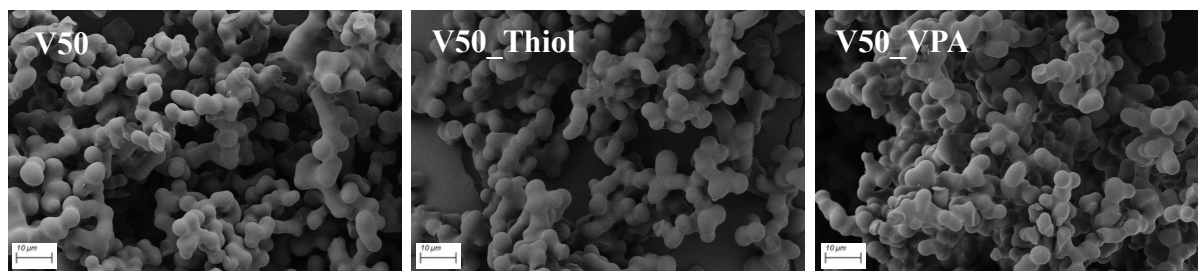


Figure 29: SEM images of **V50**, **V50\_Thiol**, and **V50\_VPA**. The microstructure did not change with functionalization. Images of the **V05**- and **V10**-series can be found in the Appendix (Figure A 8 and Figure A 9).

It could be observed that the particle size within the network is influenced by the amount of VTMS precursor: a higher concentration of VTMS leads to smaller particles. **V05** shows particles in the range of  $7.5 \mu\text{m}$ , while **V50** shows particles in the range of  $4.5 \mu\text{m}$ . This can be explained by a slightly higher reactivity of VTMS at the present pH conditions compared to MTMS, leading to higher reaction rates and, therefore, to a higher number of smaller particles aggregated to the aerogels network [65, 157].

### 3.2.2 Surface Chemistry

The surface chemistry of the samples was analyzed with energy-dispersive X-ray spectroscopy (EDX) to determine the presence of sulfur (which indicates the presence of dithiol) and phosphorus (which indicates the content of VPA). The results are presented in Table 9. For sample **V50**, where no presence of sulfur or phosphorus was expected, just a slight signal of sulfur was measured, leading to a calculated mass percentage of 0.22 wt.-%. This signal can be a result of impurities during synthesis or sample preparation for SEM/EDX measurement. For **V50\_Thiol**, sulfur was expected and measured, leading to a calculated mass percentage of 4.33%. No phosphorus was detected after the first functionalization step with the dithiol group. For **V50\_VPA**, sulfur as well as phosphorus was detected with 3.59 wt.-% and 11.07 wt.-%, respectively, after the functionalization with VPA. The presence of nitrogen (2.06 wt.-%) in sample **V50\_VPA** indicated that after washing, the samples still contained some residuals of nitrogen-containing initiator (AIBN). For sample **V50\_Thiol**, no AIBN leftovers could be detected *via* EDX.



Table 9: Elemental analysis from energy-dispersive X-ray spectroscopy (EDX) measurements of samples **V50**, **V50\_Thiol**, and **V50\_VPA**.

Element	Mass per element [wt.-%]		
	V50	V50_Thiol	V50_VPA
<b>C</b>	56.53	57.65	38.26
<b>N</b>	0.00	0.00	2.06
<b>O</b>	18.70	17.55	27.44
<b>Si</b>	24.55	20.47	17.58
<b>P</b>	0.00	0.00	11.07
<b>S</b>	0.22	4.33	3.59
<b>Sum</b>	100.00	100.00	100.00

Since the EDX measurements were performed in mapping mode and carbon pads were used for sample fixation, the content of carbon should not be considered. Therefore, adjusted values without the element carbon were calculated and compared to theoretical values (calculated at an estimated reaction rate of 100%) in the following Table 10. It can be seen that for **V50**, the theoretical values fit very well with the experimentally obtained data. For **V50\_Thiol**, 24.84 wt.-% were calculated while 10.22 wt.-% were obtained experimentally for the element Sulphur. The difference of -14.62 wt.-% can be explained due to the estimated reaction rate of 100% used for calculation. Considering that the aerogels network consists of spherical primary particles, it is not very likely that 100% of vinyl groups are available at the surface of the primary particles for the reaction with the thiol group. Therefore, the calculated values are much higher than the experimentally observed data. For **V50\_VPA**, 9.19 wt.-% were calculated while 17.93 wt.-% were obtained experimentally for the element Phosphorus. This can be explained by the likely possibility of self-polymerization of VPA resulting in higher phosphorus content than calculated theoretically, as the theoretical value counts for one VPA molecule per thiol group.

Table 10: Adjusted values from elemental analysis via EDX (Exp.) and calculated theoretical composition (Theor.) of the samples **V50**, **V50\_Thiol**, and **V50\_VPA** at estimated reaction rates of 100%. The difference (Diff.) of experimental to theoretical value was calculated.

Element	Adjusted mass per element [wt.-%]								
	V50			V50_Thiol			V50_VPA		
	Exp.	Theor.	Diff.	Exp.	Theor.	Diff.	Exp.	Theor.	Diff.
<b>C</b>	-	-	-	-	-	-	-	-	-
<b>N</b>	0.00	0.00	0.00	0.00	0.00	0.00	3.34	0.00	3.34
<b>O</b>	43.02	42.53	0.49	41.44	39.30	2.14	44.44	44.32	0.13
<b>Si</b>	56.48	57.47	-0.99	48.34	35.86	12.47	28.47	27.47	1.01
<b>P</b>	0.00	0.00	0.00	0.00	0.00	0.00	17.93	9.19	8.74
<b>S</b>	0.51	0.00	0.51	10.22	24.84	-14.62	5.81	19.02	-13.21
<b>Sum</b>	100.00	100.00	-	100.00	100.00	-	100.00	100.00	-

For further understanding and proof of reaction, the samples with the highest vinyl concentration (**V50**, **V50\_Thiol**, and **V50\_VPA**) were analyzed *via*  $^{13}\text{C}$  solid-state nuclear magnetic resonance spectroscopy (NMR). The obtained spectra were plotted and compared with each other (cf. Figure 30, left).

The expected structures are shown next to the spectra (Figure 30, right). The shown structures are connected within the aerogels network *via* oxygen between the silicon center atoms (Si-O-Si).

The chemical shifts at 1 ppm and -2 ppm in all spectra could be attributed to methyl groups (-CH<sub>3</sub>) from all three used precursors forming the network, namely VTMS, MTMS, and DMDMS. The shift at -2 ppm belongs to organotrialkoxysilanes VTMS and MTMS, according to the literature, and the shift at 1 ppm to DMDMS. [158] The chemical shifts at 135 ppm and 132 ppm in all spectra belonged to the vinyl groups of VTMS bond into the aerogels network [159]. It could be seen that the intensity of those peaks and, therefore, the concentration decreased after the first reaction step, which indicated a successful reaction of those groups as expected. The fact that there are still peaks at these shifts led to the assumption that not all vinyl groups reacted during synthesis. This could be explained by the microstructure of the aerogel samples: since not all vinyl groups were present at the network surface, they could not react completely. For **V50\_Thiol**, new shifts occurred at 16 ppm, 27 ppm, 32 ppm, and 71 ppm. These could be attributed as follows: The peak at 16 ppm resulted from the elimination of the vinyl bond to Si-CH<sub>2</sub>-R, the peaks at 27 ppm and 32 ppm resulted from S-CH<sub>2</sub>-R, and the peak at 71 ppm could be identified as O-CH<sub>2</sub>-R. [160, 161]

For **V50\_VPA**, a new shift at 24 ppm occurred, and the intensities of shifts at 27 ppm and 32 ppm increased. The peak at 24 ppm could be identified as P-CH<sub>2</sub>-R. The intensities of peaks at 27 ppm and 32 ppm increased due to the formation of further S-CH<sub>2</sub>-R groups during the addition reaction of VPA. [160, 161]

The available NMR spectra strongly indicated a successful chemical reaction and binding of the individual components during the two-step functionalization process.

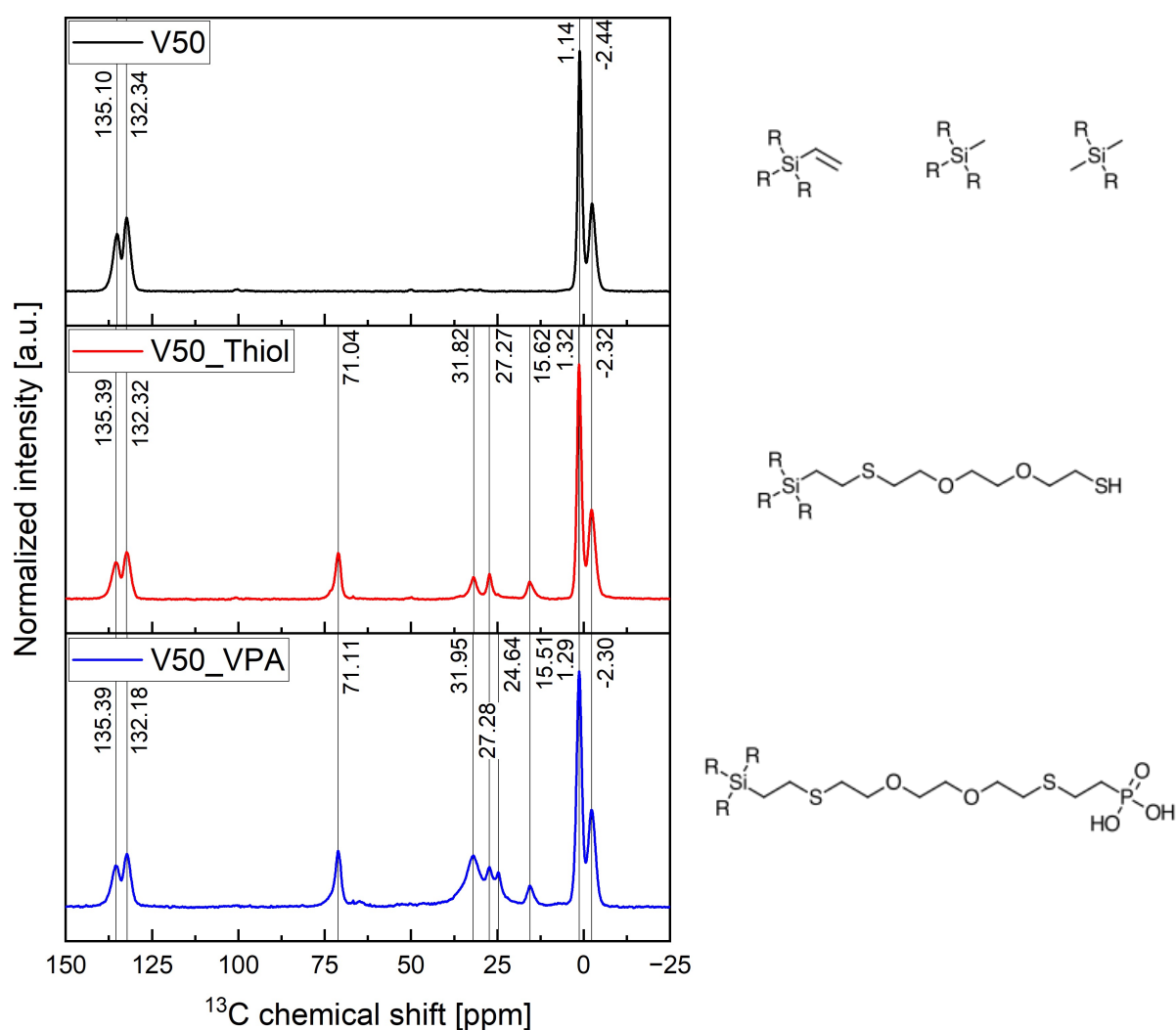


Figure 30: <sup>13</sup>C-NMR spectra of samples **V50**, **V50\_Thiol**, and **V50\_VPA** (left) and expected chemical structures within the aerogel network (right).

To check whether the functionalization influenced the hydrophobicity, water drop contact angles were measured. The results of **V05**-, **V10**- and **V50**-series are presented in Table 11. All samples showed hydrophobic properties except for **V50\_VPA**. Here, the contact angle could not be measured because the sample was hydrophilic and directly soaked up the droplet (cf. Figure 31). This indicated that there seemed to be an upper limit for the loading of samples with VPA for getting hydrophobic samples. VPA itself is hydrophilic because of its present OH

groups. Low amounts of VPA showed no real influence on the hydrophobicity of the sample, but at some point, there was a breakdown leading to hydrophilic monoliths.

Table 11: Water drop contact angle determined by drop shape analyzer for sample-series V05, V10, and V50.

Sample	Water drop contact angle		
		$\theta_c$ [°]	
	_	_Thiol	_VPA
V05	142	129	135
V10	130	132	130
V50	136	134	-

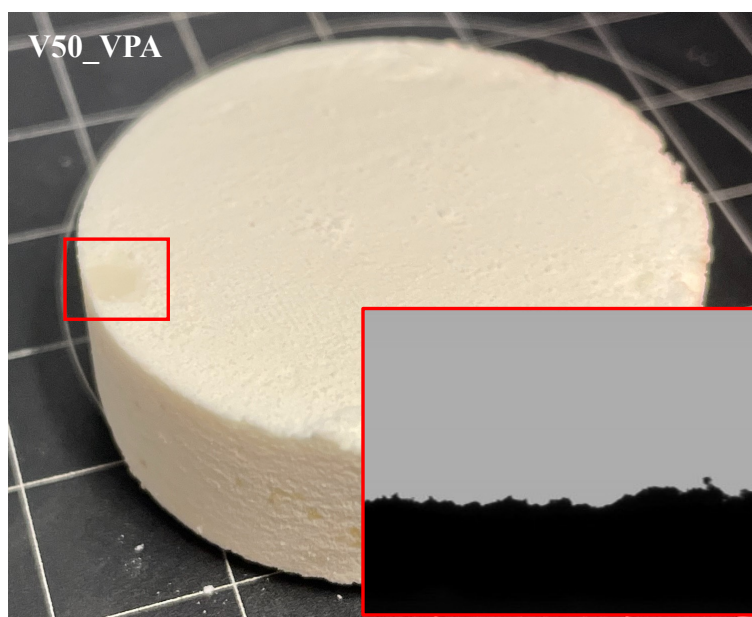


Figure 31: Digital image of sample V50\_VPA after water drop contact angle measurement. The sample showed hydrophilic properties, so that no contact angle could be measured.

### 3.2.3 Thermal Properties

HotDisk measurements were performed to study the trends in thermal conductivity of functionalized and unfunctionalized samples at room temperature (cf. Table 12). It could be observed that functionalized samples after thiol treatment show slightly higher thermal conductivity values ( $\sim 34 \text{ mW m}^{-1} \text{ K}^{-1}$ ) than untreated samples ( $\sim 31 \text{ mW m}^{-1} \text{ K}^{-1}$ ). For VPA-treated samples, the thermal conductivity rises to  $\sim 47 \text{ mW m}^{-1} \text{ K}^{-1}$ . This trend followed the increase in density, which was already described in chapter 3.2.1 “Density and Microstructure”.

The values obtained *via* the HotDisk method should not be taken as exact (absolute) values, but trends and tendencies can be seen very well. There exist several papers about poor comparability of thermal conductivities measured with steady-state (HFM) and/or transient (HotDisk) methods; one was recently published by Malfait *et al.* They noted that under unfavorable

conditions and in the context of aerogel research, transient methods are more likely to provide unreliable data. [162]

Table 12: Thermal conductivity of sample series V05, V10, and V50 at 20°C measured with HotDisk method.

Sample	Thermal conductivity at 20°C		
	$\lambda$ [mW m <sup>-1</sup> K <sup>-1</sup> ]		
	–	_Thiol	_VPA
V05	31.4	33.7	41.7
V10	31.4	34.1	44.4
V50	30.6	34.4	46.5

### 3.2.4 Mechanical Properties

To determine the mechanical properties of the synthesized aerogels and the functionalized samples, they were compressed uniaxially up to 60% strain. After compression, the unfunctionalized and dithiol-functionalized samples were unloaded. They immediately recovered to their original height without any visible damage. For VPA-functionalized samples, V05\_VPA was compressed up to ~35% strain, but the sample already broke. Therefore, no further compression tests were performed with VPA-containing samples since they lost their flexibility. The measured stress-strain-curves are shown in Figure 32 and in the range of  $0 < \varepsilon < 10\%$  the Young's modulus was calculated. The results are listed in Table 13.

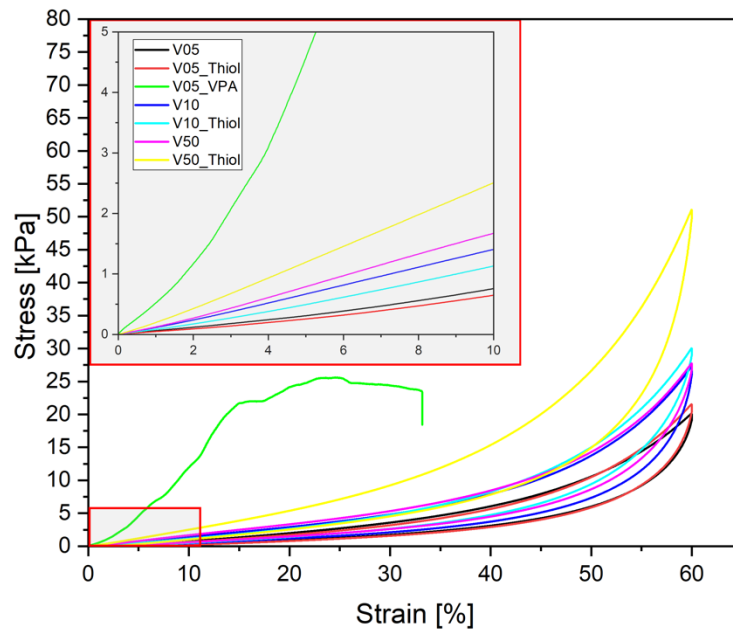


Figure 32: Uniaxial stress-strain-curve of sample-series V05, V10, and V50. More detailed single stress-strain curves are shown in the appendix (cf. Figure A 10).

The Young's modulus increased with increasing amount of VTMS. The increased stiffness could already be felt by hand. The calculated Young's modulus for **V10** and **V50** is with 15.0 kPa and 16.1 kPa, respectively, more than double the value of **V05** with 7.0 kPa.

For thiol functionalized samples **V05\_Thiol** and **V10\_Thiol**, no changes in Young's modulus within their errors could be observed compared to **V05** and **V10**, respectively. The Young's modulus of sample **V50\_Thiol** increased to 26.4 kPa.

Sample **V05\_VPA** broke during the measurement, and it was therefore stopped after 35% strain. The calculated Young's modulus is expected to be  $\sim 120$  kPa, which is around a power of ten higher than all other samples measured. The samples functionalized with VPA fully lost their flexibility due to the polymerization of VPA. Polymerized VPA is not flexible (like many polymers) and, therefore, stiffens the inherently flexible aerogel.

Table 13: Young's modulus  $E$  calculated in the linear range of stress-strain curves from 0 to 10% strain for sample-series **V05**, **V10**, and **V50**.

Sample	Young's modulus $E$ [kPa]		
	–	_Thiol	_VPA
<b>V05</b>	$7.0 \pm 0.4$	$6.4 \pm 0.8$	$\sim 120$
<b>V10</b>	$15.0 \pm 2.2$	$13.7 \pm 0.8$	-
<b>V50</b>	$16.1 \pm 1.0$	$26.4 \pm 2.2$	-

### 3.2.5 Reaction to Fire

To check the samples' reaction to fire, a flame from a Bunsen burner was used to light up the samples. The flame was set for 20 s directly onto the surface of the monolithic samples, and the temperatures at the surface and inside the monolith were measured.

The measured temperature profile of each sample can be found in Figure 33. It can be seen that samples **V0** (without any vinyl groups, corresponds to sample **a** from section 3.1.1), **V50**, and **V50\_Thiol** reached very high temperatures of 800 – 1000°C at the inside of the monolith, while all samples had similar temperatures at the outside during ignition ( $\sim 800^\circ\text{C}$ ). After ignition, the sample temperature at the outside decreased first, then slightly increased again before reaching a temperature plateau. The temperatures of vinyl-containing samples (**V50** and **V50\_Thiol**) were higher than the temperatures of the vinyl-free sample (**V0**). This can be explained due to the higher reactivity of vinyl groups resulting in higher temperatures during the combustion process. On the inside, the temperature increased and reached its maximum after approx. 180 – 210 s. The samples totally burned through, as the images in Figure 35 show. It took about

500 seconds until the temperatures at the in- and outside reached temperatures below 30°C again.

The flame-retardant treated samples **V05\_VPA**, **V10\_VPA**, and **V50\_VPA** all showed similar temperature profiles. First, during ignition, the temperatures at the outside increased up to 800°C. Then, the temperatures directly decreased as soon as the flame was stopped. The measured outside temperature went down to 30°C after 200 – 250 s. The samples did not start to burn, as can be seen in Figure 35. A black protection layer is formed at the flame side of the samples. For the inside of the material, the temperature increased up to 50 – 100°C after 50 s before decreasing to 30°C after 300 – 350 s.

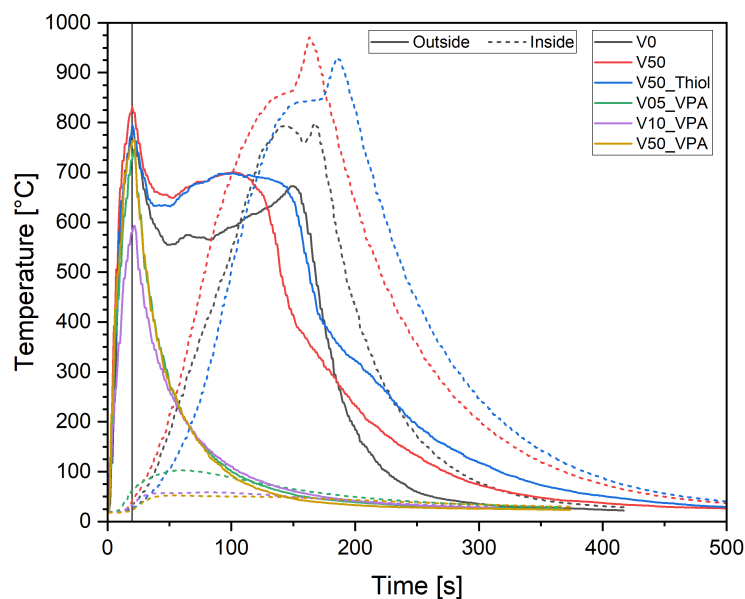


Figure 33: Temperature profile during flame treatment. The outer temperature is measured at the side of the flame and the inner temperature within the monolith. The data was collected in an interval of 1 s. All samples reached high temperatures at the outside (> 600°C), at the inside only non-VPA-functionalized samples burned and therefore reached high temperatures there.

In the following Figure 35, the burning behavior can be seen. Samples without flame retardant started burning, and the whole sample was burned after ignition. While sample **V0** started burning with a visible flame after ignition, the vinyl-containing samples **V50** and **V50\_Thiol** did not show this visible flame. White smoke could be observed for all untreated samples during combustion.

The treated samples **V05\_VPA**, **V10\_VPA**, and **V50\_VPA** all showed good fire retarding properties: After ignition, a black protective layer directly formed at the surface in contact with the flame. After the flame stopped, glowing and burning directly stopped. The sample did not burn through and no visible smoke could be observed.



Figure 34: Photographic image of sample V0 before fire testing.

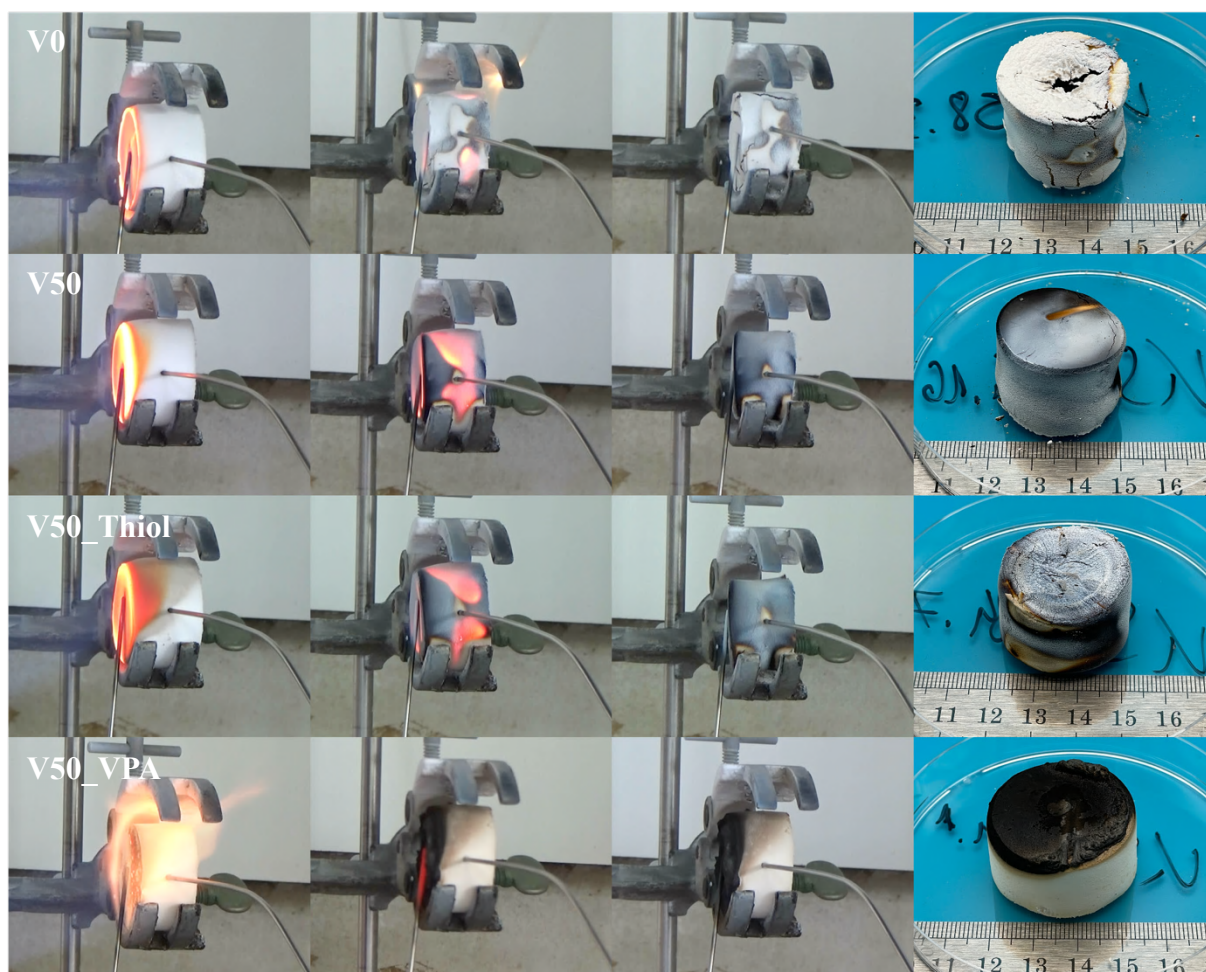


Figure 35: Photographic images of samples V0, V50, V50\_Thiol, and V50\_VPA during and after fire testing. From left to right column: ignition, burning, right after burning (2x).

The following Figure 36 shows the samples inside after combustion. As can be seen, sample V50 totally burned through and the inner of the sample is black. For functionalized samples (here V50\_VPA as an example), it can be seen that the inside of the sample is intact and just the surface directly in contact with the fire from the Bunsen burner was burned. After a small penetration depth of approx. less than 5 mm, the material showed no visible change to the back-side or unburned samples. To check whether the inside of the material is still fireproofed, the



sample was cut in half and the cut surface was ignited. No change in combustion behavior could be observed (cf. Figure A 11), leading to the result that the flame-retardant effect is also effective at the materials inside.

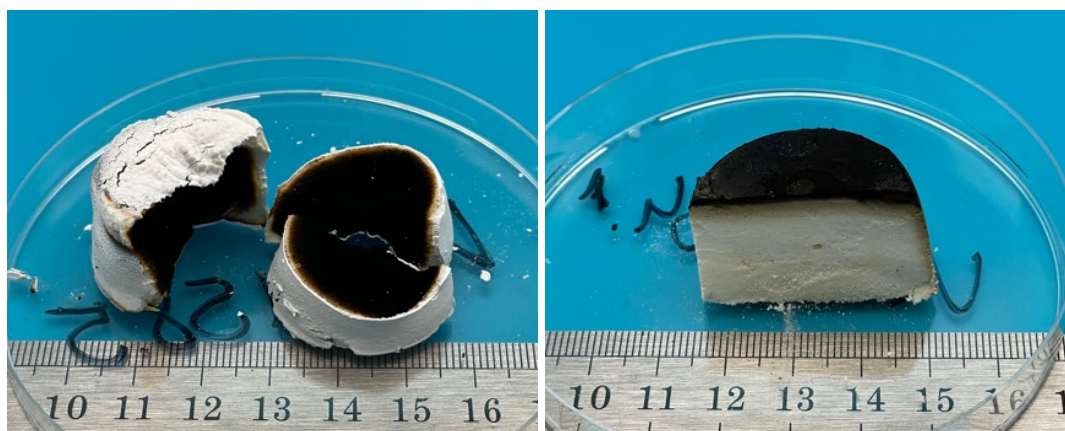


Figure 36: Photographic images of samples **V50** (left) and **V50\_VPA** (right) after fire treatment showing the inside of the samples. While the non-functionalized sample **V50** was totally black on the inside, the functionalized sample **V50\_VPA** just showed a black surface and the inside was unaffected.

### 3.2.6 Thermal Decomposition

The materials' thermal behavior was measured under inert conditions in Simultaneous Thermal Analysis (STA) and Thermogravimetric Analysis (TGA) for temperatures up to 800°C. In the following Figure 37 the mass losses and heat flux measured with STA are shown for samples **V50**, **V50\_Thiol**, and **V50\_VPA**.

The samples **V50** and **V50\_Thiol** were quite stable up to temperatures of ~ 325°C. At higher temperatures, the decomposition of organic groups inside the aerogel network started. In the first step, **V50** lost approx. 4% of its weight up to 500°C. At higher temperatures, the mass decreased further to approx. 88% of initial mass at 800°C. Sample **V50\_Thiol** showed a quite similar trend as sample **V50** but with much higher mass losses at each step. In the first step up to 500°C, the material lost up to approx. 15% of its initial weight. In the second step, **V50\_Thiol** ended up with approx. 74% of its initial weight.

The measured curve for **V50\_VPA** resulted from a combination of **V50\_Thiol** and pure poly(VPA), which can be found in the literature [163]. A first degradation step starting at approx. 150°C can be seen in the curve from sample **V50\_VPA** up to approx. 325°C (mass loss: 6%), where it is combined with the starting decomposition step from **V50\_Thiol** up to 475°C (mass loss: 13%), where a mass loss of poly(VPA) contributed to steep mass loss of 18% in total at 500°C. Sample **V50\_VPA** ended up with 72% of its initial mass at 800°C. An IR spectrometer was coupled to the STA device to identify the combustion products. However, due to the high number of signals, the analysis was unable to identify individual products (see Figure A 12 in the appendix).

The measured dynamic scanning calorimetry (DSC)-curves of **V50**, **V50\_Thiol**, and **V50\_VPA** from Figure 37 differed from each other. While **V50** showed first endothermic behavior during heat-up to 325°C, exothermic behavior in the range from 325°C – 550°C and endothermic behavior up to 800°C, **V50\_Thiol** showed endothermic behavior in the full temperature range from 30 °C – 800°C. **V50\_VPA** showed higher endothermic behavior up to 475°C, followed by a steep drop to exothermic conditions and the following exothermic behavior. This can be explained by the different degradation reactions inside the aerogel materials due to the different chemical compositions (without thiol, with thiol, with thiol, and VPA).

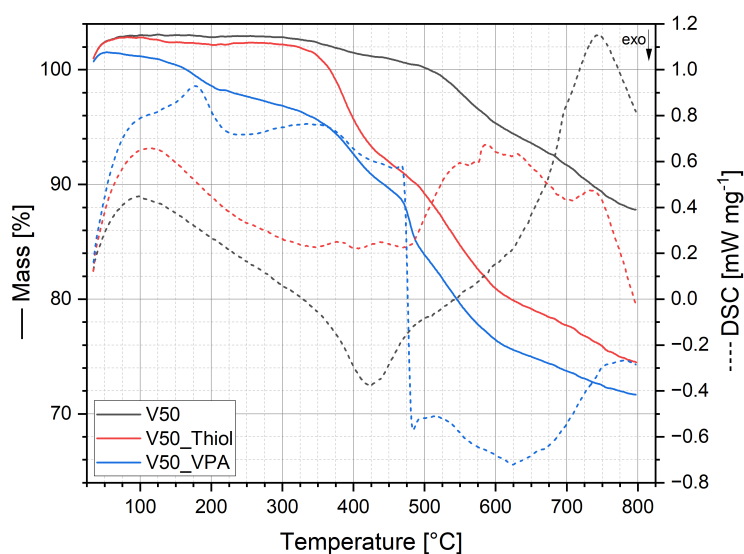


Figure 37: TGA- and DSC-curves of STA measurement for samples **V50**, **V50\_Thiol**, and **V50\_VPA** measured in inert gas conditions (argon). Residual masses of 88%, 74%, and 72% of its initial mass were obtained, respectively.

In the following Figure 38, the mass losses measured with TGA are shown for samples **V05\_VPA**, **V10\_VPA**, and **V50\_VPA** to study the influence of different amounts of VPA. While the general degradation steps of all measured samples showed comparable trends, their residual masses followed the trend that higher vinyl content and, therefore, higher VPA content resulted in higher residual masses at 800°C. While **V05\_VPA** had the lowest residual mass at 62.7%, **VPA10\_VPA** had 65.9%, and **VPA50\_VPA** had about 67.7%. The small mass at the initial stage, less than 100°C, can be explained by the evaporation of water, which seemed to be present in samples after longer storage of samples before measurement. After this, the same steps for all samples could be observed as measured with the STA device in Figure 37 and already discussed before.

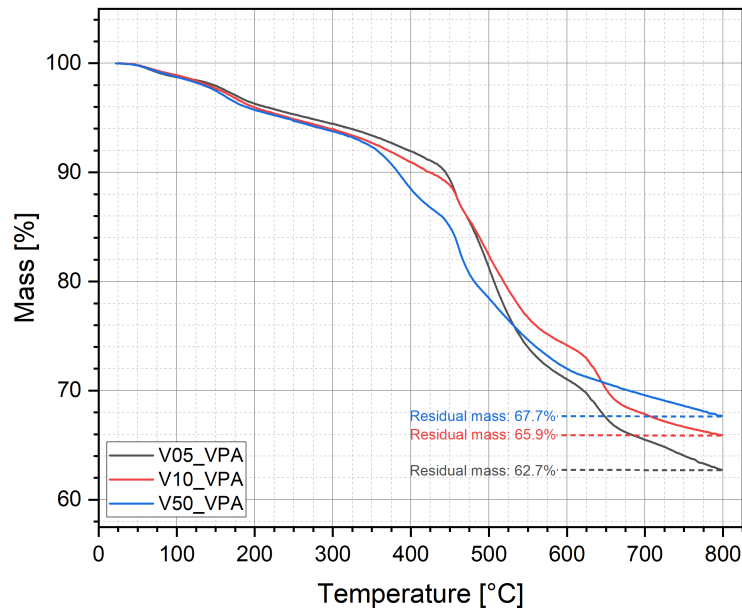


Figure 38: TGA-curves of samples **V05\_VPA**, **V10\_VPA**, and **V50\_VPA** measured in inert gas conditions (nitrogen). The obtained curves followed the trend that higher vinyl content and, therefore, higher VPA content resulted in higher residual masses.

### 3.2.7 Comparison of Non-functionalized and Functionalized Aerogels

In the following section, non-functionalized samples from section 3.1.1 “Pure Aerogels” were compared with functionalized samples containing flame retardant VPA according to their densities and microstructure, surface chemistry, thermal and mechanical properties, as well as their reaction to fire.

The observed densities and the microstructure differed a lot for functionalized samples (**V05\_VPA**, **V10\_VPA**, and **V50\_VPA**) compared to non-functionalized samples **a** from section 3.1.1 “Pure Aerogels”. While sample **a** had a density of  $0.106 \text{ g cm}^{-3}$ , samples **V05\_VPA**, **V10\_VPA**, and **V50\_VPA** had densities of  $0.156 - 0.167 \text{ g cm}^{-3}$ , which is an increase of about 55%. The microstructure differed because of the addition of VTMS precursor to the system. The more VTMS was added, the smaller the particles of the aerogels network got. For non-functionalized samples, particles with diameters of  $8.2 \mu\text{m}$  were observed. With increasing VTMS concentration, the particles reached diameters as low as  $4.5 \mu\text{m}$ . The functionalization process itself did not influence the resulting particles.

The surface chemistry and, therefore, hydrophobicity of samples slightly changed. For non-functionalized samples, water drop contact angles of  $136^\circ$  could be observed. With increasing VTMS concentration and functionalization, the contact angle stayed first constant (**V05\_VPA** and **V10\_VPA**) before it decreased up to a not measurable hydrophilic absorption of water during contact angle measurements for sample **V50\_VPA**.

Even though the here obtained values for thermal properties could not be compared absolutely since they were measured with different measurement techniques (steady-state (HFM) and transient (HotDisk) method), non-functionalized samples showed lower thermal conductivities than functionalized ones.

The mechanical properties of the obtained samples are different: non-functionalized samples showed flexible and very soft behavior, during the functionalization process, the samples totally lost their flexibility, got brittle, and therefore were not completely investigated. Young's moduli of  $\sim 8$  kPa and  $\sim 120$  kPa were calculated respectively.

The samples' reactions to fire differed. While non-functionalized samples totally burned through, functionalized samples did not burn and formed a black protection layer at their surface.

Taking all the obtained data into account, it seemed like the lowest content of VTMS was sufficient for reaching a lightweight but inflammable material that still showed hydrophobic properties. Further reduction of VTMS and less functionalization with dithiol and VPA could potentially overcome the effect of increased thermal conductivity and loss of flexibility.

### 3.3 Synthesis of Particles

A new recipe for synthesizing particles *via* emulsion technique was invented to decrease the material's bulk density further. To study the influence of the introduction of VTMS as a third precursor, the amount of vinyl-containing precursor was gradually increased to 50% and 100%, allowing to further functionalize the samples.

In the following paragraphs, first, the results of density and microstructure characterization of particle samples are described. Second, the size of particles was determined, and last, thermal conductivity measurements were conducted and compared with standard mat-shaped samples. The samples in this chapter are named respecting their vinyl content: **V0** describes a sample with no VTMS, **V50** with 50% VTMS, and **V100** is 100% VTMS. The index “\_dil” was used for samples with higher water content, respectively diluted samples. For example, **V50\_dil** represents a sample with 50% VTMS and higher water content during synthesis.

#### 3.3.1 Density and Microstructure

The following Table 14 shows the mean values for  $\rho_{bulk}$ ,  $\rho_{skel}$ , and the yield of samples **V0**, **V50**, and **V100**, as well as their respective dilutions. Per variation, at least 12 batches were produced. The errors were calculated as standard deviations from their mean values.

The bulk density seemed to be unaffected by the concentration of VTMS within the range of 0 – 50% VTMS. For higher VTMS concentration (100%), the bulk density strongly increases. The diluted samples do not show significantly lower densities compared to their undiluted samples. For **V0**, **V0\_dil**, **V50**, and **V50\_dil**, the bulk densities were measured in a range of  $\sim 0.05 \text{ g cm}^{-3}$ . For **V100** and **V100\_dil**, the bulk density increased to  $\sim 0.08 \text{ g cm}^{-3}$ . The skeletal density of all samples could be observed in the range of  $1.36 - 1.54 \text{ g cm}^{-3}$ .

For 0% and 50% VTMS, the received yield is almost stable at 26 – 29 mL total volume per batch. For 100% VTMS, the yield decreased to 13 mL. The sol reacted faster with increasing VTMS concentration, as known from the literature: it is shorter for the higher electron-donating group of organo-alkoxysilanes [65, 164]. The diluted samples show lower yields compared to their undiluted version: for **V0\_dil** and **V50\_dil** approx. 20 mL of particles were received per batch. Since **V100** already obtained low yields, the diluted version had almost the same yields. Compared to Yun *et al.*, who synthesized pure MTMS particles ( $\rho_{bulk} = 0.08 \text{ g cm}^{-3}$ ) in a comparable W/O-emulsion process, the here achieved bulk densities are about 40% lighter ( $\rho_{bulk} \sim 0.05 \text{ g cm}^{-3}$ ) [89].

Table 14: Bulk and skeletal density of samples with their yield. The error of all skeletal density measurements is  $\pm 0.02 \text{ g cm}^{-3}$ .

Sample	H <sub>2</sub> O:MTMS -ratio	VTMS content [%]	Bulk density $\rho_{bulk}$ [g cm <sup>-3</sup> ]	Skeletal density $\rho_{skel}$ [g cm <sup>-3</sup> ]	Yield [mL]
<b>V0</b>	39.65	0	$0.053 \pm 0.006$	1.42	$29 \pm 3$
<b>V0_dil</b>	50.00	0	$0.048 \pm 0.011$	1.54	$20 \pm 3$
<b>V50</b>	39.65	50	$0.055 \pm 0.005$	1.41	$26 \pm 3$
<b>V50_dil</b>	50.00	50	$0.051 \pm 0.004$	1.41	$20 \pm 2$
<b>V100</b>	39.65	100	$0.086 \pm 0.010$	1.36	$13 \pm 3$
<b>V100_dil</b>	50.00	100	$0.073 \pm 0.012$	1.41	$13 \pm 2$

Scanning electron images of the synthesized particles are shown in Figure 39. The microstructure follows the same trends explained in sections 3.1.1.1 and 3.2.1: The particle size decreased with increasing dilution as well as increasing VTMS concentration. Therefore, sample **V0** showed the biggest particles within the aerogel network, and sample **V100\_dil** was the smallest. Since the particles were not aged, their interparticular necks were not as distinctive as for the monolithic samples, which have had up to several days to age.

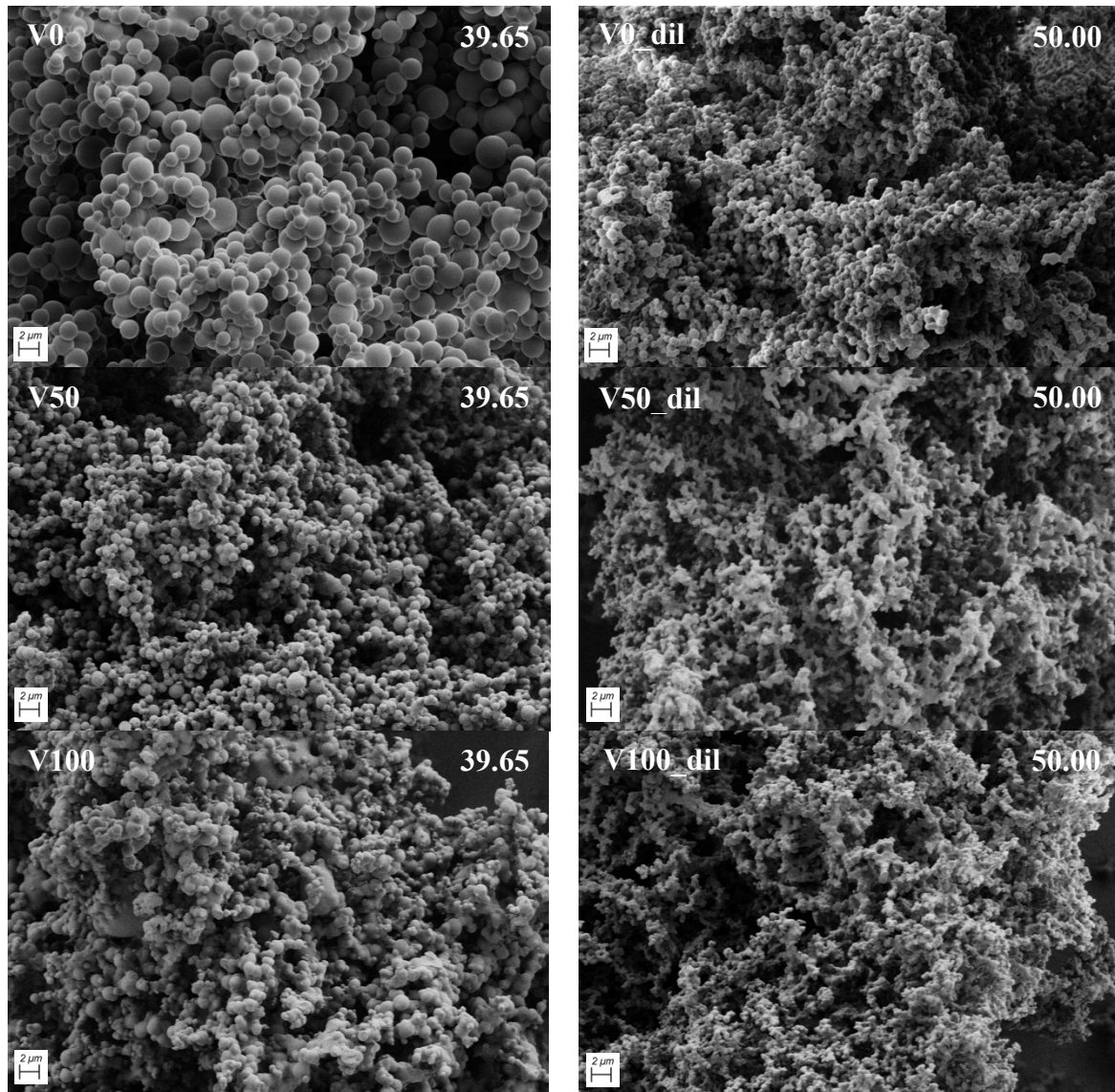


Figure 39: SEM images of samples **V0**, **V0\_dil**, **V50**, **V50\_dil**, **V100** and **V100\_dil**. The microstructure is strongly influenced by the VTMS concentration as well as the dilution. The higher the VTMS concentration and the level of dilution, the smaller the particles. Since samples had no time for aging, the interparticle necks are not as pronounced as for monolithic samples with longer aging.

### 3.3.2 Particle Size Distribution

The particle size distributions are shown in Figure 40. Samples **V0** and **V0\_dil** show the smallest particles. With increasing VTMS concentration, the particles got bigger as the condensation reaction was observed to be much faster. **V0** and **V0\_dil** showed  $D_{50}$  values of 183  $\mu\text{m}$  and 279  $\mu\text{m}$ , respectively (cf. Table 15).  $D_{50}$  values for **V50** and **V50\_dil** were 418  $\mu\text{m}$  and 629  $\mu\text{m}$ , for samples with the highest VTMS concentration, **V100** and **V100\_dil**  $D_{50}$  values of 445  $\mu\text{m}$  and 444  $\mu\text{m}$  were measured. The values for **V100** and **V100\_dil** were lower than expected. A reason for this is the limitation of the measurement device: Particles larger than 2000  $\mu\text{m}$  cannot be measured and therefore cut off from the calculations. It is expected that both samples showed

a higher amount of these big particles. This can also be estimated from the following digital microscope images shown in Figure 41.

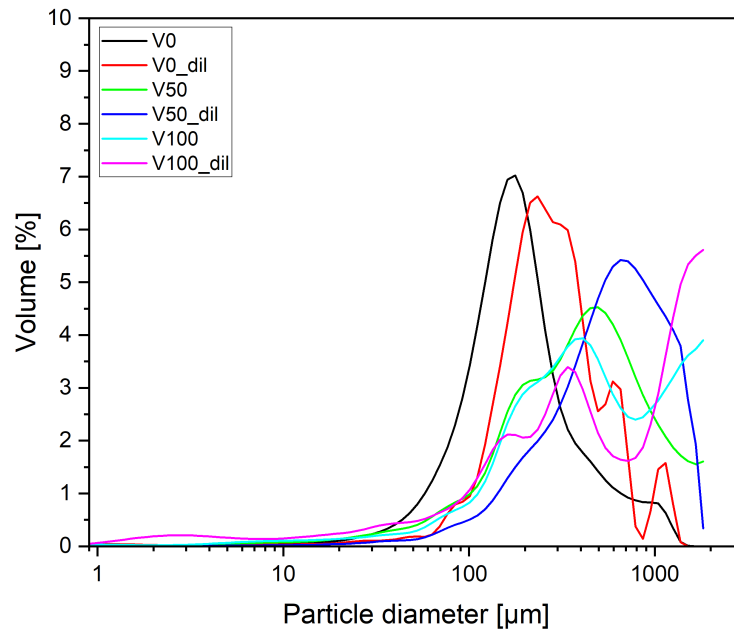


Figure 40: Particle size distribution particles synthesized with different VTMS and water concentrations. With increasing VTMS concentration, the particles got bigger, as well as with increasing dilution. Samples **V100** and **V100\_dil** exceeded the device's measurement range of up to 2000  $\mu\text{m}$ .

Table 15: Particle size distribution and its  $D$ -values calculated from Figure 40.

Sample	H <sub>2</sub> O:MTMS -ratio	VTMS content [%]	D <sub>10</sub> [ $\mu\text{m}$ ]	D <sub>25</sub> [ $\mu\text{m}$ ]	D <sub>50</sub> [ $\mu\text{m}$ ]	D <sub>75</sub> [ $\mu\text{m}$ ]	D <sub>90</sub> [ $\mu\text{m}$ ]
<b>V0</b>	39.65	0	81.4	125.8	182.9	273.2	498.2
<b>V0_dil</b>	50.00	0	133.9	192.9	278.6	414.5	648.4
<b>V50</b>	39.65	50	111.4	214.2	417.6	715.8	1166
<b>V50_dil</b>	50.00	50	195.3	365.6	628.6	980.5	1343
<b>V100</b>	39.65	100	123.0	230.6	445.1	991.5	1563
<b>V100_dil</b>	50.00	100	61.5	187.8	444.3	1276	1693

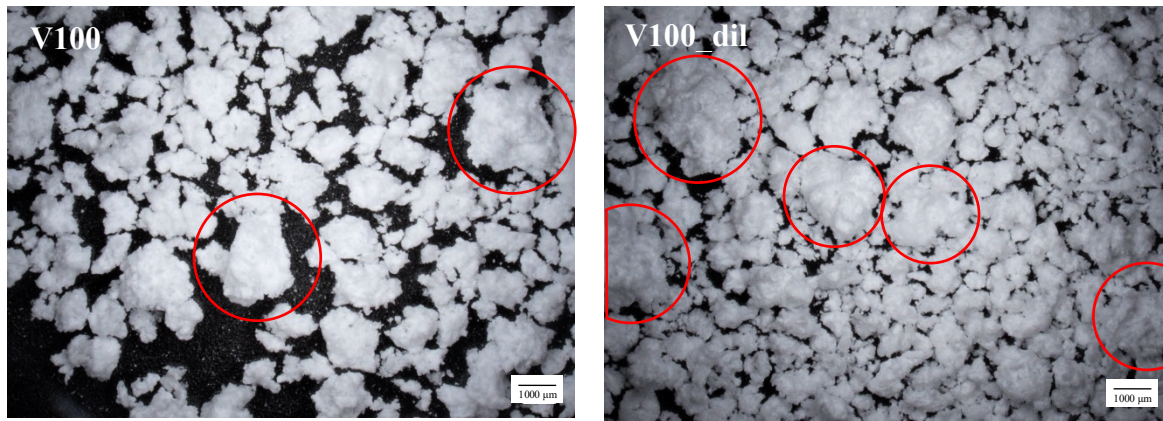


Figure 41: Digital microscope images of sample **V100** (left) and **V100\_dil** (right) at 20x magnification. The images demonstrate the bigger particles above 2000  $\mu\text{m}$ , which could not be measured with the particle size analyzer (marked red).

### 3.3.3 Thermal Properties

HFM studies were carried out for particle samples and compared to monolithic mat-shaped samples (cf. Figure 42). Samples **V0** and **V0\_dil** showed almost the same thermal conductivities in the measured range from 0 – 60°C. Compared to mat-shaped monoliths  $\sim 1 \text{ mW m}^{-1} \text{ K}^{-1}$  higher thermal conductivities were measured. This could be explained by possible air gaps and paths between the particles during measurement, which increased the thermal conductivities. The effect of air gaps and paths for powder and/or granulate silica aerogel samples was well investigated by Neugebauer *et al.* [165]. They found out that the compaction of powder beds typically leads to smaller thermal conductivities because of the reduced volume of interstitial air. The compaction is accompanied by an increased bulk density.

Samples **V50**, **V50\_dil**, **V100**, and **V100\_dil** were only measured at 25°C, as no change in the general trend of the curve was expected over the entire range of 0 – 60°C. As the density of **V50** and **V50\_dil** are comparable to **V0** and **V0\_dil**, no change in thermal conductivity at 25°C was measured, as expected.

For **V100** and **V100\_dil**, the thermal conductivity further increased at 25°C due to the higher density of those samples, resulting in better thermal conductivity through the solid backbone of aerogel particles. Since the density of **V100\_dil** is slightly smaller than the density of **V100**, the thermal conductivity of **V100\_dil** with  $\sim 35 \text{ mW m}^{-1} \text{ K}^{-1}$  is slightly smaller, too, compared to **V100** with  $\sim 36.5 \text{ mW m}^{-1} \text{ K}^{-1}$ .



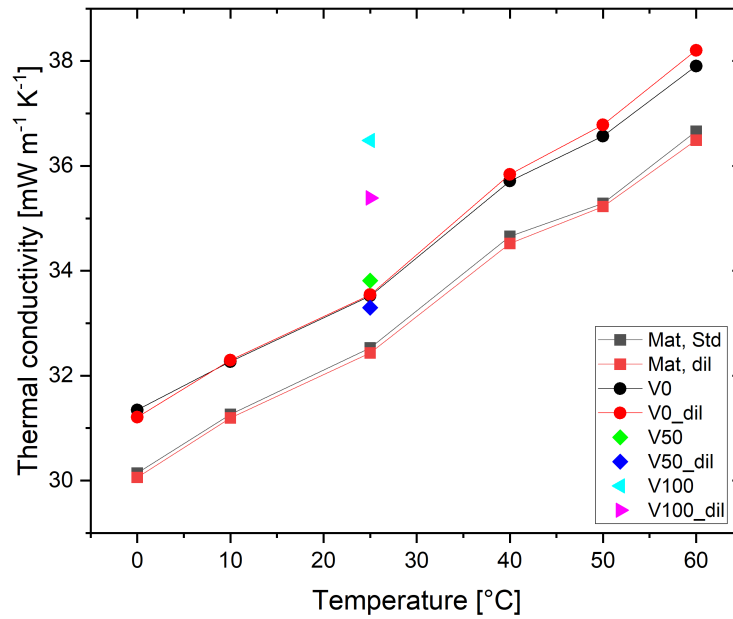


Figure 42: Thermal conductivity of particles compared to mat-shaped monoliths with different precursor-to-water ratios and different VTMS concentrations. Particles, in general, showed higher thermal conductivities than monoliths.

### 3.3.4 Conclusion

A new recipe for synthesizing MTMS-DMDMS-based aerogel particles *via* emulsion technique was invented, and a third precursor (VTMS) was successfully incorporated up to 50%, giving the potential for further functionalization of the samples. The two-step functionalization process from section 3.2 could potentially be applied without any modifications to the investigated process.

For **V0**, **V0\_dil**, **V50**, and **V50\_dil**, the bulk densities were measured in the range of  $\sim 0.05 \text{ g cm}^{-3}$ . Higher VTMS concentrations led to higher bulk densities. The skeletal density of all samples could be observed in the range of  $1.36 - 1.54 \text{ g cm}^{-3}$ . For 0% and 50% VTMS, the highest yields could be observed, for 100% VTMS, the yield decreased. Compared to pure MTMS particles from the literature [89], the here achieved bulk densities are about 40% lighter. SEM images led to the result that the primary particle size decreased with increasing dilution as well as increasing VTMS concentration. The particle size distribution was measured: Samples **V0** and **V0\_dil** showed the smallest particles. The higher the VTMS concentration, the bigger the particles. **V100** and **V100\_dil** showed particles bigger than  $2000 \mu\text{m}$ , which could not be detected with the measurement device. At  $25^\circ\text{C}$ , samples **V0**, **V0\_dil**, **V50** and **V50\_dil** showed slightly higher ( $\sim 1 \text{ mW m}^{-1} \text{ K}^{-1}$ ) thermal conductivities as their respective monoliths. For **V100** and **V100\_dil**, the thermal conductivity further increased due to their higher density.

### 3.4 Silica Aerogel-Aerogel Composites

Aerogel-aerogel composites were synthesized to study the influence of the incorporation of ground silica aerogel granulates into an MTMS-DMDMS co-precursor aerogel. The idea was to reduce the material's thermal conductivity by incorporating a hydrophobic aerogel material (commercially available as Cabot ENOVA<sup>®</sup> IC3110) with ultralow thermal conductivities as filler within the “marshmallow-like” hybrid aerogel, resulting in an aerogel-aerogel composite. The general feasibility of this is examined in an initial study below. This chapter should be understood as the first trial and gives a possible outlook for further research in this direction.

Therefore, in the following paragraphs, the density of the first aerogel-aerogel composite samples is analyzed. Then, thermal- as well as mechanical properties are discussed. Further challenges, as well as ideas for optimization, are presented at the end.

The samples in this chapter are named “AAC\_” followed by a number representing the amount of granulate emulsion added during synthesis in grams. For example, AAC\_0 represents the reference sample without granulate, and AAC\_2.5 is a sample where 2.5 g of granulate emulsion was added.

The synthesis is described in section 4.1.4. In contrast to the synthesis from section 4.1.1, for faster gelation (to prevent the precipitation of the granulate), the base catalyst was changed from urea to tetramethylammonium hydroxide (TMAOH), allowing a fast and controlled gelation due to direct increase of the pH after the addition. To get information on the exact amount of granulate added (without the water) to the sol, 10 g of the granulate-emulsion was taken and dried in an oven at 80°C until the water was evaporated. The mass of granulate was determined to be 10% of the granulate-emulsion mass. This needs to be considered for the following results.

#### 3.4.1 Density, Porosity, and Shrinkage

In Table 16, the mean values for  $\rho_{env}$ ,  $\rho_{skel}$ ,  $\Phi$ , and  $S_R$  of the synthesized aerogel-aerogel composite samples are shown, per variation five in cylindrical shapes. The errors were calculated as standard deviations from their mean values.

The envelope density of all samples was measured between 0.101 and 0.119 g cm<sup>-3</sup>. The reference sample AAC\_0 is in the lower range, while with an increasing amount of granulate, the envelope density tends to increase up to sample AAC\_15.0. The increase in mass can be explained due to the granulate density, which is slightly higher than the density of the surrounding matrix. The granulate density is given in the manufacturer's datasheet as 0.120 – 0.150 g cm<sup>-3</sup>

[166] , while the matrix density typically is  $0.100 - 0.110 \text{ g cm}^{-3}$ . Sample **AAC\_20.0** could not be measured due to their fragile nature caused by the increasing granulate amount resulting in uneven shapes (cf. Figure A 14 in the appendix). Therefore, the volume calculation was not possible with a simple caliper.

The skeletal density of samples **AAC\_0** and **AAC\_10.0** were measured. From those, the skeletal density for **AAC\_2.5**, **AAC\_5.0**, and **AAC\_15.0** were estimated in the same region (as the materials composition does not change a lot), and therefore, the average was taken ( $\rho_{skel} = 1.2316 \text{ g cm}^{-3}$ ) for further calculation of the porosity of the samples. The porosity was observed in the range from 90.4% to 91.8%. The observed shrinkage (1.4 – 2.6%) was typical for “marshmallow-like” gels, and within their errors did not vary from each other.

Table 16: Envelope and skeletal density of samples **AAC\_0** – **AAC\_20.0** with their respective calculated porosity and measured radial shrinkage. The error of the skeletal density measurements is  $\pm 0.01 \text{ g cm}^{-3}$ .

Sample	Granulate-Emulsion [g]	Envelope density $\rho_{env}$ [g cm <sup>-3</sup> ]	Skeletal density $\rho_{skel}$ [g cm <sup>-3</sup> ]	Porosity $\Phi$ [%]	Radial shrinkage $S_r$ [%]
<b>AAC_0</b>	0.0	$0.1049 \pm 0.0056$	1.2255	91.5	$1.7 \pm 0.7$
<b>AAC_2.5</b>	2.5	$0.1011 \pm 0.0031$	1.2316*	91.8	$2.6 \pm 1.1$
<b>AAC_5.0</b>	5.0	$0.1144 \pm 0.0039$	1.2316*	90.7	$1.6 \pm 0.6$
<b>AAC_10.0</b>	10.0	$0.1104 \pm 0.0045$	1.2377	91.0	$1.4 \pm 0.9$
<b>AAC_15.0</b>	15.0	$0.1186 \pm 0.0049$	1.2316*	90.4	$2.1 \pm 0.9$
<b>AAC_20.0</b>	20.0	-	1.2316*	-	-

\* estimated value: calculated as the average of **AAC\_0.0** and **AAC\_10.0**.

### 3.4.2 Thermal Properties

HotDisk measurements were performed to study the trends in thermal conductivity of aerogel-aerogel composite samples at room temperature (cf. Figure 43). With an increasing amount of granulate, the thermal conductivity increased from  $29.8 \text{ mW m}^{-1} \text{ K}^{-1}$  for reference **AAC\_0** up to  $35.8 \text{ mW m}^{-1} \text{ K}^{-1}$  for **AAC\_15.0**. This was not the expected influence of the addition of a superhydrophobic low-thermal conductive material inside the “marshmallow-like” gels. The issue is expected as follows: During drying, the water-soaked granulates collapsed and, therefore, lost their good thermal insulating properties. The dried composite monoliths contained voids filled with air, resulting in an increased thermal conductivity.

To prevent the granulates from collapsing, the drying method must be changed. APD is not sufficient anymore. Instead of APD, SCD should be used. As reported by Laskowski, SCD can prevent the soaked-up granulates from collapsing [85]. The matrix should not be negatively influenced by SCD.

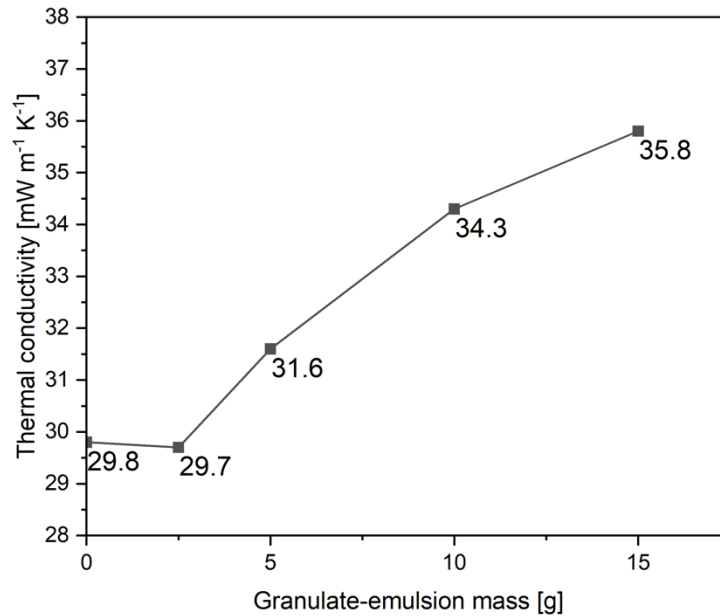


Figure 43: Thermal conductivity measured with HotDisk-method as a function of added granulate-emulsion mass. With increasing granulate content, the thermal conductivity increased.

### 3.4.3 Mechanical Properties

To determine the mechanical properties of the synthesized aerogel-aerogel composites, they were compressed uniaxially up to 60% strain. After compression, the samples were unloaded at the same rate. The reference sample AAC\_0 immediately recovered to its original height without any visible damage. Composite samples with granulate (AAC\_2.5 – AAC\_15.0) broke during the compression at certain points and did not recover to their original height after 60% strain. This can be observed in the measured stress-strain curves: The composite samples AAC\_2.5 – AAC\_15.0 all showed a stress of 0 kPa at 15 – 20% residual strain during decompression, while reference AAC\_0 went back to 0 kPa at 0% strain (cf. Figure 44). As the introduced filler granulates weakened the monolith structure due to their collapse, the samples easily broke with increased filler content.

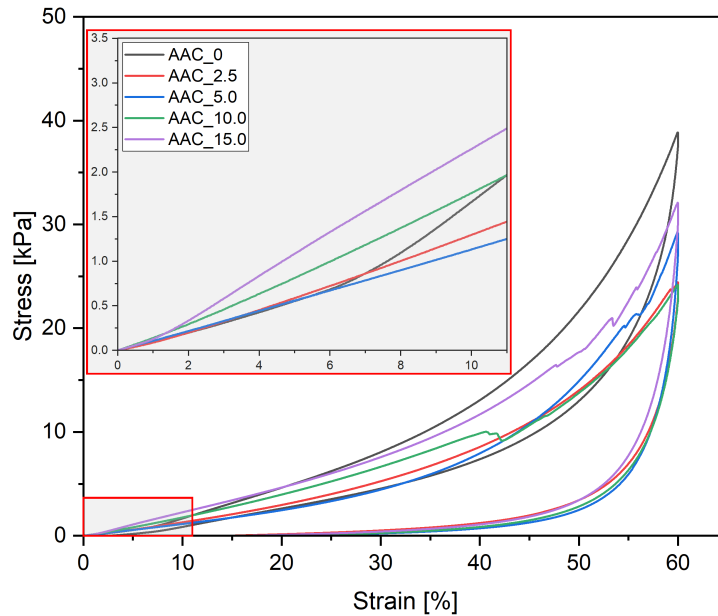


Figure 44: Stress-strain curve of samples AAC\_0 – AAC\_15.0. During compression, the composite samples broke. This can be observed in the poor shapes of the measured curves. During decompression, the samples reached 0 kPa stress at 15 – 20% residual strain, indicating that they did not recover to their original height. More detailed single stress-strain curves are shown in the appendix (cf. Figure A 15).

According to their increasing density, the calculated Young’s moduli showed an increasing trend, too (cf. Table 17). For reference sample AAC\_0, the Young’s modulus could not be determined in the range from 0 – 10% strain, as the measured stress-strain curve did not show a linear behavior. A reason for this could be the following: Due to the (by hand noticeably) higher stiffness of the sample, the applied preload of 0.150 N might not be enough to ensure the full contact of the upper pressure plate and the sample surface, leading to a change of the slope of the curves as soon as full contact was achieved. This results in a shift of the linear range, which here starts at a strain of about 7% (cf. Figure 44). Therefore, the Young’s modulus was calculated in the range of 7 – 17% (cf. Table 17), a detailed stress-strain curve is shown in the appendix (cf. Figure A 16).

Table 17: Young’s modulus  $E$  calculated in the linear range of stress-strain curves from 0 to 10% strain for samples AAC\_0 – AAC\_15.0.

Sample	Young’s modulus
	$E$ [kPa]
AAC_0	$33.5 \pm 3.6^*$
AAC_2.5	$12.9 \pm 2.7$
AAC_5.0	$10.9 \pm 0.4$
AAC_10.0	$19.1 \pm 1.8$
AAC_15.0	$20.1 \pm 4.9$

\* calculated between 7 and 17% strain.

The fact that the used filler granulates weaken the monolith structure due to their collapse can also be observed in the obtained Young’s moduli. While already very low amounts of filler

granulate lead to a strong decrease of the Young's modulus from about 33.5 kPa for reference AAC\_0 without filler to 12.9 kPa for AAC\_2.5 and 10.9 kPa for AAC\_5.0. For higher filler content, the Young's modulus increased up to 20.1 kPa for AAC\_15.0. The increasing stiffness is a consequence of the typical density dependence of the Young's modulus [167, 168]: As the number of granulates with higher density ( $\rho_{env} = 0.120 - 0.150 \text{ g cm}^{-3}$  [166]) compared to the matrix material with lower density ( $\rho_{env} = 0.100 - 0.110 \text{ g cm}^{-3}$ ) increased, this effect overcomes the weakening effect due to the collapsed granulates.

#### 3.4.4 Conclusion

The idea was to reduce the material's thermal conductivity by incorporating a hydrophobic aerogel material with ultralow thermal conductivities as filler within the "marshmallow-like" hybrid aerogel. The commercially available aerogel granulates could successfully be introduced into a flexible hybrid silica aerogel up to certain amounts. With an increasing amount of filler granulates, the density of the aerogel-aerogel composites increased up to  $\sim 0.119 \text{ g cm}^{-3}$ . Samples with more than 15 g of granulate emulsion got very unstable and hard to handle. Skeletal densities of about  $1.2316 \text{ g cm}^{-3}$  were measured, resulting in porosities of 90.4% to 91.8%. Radial shrinkages of the obtained samples were observed at about 1.4 – 2.6% for all samples. Other than expected, the thermal conductivity increased with an increasing number of granulates. This could be explained by the collapse of the filler granulates due to the APD process. The experiments should be repeated, and the samples should be dried in an SCD process. This would probably overcome the shrinkage of filler granulates and, therefore, could lead to the expected results of decreased thermal conductivity. During mechanical compression tests, the composite samples broke and did not fully recover to their original height. According to their increasing density, the calculated Young's moduli of composite samples showed an increasing trend at higher filler content. At lower content, the collapse of granulates weakened the structure compared to reference samples without filler, resulting in lower Young's moduli.

## 4 Experimental Part

The following “Experimental Part” is divided into the section “Materials and Methods”, which describes in detail how the samples were synthesized as well as which materials/chemicals were used, and the section “Characterization”, where all techniques for the final materials characterization/analysis with their specific parameters are explained.

### 4.1 Materials and Methods

In the following, the synthesis of monoliths and particles is described. First, the synthesis of MTMS-DMDMS-based monoliths as pure aerogels and composites with non-woven fabric are described. Second, the introduction of vinyl-containing precursors to the known system through increasing substitution is shown. The third section of this part describes the synthesis of particles instead of monoliths. Finally, the possibility of imprinting macroscopic cavities and shapes inside monolithic samples, followed by dissolution of those imprints, is explained.

#### 4.1.1 Synthesis of MTMS-DMDMS-based Monolithic Aerogels

In the following paragraphs, first, the synthesis of pure hybrid-silica aerogel samples is described. Finally, the synthesis of aerogel composites with non-woven fabric is shown. Both follow almost the same recipes and processes (cf. Figure 45). For optimization of the density of the final material, the precursor-to-water ratio is changed.

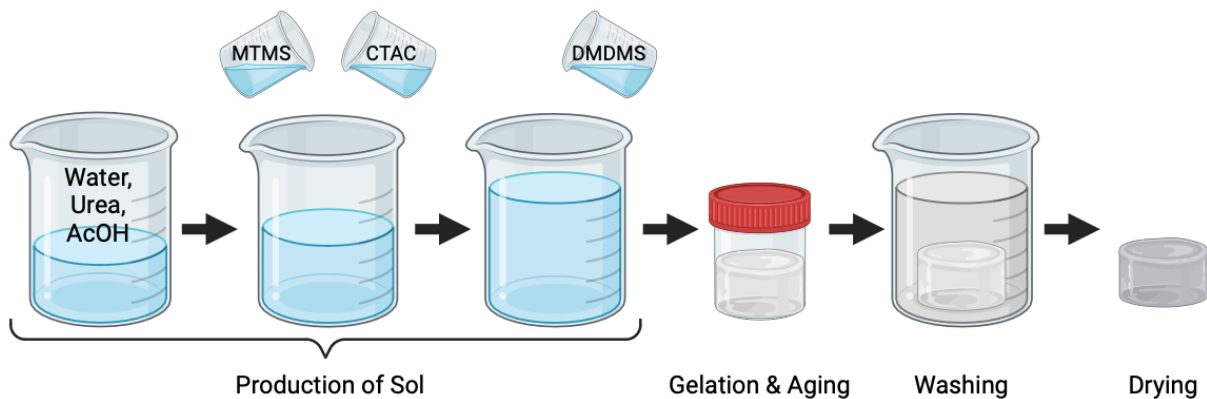


Figure 45: Schematic representation of the synthesis of pure aerogel samples. For composites, the prepared non-woven fabric is added to the screw container before addition of sol. Created with BioRender.com.

##### 4.1.1.1 Aerogels

For the synthesis of monolithic samples, methyltrimethoxysilane (MTMS) and dimethyl-dimethoxysilane (DMDMS), obtained from *abcr GmbH*, Germany, were used as precursors. Acetic acid (AcOH) was purchased from *Fisher Scientific GmbH*, Germany, and cetyltrimethylammonium chloride solution (CTAC, 25 wt.-% in H<sub>2</sub>O) from *Sigma-Aldrich GmbH*,

Germany. Urea was received from *Merck KGaA*, Germany. All chemicals were used as received. All sol-gel solutions were prepared from purified water. For the washing steps, ethanol (EtOH) from *Fisher Scientific GmbH*, Germany, and isopropanol (IPA) from *Sigma-Aldrich GmbH*, Germany, were used, both technical grades.

The synthesis consists of four main steps and the standard reference is mainly based on a recipe patented by Fener and Niemeyer [169]: hydrolysis, condensation, aging, and washing/drying, which were all done in a simple one-pot reaction. The weights of the chemicals can be seen in Table 18.

First, distilled water and urea were mixed and heated up to 50°C. For the hydrolysis, acetic acid was added, followed by MTMS and CTAC. The solution was mixed for 15 min at 50°C. Then DMDMS was added and mixed for another 45 min. Afterward, the sol was transferred to closed vessels and placed in an oven at 80°C for the listed time of gelation/condensation and aging (cf. Table 18). Before drying, the obtained wet gels were transferred into fresh solvents for washing to remove unreacted chemicals and the surfactant CTAC. Due to limited diffusion, washing was carried out for 24 h each following the order: water, ethanol, water, water, isopropanol. After that, the samples were finally dried out of isopropanol under ambient pressure at 80°C for 24 h in an oven.

Table 18: Synthesis recipes for 380 g (~ 350 mL) of total solution for reference sample (a) and modified samples (b – i). Samples b, d, f, and h represent the “dilution all”-series; samples c, e, g, and i represent the “water”-series.

Sample	H <sub>2</sub> O:MTMS -ratio	Aging [d]	H <sub>2</sub> O [g]	Urea [g]	AcOH [μL]	MTMS [g]	CTAC [g]	DMDMS [g]
a	39.65	1	177.99	74.39	71	42.50	59.91	25.13
b	50.00	1	204.82	64.51	62	36.86	51.95	21.79
c	50.00	1	184.80	77.24	74	34.99	62.20	20.69
d	55.00	3	215.38	60.62	58	34.63	48.82	20.48
e	55.00	3	187.30	78.28	75	32.24	63.04	19.06
f	60.00	7	224.74	57.18	55	32.67	46.04	19.32
g	60.00	7	189.43	79.17	76	29.89	63.75	17.67
h	65.00	7	233.09	54.10	52	30.91	43.57	18.28
i	65.00	7	191.27	79.94	77	27.86	64.37	16.47

The resulting samples were named and categorized as follows: Sample a represents the standard reference sample synthesized according to literature [169]. Samples b, d, f, and h represent the “all”-series with increasing water:MTMS-ratio, which means that all used chemicals (urea, AcOH, CTAC) except for the precursors were raised by the same level as the water. Samples c, e, g, and i represent the “water”-series with increasing water:MTMS-ratio, which means that



only the amount of water used during the synthesis was increased without changing the other ratios.

For the different characterization techniques, several sample geometries were synthesized.

#### 4.1.1.2 Aerogel Composites

Monolithic aerogel composites with non-woven fabric are synthesized analog to the synthesis of pure aerogels from section 4.1.1.1. The weights of the chemicals used for the production of sol are shown in Table 19. The non-woven fabric “Impexso Volumenvlies” was purchased in 10 mm and 20 mm thickness from *Impexso Vliesstoffe*, Germany.

For the preparation of aerogel composites, the non-woven fabric was cut in shape and cleaned with acetone to remove unwanted impurities from the production process. The masses of dried fabric were determined with an analytical balance before impregnating them with the sol.

Samples were synthesized in a cylindrical shape with 20 mm of non-woven fabric and around 25 ml of sol, resulting in monoliths with approx.  $\varnothing$  35 x 20 mm<sup>2</sup>. Matts were produced with 10 mm of non-woven fabric and around 1300 mL of sol, resulting in samples with dimensions of approx. 290 x 330 x 13 mm<sup>3</sup>.

Table 19: Synthesis recipes for 200 g (~ 180 mL) of total solution for reference sample (**a\_f**) and modified samples (**b\_f**, **c\_f**, **f\_f**, **g\_f**). Samples **b\_f** and **f\_f** represent the “all”-series; samples **c\_f** and **g\_f** represent the “water”-series.

Sample	H <sub>2</sub> O:MTMS -ratio	Aging [d]	H <sub>2</sub> O [g]	Urea [g]	AcOH [μL]	MTMS [g]	CTAC [g]	DMDMS [g]
<b>a_f</b>	39.65	1	93.68	39.15	38	22.37	31.53	13.23
<b>b_f</b>	50.00	1	97.26	40.65	39	18.42	32.74	10.89
<b>c_f</b>	50.00	1	107.80	33.95	33	19.40	27.34	11.47
<b>f_f</b>	60.00	7	99.70	41.67	40	15.73	33.56	9.30
<b>g_f</b>	60.00	7	118.28	30.09	29	17.19	24.23	10.17

The resulting samples were named and categorized as follows: Sample **a\_f** represents the standard reference sample synthesized according to the literature [169]. Samples **b\_f** to **g\_f** are synthesized with the same recipe analog to the previous section 4.1.1.1, with the only difference that the non-woven fabric was added to the sol before gelation: Sample **b\_f** and **f\_f** represent the “all”-series with increasing water:MTMS-ratio; Sample **c\_f** and **g\_f** represent the “water”-series with increasing water:MTMS-ratio.

### 4.1.2 Vinyl Modification of Monolithic Aerogels

For modification of monolithic aerogels with vinyl groups, new vinyl-containing precursors were successfully introduced (cf. Figure 46) to allow the aerogels to get further functionalized throughout these vinyl groups via a two-step thiol-ene click-reaction mechanism (cf. Figure 47).

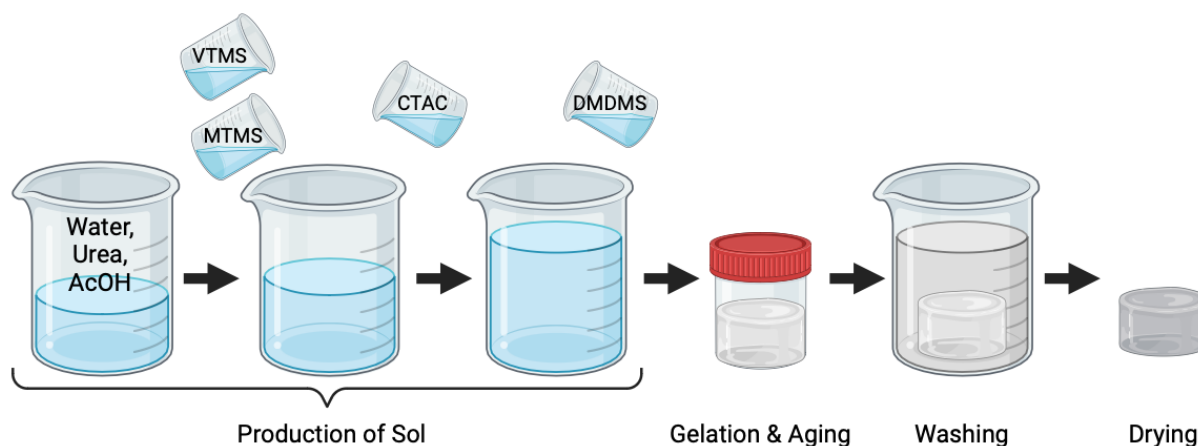


Figure 46: Schematic representation of the synthesis of vinyl-containing monolithic aerogel samples. Created with BioRender.com.

The introduction of vinyl groups into the aerogel network allows to further functionalize the samples with flame retardants as an example. Here in this case, a two-step thiol-ene click mechanism was used, consisting of the addition of thiol-groups to the aerogels network in the first step and then the addition of a flame retardant (*i.e.*, vinylphosphonic acid) in the second step (cf. Figure 47).

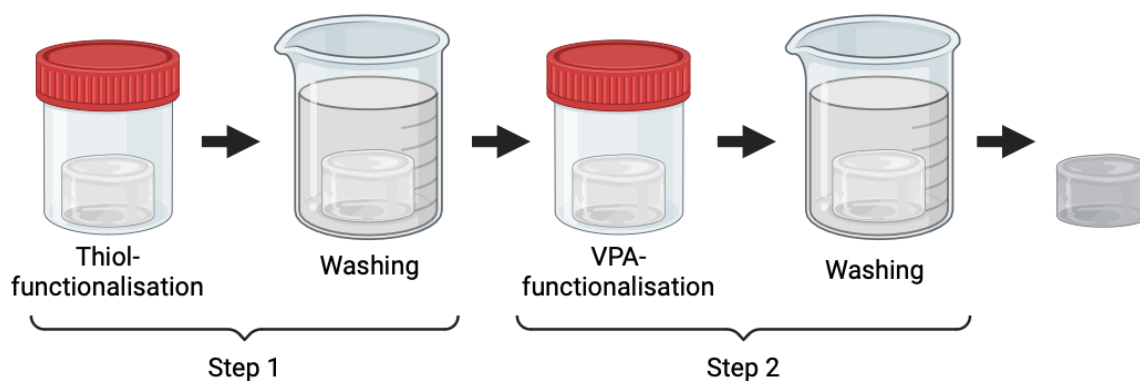


Figure 47: Schematic representation of the functionalization of vinyl-containing aerogel samples in a two-step process via thiol-ene click reaction mechanism. Created with BioRender.com.

#### 4.1.2.1 Synthesis of Vinyl Containing Monoliths

Besides the chemicals already listed in section 4.1.1.1, vinyltrimethoxysilane (VTMS) is obtained from *abcr GmbH*, Germany, for synthesis.

The monolithic samples are synthesized analog to the synthesis of pure aerogels. MTMS is partially substituted against VTMS (cf. Table 20) and added in the same step as MTMS. The samples are washed in the same way described in section 4.1.1.1 before drying at 60 – 80°C at ambient pressure for 24 h.

Samples for each series were synthesized in cylindrical shape with about 25 ml of sol, resulting in 18 monoliths with approx.  $\varnothing$  3 x 20 mm<sup>2</sup>.

Table 20: Synthesis recipes for 525 g (~ 500 mL) of total solution for vinyl-based monoliths with substitution of 5, 10, and 50 mol% of MTMS for VTMS. All samples were gelated and aged for one day.

Sample	VTMS:MTMS -ratio	H <sub>2</sub> O [g]	Urea [g]	AcOH [μL]	MTMS [g]	VTMS [g]	CTAC [g]	DMDMS [g]
V05	0.05:0.95	245.79	102.73	99	55.75	3.19	82.72	34.70
V10	0.10:0.90	245.67	102.68	99	52.79	6.38	82.68	34.69
V50	0.50:0.50	244.71	102.28	98	29.22	31.79	82.36	34.55

The samples were named V for “Vinyl” with numbers 05, 10, and 50, which represent the ratio of VTMS during the synthesis used for each sample.

#### 4.1.2.2 Functionalization via Thiol-Ene Click-Reaction

For the chemical functionalization of vinyl-containing aerogels, diethylene glycol diethyl ether (DEGDE) as solvent obtained from *Thermo Fisher Scientific Inc.*, Germany, is used. 2,2'-(ethylenedioxy)diethanethiol (EDET) and vinylphosphonic acid (VPA) from *Sigma-Aldrich GmbH*, Germany, were used as reagents. Azobis(isobutyronitrile) (AIBN), obtained from *Sigma-Aldrich GmbH*, Germany, is used as a radical initiator.

First, the dried vinyl-containing samples were treated in closed vessels with 50 mL DEGDE solution containing 10 wt.-% EDET and 0.5 wt.-% AIBN for 24 h at 70°C. In a second step, the samples were treated with 50 mL DEGDE solution containing 10 wt.-% VPA and 0.5 wt.-% of AIBN for another 24 h at 70°C. [69] After each step, five washings with IPA were performed at room temperature to get rid of unreacted chemicals, followed by a drying process at 60 – 80°C at ambient pressure to also characterize the samples in between each step.

After functionalization, IPA was used five times for washing the samples before drying at 60 – 80°C for 24 h at ambient pressure.

#### 4.1.3 Synthesis of Particles

Methyltrimethoxysilane (MTMS), dimethyldimethoxysilane (DMDMS), and vinyltrimethoxysilane (VTMS), obtained from *abcr GmbH*, Germany, were used as precursors. Acetic acid

(AcOH) was purchased from *Fisher Scientific GmbH*, Germany, and cetyltrimethylammonium chloride solution (CTAC, 25 wt.-% in H<sub>2</sub>O) from *Sigma-Aldrich GmbH*, Germany. Ammonia solution (NH<sub>4</sub>OH, 4.5 wt.-% in H<sub>2</sub>O) was ordered from *Fisher Scientific GmbH*, Germany. As the oil-phase during emulsion gelation, n-hexane from *Fisher Scientific GmbH*, Germany, was used. All chemicals were used as received. All sol-gel solutions were prepared from purified water. For the washing steps, ethanol (technical grade) from *Fisher Scientific GmbH*, Germany, was used.

According to Figure 48, a typical sol consisting of precursors MTMS and DMDMS as well as surfactant CTAC, water, and catalysts AcOH and NH<sub>4</sub>OH had to be mixed. Therefore, 14.86 mL of water, 5  $\mu$ L of AcOH, 0.35 mL of CTAC, and 3.01 mL of MTMS were mixed and stirred for 15 min at room temperature. Then, 1.93 mL of DMDMS was added and mixed for 45 min. Finally, 0.38 mL of NH<sub>4</sub>OH was added. At a stirring speed of 400 rpm, the sol as the aqueous phase was poured into the n-hexane as the oil phase at a volume ratio of 0.3 to form a water-in-oil emulsion. Subsequently, droplets of sol were formed. After 10 min of stirring, gelation of the dispersed phase took place. The spherical gel particles were filtered and washed several times with ethanol to remove surfactant and unreacted chemicals. After washing, the particles were dried at ambient pressure at 60 – 80°C in an oven.

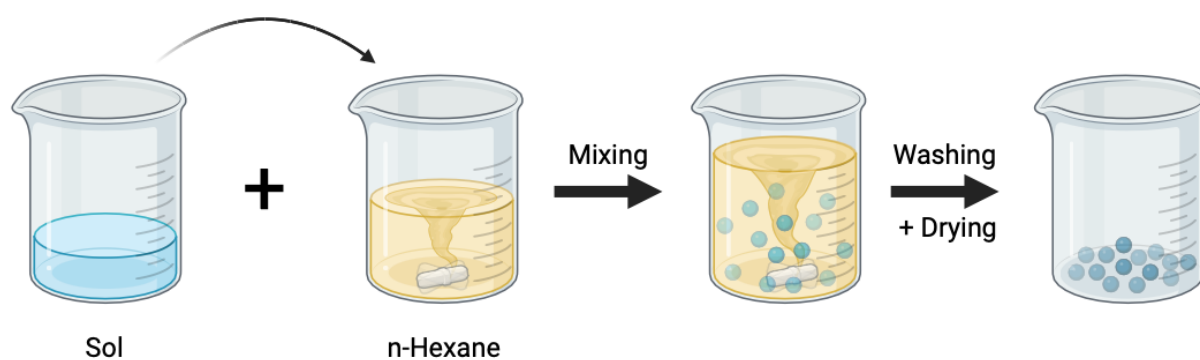


Figure 48: Scheme of emulsion-gelation process. The sol acts as water-phase (W) and the n-hexane as oil-phase (O) in a (W/O)-emulsion. Created with BioRender.com.

Several variations with changing precursor-to-water ratio and changing precursors (introducing vinyl-containing precursors for the ability of later functionalization) were performed. The respective amounts used for synthesis are shown in Table 21.

Table 21: Synthesis recipes for ~ 20 mL of total solution for reference sample and modified samples.

Sample	H <sub>2</sub> O:(MTMS+VTMS)-ratio	MTMS:VTMS-ratio	H <sub>2</sub> O [mL]	AcOH [ $\mu$ L]	MTMS [mL]	VTMS [mL]	CTAC [mL]	DMDMS [mL]	NH <sub>4</sub> OH [mL]
V0	39.65	1:0	14.98	5	2.91	0.00	0.42	1.96	0.38
V0_dil	50.00	1:0	15.82	4	2.54	0.00	0.35	1.63	0.38
V50	39.65	0.5:0.5	14.89	5	1.51	1.62	0.42	1.94	0.38
V50_dil	50.00	0.5:0.5	15.74	4	1.26	1.35	0.35	1.62	0.38
V100	39.65	0:1	14.79	5	0.00	3.22	0.42	1.93	0.38
V100_dil	50.00	0:1	15.66	4	0.00	2.69	0.35	1.61	0.38

#### 4.1.4 Silica Aerogel-Aerogel Composites

Silica aerogel-aerogel composites are, in general, synthesized analog to the synthesis of pure aerogels from section 4.1.1.1. The weights of the chemicals used to produce the sol are shown in Table 22. A TMAOH solution (25 wt.-% in H<sub>2</sub>O) from *Sigma-Aldrich GmbH*, Germany, was used. The aerogel granulates were ENOVA<sup>®</sup> IC3110 from *Cabot Corporation*, USA.

For the preparation of aerogel-aerogel composites, the granulates were emulsified in the first step: they were taken as received and wetted with a 50:50 wt.-% solution of water and ethanol. The solution was changed several times while the water content was gradually increased until all granulates were soaked up with pure water. Then, a T 50 digital ULTRA-TURRAX<sup>®</sup> from *IKA*, Germany, was used to grind the granulates in water at 5000 rpm for 5 min, followed by 10 min at 10000 rpm.

A typical sol consisted of the precursors MTMS and DMDMS as well as the surfactant CTAC, water, and the catalysts (AcOH and TMAOH) and were mixed with emulsified and ground ENOVA<sup>®</sup> IC3110 granulates. Therefore, the listed amount of granulate emulsion and water had to be mixed (cf. Table 22). Then, 21  $\mu$ L of AcOH, 12.64 g of MTMS, 17.82 g of CTAC, and 7.48 g of DMDMS were added, and the sol was properly stirred for 30 min at 50°C. After the addition of 533  $\mu$ L of TMAOH and further stirring for another 30 s, the granulate-sol mixture was quickly distributed into the closed gelation containers. The gelation and aging were carried out at 80°C for 72 h in an oven. Before drying, the obtained wet gels were transferred into fresh solvents for washing to remove unreacted chemicals and the surfactant CTAC. Due to limited diffusion, washing was carried out for 24 h each following the order: water, ethanol, water, water, isopropanol. After that, the samples were finally dried out of isopropanol under ambient pressure at 80°C for 24 h in an oven.

The samples were synthesized in a cylindrical shape, resulting in monoliths with approx.  $\emptyset$  35 x 20 mm<sup>2</sup>.

Table 22: Synthesis recipes for ~ 100 mL of total solution for reference sample (AAC\_0) and modified samples (AAC\_2.5, AAC\_5.0, AAC\_10.0, AAC\_15.0, AAC\_20.0). The sol was distributed into five closed containers for gelation.

Sample	Granulate-Emulsion [g]	H <sub>2</sub> O [g]	AcOH [ $\mu$ L]	MTMS [g]	CTAC [g]	DMDMS [g]	TMAOH [ $\mu$ L]
AAC_0	0.0	61.49					
AAC_2.5	2.5	59.24					
AAC_5.0	5.0	56.99	21	12.64	17.82	7.48	533
AAC_10.0	10.0	52.49					
AAC_15.0	15.0	47.99					
AAC_20.0	20.0	43.49					

## 4.2 Characterization

In the following, the techniques and their specific parameters used to characterize the final materials' properties are described.

### 4.2.1 Density, Porosity, and Shrinkage

The envelope density  $\rho_{env}$  of the cylindrical-shaped samples was measured by caliper and scale, calculating the volume and dividing it by the mass of the sample weight with an analytical balance. The bulk density  $\rho_{bulk}$  of the particle samples was measured by measuring the volume of the sample in the measurement cylinder and dividing it by the mass of the sample weight with an analytical balance. The skeletal density  $\rho_{skel}$  was measured with helium pycnometer AccuPyc® II 1340 from *Micromeritics*<sup>TM</sup>, Germany. Each measurement consists of ten purging cycles to remove air from the sample and sample chamber, followed by ten measurement cycles. Out of both densities, the porosity  $\Phi$  of the material was calculated by equation (10):

$$\Phi = 1 - \frac{\rho_{skel}}{\rho_{env}} \quad (10)$$

The radial shrinkage  $S_r$  was calculated by comparing the diameter of the container used for synthesis with the final aerogel's diameter.

### 4.2.2 Thermal Conductivity

The thermal conductivity was measured in the range of 0 – 60°C by the heat flow meter apparatus HFM 436 Lambda from *NETZSCH*, Germany. The samples had a minimum size of 200 x 200 mm<sup>2</sup> and a height of up to 13 mm.

For measuring the thermal conductivity of particles, a self-built measurement frame made of expanded polystyrene with inner dimensions of 120 x 120 x 20 mm<sup>3</sup> was filled with the sample (cf. Figure 49). The sample was filled slightly higher than the frame to ensure contact with the sample and measurement device.

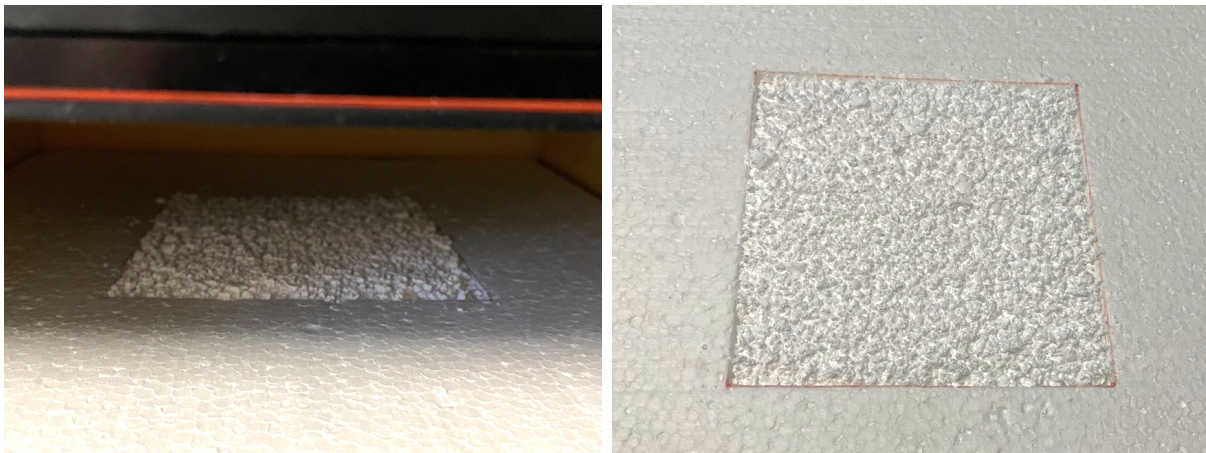


Figure 49: Photographs of HFM measurement frame for determination of thermal conductivity for particles made of expanded polystyrene. Left: frame with particles inside the HFM device; right: top-view of the particle-filled frame with inner dimensions of 120 x 120 x 20 mm<sup>3</sup>.

The thermal conductivity of smaller cylindrical samples with diameters of approx. 35 mm were measured with Hot Disk® TPS 2500 from *Hot Disk AB*, Sweden. A 5501 F2-Type Sensor with 6,403 mm and Grey Cable was used. The samples were measured at room temperature (~ 21°C). The measurement time was set to 40 s, and the heating power to 5 mW.

### 4.2.3 Acoustic Properties

To analyze the materials' sound absorption coefficient  $\alpha$  and the sound transmission loss ( $D_{TL}$ ) a 100 mm AcoustiTube® from *Gesellschaft für Akustikforschung Dresden mbH*, Germany was used. The absorption coefficient was measured in a 3-microphone setup, resulting in one measurement for the frequency range 50 – 2000 Hz. For the sound transmission loss, a 4-microphone setup was used, resulting in one measurement for the frequency range from 50 – 500 Hz (low frequency) and one measurement for 500 – 2000 Hz (high frequency), which were combined in postprocessing to one plot.

### 4.2.4 Morphology and Energy-dispersive X-ray Spectroscopy

To analyze the sample's microstructure, images were taken with the scanning electron microscope (SEM) Merlin from *Carl Zeiss*, Germany, at an acceleration voltage of 2 – 3 kV and a working distance of 7 – 10 mm. Before observation, the samples were sputtered with platinum for 100 s. The particle sizes were determined from these SEM images with the help of the software ImageJ.

For energy-dispersive X-ray spectroscopy (EDX), an Ultim 100 EDS detector from *Oxford Instruments*, England, at an acceleration voltage of 5 kV and a working distance of 8.2 mm was used. Elemental analysis was carried out in mapping mode with a measurement duration of 30 min.

### 4.2.5 Mechanical Properties

Uniaxial compression testing was performed on cylindrical-shaped samples with dimensions of approx. 34 mm in diameter and 20 mm in height on the universal testing machine *ZwickRoell Z2.5*, Germany, equipped with 50 N and 200 N load cells. A preload of 0.150 N was applied to ensure that the upper pressure plate was in full contact with the sample surface. The samples were compressed at a rate of 10 mm min<sup>-1</sup> up to 40% of their original height, *i.e.*, to 60% strain, before they were decompressed at the same rate to the original height.

### 4.2.6 Hydrophobicity

To show the sample's hydrophobicity, the water drop contact angle  $\theta_c$  was determined by Drop Shape Analyzer DSA 100 from *KRÜSS*, Germany. For this, a water droplet of 5.0  $\mu\text{L}$  was placed on the sample surface, and the contact angle was automatically determined.

### 4.2.7 Solid-State Nuclear Magnetic Resonance Spectroscopy

To analyze the chemical structure of samples during functionalization steps, NMR measurements were performed. The solid-state <sup>13</sup>C-NMR was performed by the NMR Platform of the FSU Jena. Measurements were conducted on an Avance II 400 WB (400.17 MHz, <sup>1</sup>H; 100.6 MHz, <sup>13</sup>C) from *Bruker*, Germany, with a <sup>1</sup>H-<sup>13</sup>C cross polarization pulse program at 10 kHz.

### 4.2.8 Reaction to Fire Test

Reaction to fire tests were performed with a Bunsen burner from *Rothenberg Industrial*, Germany, with a mixture of propane/butane (30/70). The sample was held by a laboratory clamp. Two temperature sensors were used to measure the temperature at the sample's surface and the



inside, respectively. The sensors were connected to a *testo* 922, Germany temperature measurement device, and the data was collected in intervals of 1 s. The sample was treated for 20 s with the direct flame from the Bunsen burner. The distance between the sample surface and the Bunsen burner was set to approx. 10 cm. The following Figure 50 shows the experimental setup of the measurement.

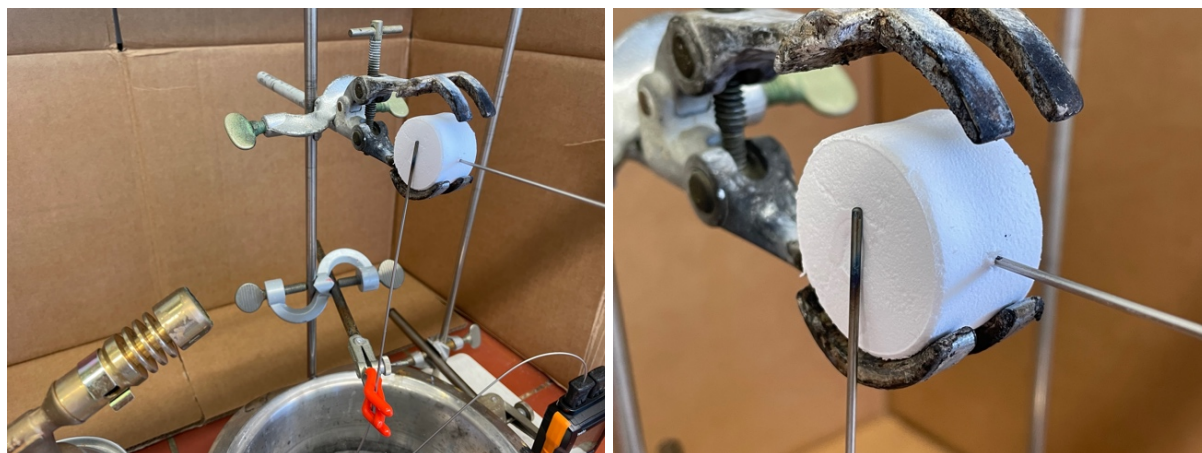


Figure 50: Experimental setup for measuring the monolith's reaction to fire (left). Two sensors were used to measure the temperature during fire treatment at the surface and the inside of the monolith (right).

#### 4.2.9 Thermogravimetric Analysis

TGA was performed on an Iris F1 from *Netzsch*, Germany. For measurement, an 85  $\mu\text{L}$   $\text{Al}_2\text{O}_3$  crucible was filled with 7 – 8 mg of sample. The samples were heated up in a temperature range of 20 – 800°C with 10 K  $\text{min}^{-1}$ . The measurement was performed in a flow of 20  $\text{ml min}^{-1}$  of nitrogen as the inert gas.

#### 4.2.10 Simultaneous Thermal Analysis

STA was performed on an STA 449 F3 from *Netzsch*, Germany. For measurement, an 85  $\mu\text{L}$  PtRh20 crucible with  $\text{Al}_2\text{O}_3$  liner was filled with 4 – 5 mg of sample. The samples were heated up in a temperature range of 35 – 800°C with 10 K  $\text{min}^{-1}$ . The measurement was performed with argon as the inert gas.

#### 4.2.11 Particle Size

The particle size distribution was measured with an LS 13 320 Laser Diffraction Particle Size Analyzer from *Beckman Coulter Inc.*, USA, with a Tornado Dry Powder System. 10 – 20 mL of dry sample were analyzed each at a vacuum of approx. 50 mbar (18.8"  $\text{H}_2\text{O}$ ).

### **4.2.12 Digital Microscopy**

Digital microscopy images were taken by microscope VHX-970F from *Keyence*, Japan. Pictures were taken in bright field mode with a ring light. An objective with 20x and 50x magnification was used. The pictures were digitally optimized to reduce the light reflection from the white sample surface.

## 5 Summary and Outlook

The aim of this work, first, was the improvement of density of organofunctionalized hybrid-silica aerogels, including the development of a simple and low-cost synthesis route based on the sol-gel process for ambient pressure dried aerogel lightweight insulation materials. Therefore, in experiments, the amount of the precursors (MTMS and DMDMS) per volume of aerogel was reduced, leading to lighter samples. To improve the stability and handling of diluted samples, a fiber matrix was incorporated into the aerogels. Further, the material's reaction to fire should be improved due to the introduction of a flame-retardant agent to overcome the disadvantage of the higher reactivity to fire of hybrid silica aerogels in comparison to pure silica ones. Therefore, in the before-investigated synthesis, the precursor MTMS was partially substituted by VTMS for the possibility of the chemically binding of the flame-retardant VPA to the aerogel's network. A second attempt to reduce the density of the final insulation material was to use the natural packing density of spheres and particles. Therefore, a new synthesis procedure for flexible hybrid-silica aerogel particles was investigated. The substitution of MTMS against VTMS for further functionalization was investigated in this step, too. Finally, the material's thermal conductivity should be reduced. Therefore, a hydrophobic aerogel material with ultralow thermal conductivities was used as filler within the "marshmallow-like" hybrid aerogels, resulting in aerogel-aerogel composites.

The results showed that by the variation of only a few synthesis parameters, the aerogel properties could be selectively controlled and adjusted according to the application. The amount of solvent showed a direct impact on the final material density: By adjusting the amount of solvent, the density could be decreased by up to 38%. It could be observed that the overall topology of the sample's microstructure did not change drastically by the variation of the water:MTMS-ratio. The low thermal conductivity of the synthesized samples ( $\sim 32.5 \text{ mW m}^{-1} \text{ K}^{-1}$  at  $25^\circ\text{C}$ ), as well as the hydrophobicity, was not affected within the investigated dilution range. During mechanical testing, a decrease in Young's modulus could be observed.

For fiber composite aerogels, the same densities as samples without fiber matrix could be observed due to improved shrinkage. The thermal conductivities of composite samples are slightly higher than those of pure aerogels. For larger-sized mats, it could be observed that the implementation of fibers is beneficial for the handling and application of the final material without losing their main properties. The aerogels, in general, have a similar performance to the reference sample and values reported in the literature but show a much lower density and are, therefore, better suited for lightweight applications. Further investigation is recommended as a future

course of action: Thermal conductivities should be determined for lower temperatures to evaluate the insulation performance in extreme conditions. Upscaling to larger sample geometries needs to be conducted, as well as the combination with other fiber materials for composites.

The vinyl modification with the flame retardant VPA was successful. Even though the materials got very stable against fire, the functionalization comes along with higher densities, higher thermal conductivities, and loss of flexibility. Further reduction of VTMS and less functionalization with dithiol and VPA could potentially overcome these effects. Therefore, reduced VTMS and flame retardant (VPA) concentrations to maintain the fire resistance while mitigating trade-offs such as increased density and thermal conductivity should be investigated. Alternative flame retardants (phosphorus-based and non-phosphorus ones), as well as further functionalization methods to achieve a better balance of the resulting properties, should be investigated.

A new recipe for the synthesis of particles using emulsion technology has been invented to further reduce the density of the material using the natural packaging density. A third precursor (VTMS) was successfully incorporated up to 50%, giving the potential for further functionalization of the samples (as investigated before for monoliths). The bulk densities were measured in the range of  $\sim 0.05 \text{ g cm}^{-3}$  (which is less than half the value of a reference monolith), and the thermal conductivity was just slightly higher ( $\sim 1 \text{ mW m}^{-1} \text{ K}^{-1}$ ) than their respective monolithic samples. Further testing of VTMS substitution and the functionalization potential to create more advanced, lightweight aerogels should be done in the future. Besides flame retardants, other functional groups could be incorporated for improving the mechanical stability or tailoring other properties related to the potential application.

The incorporation of hydrophobic silica granulates as filler within a flexible monolithic aerogel was somehow successful: Small amounts of granulate could be included. For higher amounts, the samples got too fragile and difficult to handle. The incorporation of granulates came along with an increased density. Other than expected, the thermal conductivity increased with an increasing number of granulates due to insufficient drying technique. The APD process caused a collapse of the granulate within the aerogel matrix. Further research in this direction should be focused on other drying techniques like SCD or freeze-drying to prevent the collapse of the aerogel granulates. Besides this, other types of aerogel granulate could be tested out.

In conclusion, the thesis reflects the many possibilities of the sol-gel process and co-condensation approach with different precursors, as well as an application-related functionalization to tailor properties such as density, hydrophobicity, inner structure, thermal conductivity, sound absorption, and more. The presented results and observations can be used as a basis for further research and synthesis of organofunctionalized silica aerogel monoliths and particles for diverse applications.

## 6 References

- [1] Sejdinović, B., *Modern Thermal Insulation and Sound Insulation Materials*, in *Advanced Technologies, Systems, and Applications VII*, N. Ademović, et al., Editors. 2023, Springer International Publishing: Cham. p. 218-233.
- [2] Schiavoni, S., D'Alessandro, F., Bianchi, F. and Asdrubali, F., *Insulation materials for the building sector: A review and comparative analysis*. Renewable and Sustainable Energy Reviews, 2016. **62**: p. 988-1011. doi:10.1016/j.rser.2016.05.045
- [3] Pedroso, M., de Brito, J. and Silvestre, J.D., *Characterization of eco-efficient acoustic insulation materials (traditional and innovative)*. Construction and Building Materials, 2017. **140**: p. 221-228. doi:10.1016/j.conbuildmat.2017.02.132
- [4] Pavel, C.C. and Blagoeva, D.T., *Competitive landscape of the EU's insulation materials industry for energy-efficient buildings*, EUR 28816 EN, P.O.o.t.E. Union, 2018, doi:10.2760/750646.
- [5] World Health Organization. Regional Office for, E., *Environmental noise guidelines for the European Region*. 2018, Copenhagen: World Health Organization. Regional Office for Europe.
- [6] Hanninen, O., Knol, A.B., Jantunen, M., Lim, T.A., Conrad, A., Rappolder, M., Carrer, P., Fanetti, A.C., Kim, R., Buekers, J., Torfs, R., Iavarone, I., Classen, T., Hornberg, C., Mekel, O.C. and Group, E.B.W., *Environmental burden of disease in Europe: assessing nine risk factors in six countries*. Environ. Health Perspect., 2014. **122**(5): p. 439-46. doi:10.1289/ehp.1206154
- [7] World Health Organization. Regional Office for, E., *Burden of disease from environmental noise: quantification of healthy life years lost in Europe*. 2011, Copenhagen: World Health Organization. Regional Office for Europe.
- [8] Statista, *Market value of acoustic insulation worldwide from 2017 to 2024, by region (in billion U.S. dollars)*. 2020 [Retrieved February 29, 2024]; Available from: <https://www.statista.com/statistics/1098072/global-acoustic-insulation-market-size-by-region/>.
- [9] Fan, J. and Njuguna, J., *1 - An introduction to lightweight composite materials and their use in transport structures*, in *Lightweight Composite Structures in Transport*, J. Njuguna, Editor. 2016, Woodhead Publishing. p. 3-34. doi:10.1016/B978-1-78242-325-6.00001-3
- [10] Refiadi, G., Aisyah, I.S. and Siregar, J.P., *Trends in lightweight automotive materials for improving fuel efficiency and reducing carbon emissions*. Automotive Experiences, 2019. **2**(3): p. 78-90. doi:10.31603/ae.v2i3.2984
- [11] Seydibeyoğlu, M.Ö., Dođru, A., Kandemir, M.B. and Aksoy, Ö., *Lightweight Composite Materials in Transport Structures*, in *Lightweight Polymer Composite Structures*, S.M. Rangappa, et al., Editors. 2020. doi:10.1201/9780429244087
- [12] Zhu, L., Li, N. and Childs, P.R.N., *Light-weighting in aerospace component and system design*. Propulsion and Power Research, 2018. **7**(2): p. 103-119. doi:10.1016/j.jppr.2018.04.001
- [13] Kiran Kumar, A.S., *Lightweighting—Systematic Approach in Aerospace Industry*, in *Light Weighting for Defense, Aerospace, and Transportation*, A. A. Gokhale, N.E. Prasad and B. Basu, Editors. 2019, Springer Singapore: Singapore. p. 121-126. doi:10.1007/978-981-15-1263-6\_9
- [14] Delogu, M., Zanchi, L., Dattilo, C.A. and Pierini, M., *Innovative composites and hybrid materials for electric vehicles lightweight design in a sustainability perspective*. Materials Today Communications, 2017. **13**: p. 192-209. doi:10.1016/j.mtcomm.2017.09.012

- 
- [15] Zhou, X., Jiang, J., Hu, Z. and Hua, L., *Lightweight Materials in Electric Vehicles*. International Journal of Automotive Manufacturing and Materials, 2022. doi:10.53941/ijamm0101003
- [16] Bheekhun, N., Abu Talib, A.R. and Hassan, M.R., *Aerogels in Aerospace: An Overview*. Advances in Materials Science and Engineering, 2013. **2013**: p. 1-18. doi:10.1155/2013/406065
- [17] Sonu, S.S., Rai, N. and Chauhan, I., *Multifunctional Aerogels: A comprehensive review on types, synthesis and applications of aerogels*. J. Sol-Gel Sci. Technol., 2023. **105**(2): p. 324-336. doi:10.1007/s10971-022-06026-1
- [18] Karamikamkar, S., Naguib, H.E. and Park, C.B., *Advances in precursor system for silica-based aerogel production toward improved mechanical properties, customized morphology, and multifunctionality: A review*. Adv. Colloid Interface Sci., 2020. **276**: p. 102101. doi:10.1016/j.cis.2020.102101
- [19] Parale, V.G., Lee, K.-Y. and Park, H.-H., *Flexible and Transparent Silica Aerogels: An Overview*. Journal of the Korean Ceramic Society, 2017. **54**(3): p. 184-199. doi:10.4191/kcers.2017.54.3.12
- [20] Shimizu, T., Kanamori, K. and Nakanishi, K., *Silicone-Based Organic-Inorganic Hybrid Aerogels and Xerogels*. Chemistry, 2017. **23**(22): p. 5176-5187. doi:10.1002/chem.201603680
- [21] Kistler, S.S., *Coherent Expanded Aerogels and Jellies*. Nature, 1931. **127**(3211): p. 741-741. doi:10.1038/127741a0
- [22] Aegerter, M.A., Leventis, N. and Koebel, M.M., *Aerogels Handbook*. 2011. doi:10.1007/978-1-4419-7589-8
- [23] Hüsing, N. and Schubert, U., *Aerogels—Airy Materials: Chemistry, Structure, and Properties*. Angew. Chem. Int. Ed., 1998. **37**(1-2): p. 22-45. doi:10.1002/(sici)1521-3773(19980202)37:1/2<22::Aid-anie22>3.0.Co;2-i
- [24] Smirnova, I. and Gurikov, P., *Aerogel production: Current status, research directions, and future opportunities*. The Journal of Supercritical Fluids, 2018. **134**: p. 228-233. doi:10.1016/j.supflu.2017.12.037
- [25] Alemán, J.V., Chadwick, A.V., He, J., Hess, M., Horie, K., Jones, R.G., Kratochvíl, P., Meisel, I., Mita, I., Moad, G., Penczek, S. and Stepto, R.F.T., *Definitions of terms relating to the structure and processing of sols, gels, networks, and inorganic-organic hybrid materials (IUPAC Recommendations 2007)*. Pure Appl. Chem., 2007. **79**(10): p. 1801-1829. doi:10.1351/pac200779101801
- [26] *Springer Handbook of Aerogels*. 1 ed. Springer Handbooks. 2023: Springer Cham. doi:10.1007/978-3-030-27322-4
- [27] Jung, S.M., Jung, H.Y., Dresselhaus, M.S., Jung, Y.J. and Kong, J., *A facile route for 3D aerogels from nanostructured 1D and 2D materials*. Sci Rep, 2012. **2**: p. 849. doi:10.1038/srep00849
- [28] Mecklenburg, M., Schuchardt, A., Mishra, Y.K., Kaps, S., Adelung, R., Lotnyk, A., Kienle, L. and Schulte, K., *Aerographite: ultra lightweight, flexible nanowall, carbon microtube material with outstanding mechanical performance*. Adv. Mater., 2012. **24**(26): p. 3486-90. doi:10.1002/adma.201200491
- [29] Ron, R., Haleva, E. and Salomon, A., *Nanoporous Metallic Networks: Fabrication, Optical Properties, and Applications*. Adv. Mater., 2018. **30**(41): p. e1706755. doi:10.1002/adma.201706755
- [30] Müller, A., Putz, Y., Oberhoffer, R., Becker, N., Strey, R., Wiedenmann, A. and Sottmann, T., *Kinetics of pressure induced structural changes in super- or near-critical CO<sub>2</sub>-microemulsions*. Phys. Chem. Chem. Phys., 2014. **16**(34): p. 18092-7. doi:10.1039/c3cp53790k
-

- [31] Tappan, B.C., Huynh, M.H., Hiskey, M.A., Chavez, D.E., Luther, E.P., Mang, J.T. and Son, S.F., *Ultralow-density nanostructured metal foams: combustion synthesis, morphology, and composition*. J. Am. Chem. Soc., 2006. **128**(20): p. 6589-94. doi:10.1021/ja056550k
- [32] Orgaz, F. and Rawson, H., *Characterization of various stages of the sol-gel process*. J. Non-Cryst. Solids, 1986. **82**(1-3): p. 57-68. doi:10.1016/0022-3093(86)90111-0
- [33] Brinker, C.J. and Scherer, G.W., *Sol-Gel Science*. 1st ed. 1990: Academic Press. 924. doi:10.1016/c2009-0-22386-5
- [34] Levy, D. and Zayat, M., *The Sol-Gel Handbook*. 2015. doi:10.1002/9783527670819
- [35] Ratke, L., *Aerogels - A Practical Workshop*. 2016, Köln: Institut für Werkstoff-Forschung, Deutsches Zentrum für Luft- und Raumfahrt e.V.
- [36] DataPhysics Instruments GmbH, *Surface tension values of some common test liquids for surface energy analysis*. [Retrieved March 07, 2024]; Available from: <https://www.dataphysics-instruments.com/Downloads/Surface-Tensions-Energies.pdf>.
- [37] Montes, S. and Maleki, H., *Aerogels and their applications*, in *Colloidal Metal Oxide Nanoparticles*, S. Thomas, A.T. Sunny and P. Velayudhan, Editors. 2020, Matthew Deans. p. 337-399. doi:10.1016/b978-0-12-813357-6.00015-2
- [38] Lin, Y.-F., Syu, C.-R., Huang, K.-W. and Lin, K.-Y.A., *Synthesis of silica aerogel membranes using low-cost silicate precursors for carbon dioxide capture*. Chem. Phys. Lett., 2019. **726**: p. 13-17. doi:10.1016/j.cplett.2019.04.017
- [39] Linneen, N., Pfeffer, R. and Lin, Y.S., *CO<sub>2</sub> capture using particulate silica aerogel immobilized with tetraethylenepentamine*. Microporous Mesoporous Mater., 2013. **176**: p. 123-131. doi:10.1016/j.micromeso.2013.02.052
- [40] Domínguez, M., Taboada, E., Molins, E. and Llorca, J., *Co-SiO<sub>2</sub> aerogel-coated catalytic walls for the generation of hydrogen*. Catal. Today, 2008. **138**(3-4): p. 193-197. doi:10.1016/j.cattod.2008.05.027
- [41] Domínguez, M., Taboada, E., Idriss, H., Molins, E. and Llorca, J., *Fast and efficient hydrogen generation catalyzed by cobalt talc nanolayers dispersed in silica aerogel*. J. Mater. Chem., 2010. **20**(23). doi:10.1039/c0jm00184h
- [42] Venkateswara Rao, A., Bhagat, S.D., Hirashima, H. and Pajonk, G.M., *Synthesis of flexible silica aerogels using methyltrimethoxysilane (MTMS) precursor*. J. Colloid Interface Sci., 2006. **300**(1): p. 279-285. doi:10.1016/j.jcis.2006.03.044
- [43] Venkateswara Rao, A., Hegde, N.D. and Hirashima, H., *Absorption and desorption of organic liquids in elastic superhydrophobic silica aerogels*. J. Colloid Interface Sci., 2007. **305**(1): p. 124-32. doi:10.1016/j.jcis.2006.09.025
- [44] Wang, C.-T., Wu, C.-L., Chen, I.C. and Huang, Y.-H., *Humidity sensors based on silica nanoparticle aerogel thin films*. Sensors and Actuators B: Chemical, 2005. **107**(1): p. 402-410. doi:10.1016/j.snb.2004.10.034
- [45] Li, Y.K., Yang, D.K., Chen, Y.C., Su, H.J., Wu, J.C. and Chen-Yang, Y.W., *A novel three-dimensional aerogel biochip for molecular recognition of nucleotide acids*. Acta Biomater, 2010. **6**(4): p. 1462-70. doi:10.1016/j.actbio.2009.10.001
- [46] Kim, G.S., Hyun, S.H. and Park, H.H., *Synthesis of Low-Dielectric Silica Aerogel Films by Ambient Drying*. J. Am. Ceram. Soc., 2004. **84**(2): p. 453-55. doi:10.1111/j.1151-2916.2001.tb00677.x
- [47] Park, S.-W., Jung, S.-B., Kang, M.-G., Park, H.-H. and Kim, H.-C., *Modification of GaAs and copper surface by the formation of SiO<sub>2</sub> aerogel film as an interlayer dielectric*. Appl. Surf. Sci., 2003. **216**(1-4): p. 98-105. doi:10.1016/s0169-4332(03)00488-4
- [48] Iglesias-Mejuto, A. and García-González, C.A., *3D-printed alginate-hydroxyapatite aerogel scaffolds for bone tissue engineering*. Materials Science and Engineering: C, 2021. **131**: p. 112525. doi:10.1016/j.msec.2021.112525



- [49] Veres, P., Kéri, M., Bányai, I., Lázár, I., Fábrián, I., Domingo, C. and Kalmár, J., *Mechanism of drug release from silica-gelatin aerogel—Relationship between matrix structure and release kinetics*. Colloids and Surfaces B: Biointerfaces, 2017. **152**: p. 229-237. doi:10.1016/j.colsurfb.2017.01.019
- [50] Mahmoudpour, M., Dolatabadi, J.E.-N., Hasanzadeh, M. and Soleymani, J., *Carbon-based aerogels for biomedical sensing: Advances toward designing the ideal sensor*. Adv. Colloid Interface Sci., 2021. **298**: p. 102550. doi:10.1016/j.cis.2021.102550
- [51] Fidalgo, A., Rosa, M.E. and Ilharco, L.M., *Chemical Control of Highly Porous Silica Xerogels: Physical Properties and Morphology*. Chem. Mater., 2003. **15**(11): p. 2186-2192. doi:10.1021/cm031013p
- [52] Kanamori, K. and Nakanishi, K., *Controlled pore formation in organotrialkoxysilane-derived hybrids: from aerogels to hierarchically porous monoliths*. Chem. Soc. Rev., 2011. **40**(2): p. 754-770. doi:10.1039/C0CS00068J
- [53] Hayase, G., Kanamori, K. and Nakanishi, K., *Structure and properties of polymethylsilsesquioxane aerogels synthesized with surfactant n-hexadecyltrimethylammonium chloride*. Microporous Mesoporous Mater., 2012. **158**: p. 247-252. doi:10.1016/j.micromeso.2012.03.049
- [54] Kanamori, K., Aizawa, M., Nakanishi, K. and Hanada, T., *Elastic organic-inorganic hybrid aerogels and xerogels*. J. Sol-Gel Sci. Technol., 2008. **48**(1-2): p. 172-181. doi:10.1007/s10971-008-1756-6
- [55] Meyer, M., Fischer, A. and Hoffmann, H., *Novel Ringing Silica Gels That Do Not Shrink*. The Journal of Physical Chemistry B, 2002. **106**(7): p. 1528-1533. doi:10.1021/jp013371q
- [56] Vareda, J.P., Maximiano, P., Cunha, L.P., Ferreira, A.F., Simoes, P.N. and Duraes, L., *Effect of different types of surfactants on the microstructure of methyltrimethoxysilane-derived silica aerogels: A combined experimental and computational approach*. J. Colloid Interface Sci., 2018. **512**: p. 64-76. doi:10.1016/j.jcis.2017.10.035
- [57] He, S. and Chen, X., *Flexible silica aerogel based on methyltrimethoxysilane with improved mechanical property*. J. Non-Cryst. Solids, 2017. **463**: p. 6-11. doi:10.1016/j.jnoncrysol.2017.02.014
- [58] Kanamori, K., Nakanishi, K. and Hanada, T., *Sol-gel synthesis, porous structure, and mechanical property of polymethylsilsesquioxane aerogels*. J. Ceram. Soc. Jpn., 2009. **117**(1372): p. 1333-1338. doi:10.2109/jcersj2.117.1333
- [59] Venkateswara Rao, A. and Haranath, D., *Effect of methyltrimethoxysilane as a synthesis component on the hydrophobicity and some physical properties of silica aerogels*. Microporous Mesoporous Mater., 1999. **30**(2): p. 267-273. doi:10.1016/S1387-1811(99)00037-2
- [60] Kanamori, K., Aizawa, M., Nakanishi, K. and Hanada, T., *New Transparent Methylsilsesquioxane Aerogels and Xerogels with Improved Mechanical Properties*. Adv. Mater., 2007. **19**(12): p. 1589-1593. doi:10.1002/adma.200602457
- [61] Hayase, G., Kanamori, K. and Nakanishi, K., *New flexible aerogels and xerogels derived from methyltrimethoxysilane/dimethyldimethoxysilane co-precursors*. J. Mater. Chem., 2011. **21**(43): p. 17077-17079. doi:10.1039/c1jm13664j
- [62] Guo, H., Nguyen, B.N., McCorkle, L.S., Shonkwiler, B. and Meador, M.A.B., *Elastic low density aerogels derived from bis[3-(triethoxysilyl)propyl]disulfide, tetramethylorthosilicate and vinyltrimethoxysilane via a two-step process*. J. Mater. Chem., 2009. **19**(47). doi:10.1039/b916355g
- [63] Hayase, G., Kanamori, K., Fukuchi, M., Kaji, H. and Nakanishi, K., *Facile synthesis of marshmallow-like macroporous gels usable under harsh conditions for the separation of oil and water*. Angew. Chem. Int. Ed. Engl., 2013. **52**(7): p. 1986-9. doi:10.1002/anie.201207969

- [64] Matias, T., Varino, C., de Sousa, H.C., Braga, M.E.M., Portugal, A., Coelho, J.F.J. and Durães, L., *Novel flexible, hybrid aerogels with vinyl- and methyltrimethoxysilane in the underlying silica structure*. Journal of Materials Science, 2016. **51**(14): p. 6781-6792. doi:10.1007/s10853-016-9965-9
- [65] Ehgartner, C.R., Grandl, S., Feinle, A. and Husing, N., *Flexible organofunctional aerogels*. Dalton Trans, 2017. **46**(27): p. 8809-8817. doi:10.1039/c7dt00558j
- [66] Matějka, L., Dukh, O., Hlavatá, D., Meissner, B. and Brus, J., *Cyclization and Self-Organization in Polymerization of Trialkoxysilanes*. Macromolecules, 2001. **34**(20): p. 6904-6914. doi:10.1021/ma010136x
- [67] Beard, A., Battenberg, C. and Sutker, B.J., *Flame Retardants*, in *Ullmann's Encyclopedia of Industrial Chemistry*. 2021. p. 1-26. doi:10.1002/14356007.a11\_123.pub2
- [68] Schartel, B., *Phosphorus-based Flame Retardancy Mechanisms-Old Hat or a Starting Point for Future Development?* Materials (Basel), 2010. **3**(10): p. 4710-4745. doi:10.3390/ma3104710
- [69] Liu, Z., Liu, J., Liu, Z., Wang, H., Ou, J., Ye, M. and Zou, H., *Functionalization of hybrid monolithic columns via thiol-ene click reaction for proteomics analysis*. J. Chromatogr. A, 2017. **1498**: p. 29-36. doi:10.1016/j.chroma.2017.01.029
- [70] Li, Z., Zhao, S., Koebel, M.M. and Malfait, W.J., *Silica aerogels with tailored chemical functionality*. Materials & Design, 2020. **193**: p. 108833. doi:10.1016/j.matdes.2020.108833
- [71] Clyne, T.W. and Hull, D., *An Introduction to Composite Materials*. 3 ed. 2019, Cambridge: Cambridge University Press. doi:DOI: 10.1017/9781139050586
- [72] Parmenter, K.E. and Milstein, F., *Mechanical properties of silica aerogels*. J. Non-Cryst. Solids, 1998. **223**(3): p. 179-189. doi:10.1016/S0022-3093(97)00430-4
- [73] Liao, Y., Wu, H., Ding, Y., Yin, S., Wang, M. and Cao, A., *Engineering thermal and mechanical properties of flexible fiber-reinforced aerogel composites*. J. Sol-Gel Sci. Technol., 2012. **63**(3): p. 445-456. doi:10.1007/s10971-012-2806-7
- [74] Maleki, H., Durães, L. and Portugal, A., *An overview on silica aerogels synthesis and different mechanical reinforcing strategies*. J. Non-Cryst. Solids, 2014. **385**: p. 55-74. doi:10.1016/j.jnoncrysol.2013.10.017
- [75] Yang, X., Sun, Y. and Shi, D., *Experimental investigation and modeling of the creep behavior of ceramic fiber-reinforced SiO<sub>2</sub> aerogel*. J. Non-Cryst. Solids, 2012. **358**(3): p. 519-524. doi:10.1016/j.jnoncrysol.2011.11.028
- [76] Rege, A., Voepel, P., Okumus, E., Hillgartner, M., Itskov, M. and Milow, B., *Temperature-Dependent Stiffening and Inelastic Behavior of Newly Synthesized Fiber-Reinforced Super Flexible Silica Aerogels*. Materials (Basel), 2019. **12**(18). doi:10.3390/ma12182878
- [77] Welsch, T., Vievers, Y., Schnellenbach-Held, M., Bialuschewski, D. and Milow, B., *Comparison of Different Aerogel Granules for Use as Aggregate in Concrete*. Gels, 2023. **9**(5). doi:10.3390/gels9050406
- [78] Fickler, S., Milow, B., Ratke, L., Schnellenbach-Held, M. and Welsch, T., *Development of High Performance Aerogel Concrete*. Energy Procedia, 2015. **78**: p. 406-411. doi:10.1016/j.egypro.2015.11.684
- [79] Gao, T., Jelle, B.P., Gustavsen, A. and Jacobsen, S., *Aerogel-incorporated concrete: An experimental study*. Construction and Building Materials, 2014. **52**: p. 130-136. doi:10.1016/j.conbuildmat.2013.10.100
- [80] Guzel Kaya, G. and Deveci, H., *Synergistic effects of silica aerogels/xerogels on properties of polymer composites: A review*. Journal of Industrial and Engineering Chemistry, 2020. **89**: p. 13-27. doi:10.1016/j.jiec.2020.05.019

- [81] Aminoroaya, A., Bagheri, R., Nouri Khorasani, S., Talebi, Z., Derakhshanfar, P. and Esmaeely Neisiany, R., *Mesoporous silica aerogel reinforced dental composite: Effects of microstructure and surface modification*. J Mech Behav Biomed Mater, 2022. **125**: p. 104947. doi:10.1016/j.jmbbm.2021.104947
- [82] Milow, B. and Ratke, L., *Aerogel-Aerogel-Verbundwerkstoff*, European Patent EP2638217B1, 2011.
- [83] Laskowski, J., Milow, B. and Ratke, L., *Aerogel-aerogel composites for normal temperature range thermal insulations*. J. Non-Cryst. Solids, 2016. **441**: p. 42-48. doi:10.1016/j.jnoncrysol.2016.03.020
- [84] Laskowski, J., Milow, B. and Ratke, L., *The effect of embedding highly insulating granular aerogel in cellulosic aerogel*. The Journal of Supercritical Fluids, 2015. **106**: p. 93-99. doi:10.1016/j.supflu.2015.05.011
- [85] Laskowski, J., *Synthese und Eigenschaften von Aerogel-Aerogel-Verbundwerkstoffen*, in *Chair of Materials Chemistry*. 2016, Rheinisch-Westfälische Technische Hochschule Aachen.
- [86] Niemeyer, P. and Milow, B., *Herstellung von hybriden Aerogelen*, European Patent EP4342578A1, 2023.
- [87] Shi, W., Ching, Y.C. and Chuah, C.H., *Preparation of aerogel beads and microspheres based on chitosan and cellulose for drug delivery: A review*. Int. J. Biol. Macromol., 2021. **170**: p. 751-767. doi:10.1016/j.ijbiomac.2020.12.214
- [88] Yu, Y., Guo, D. and Fang, J., *A Facile and Fast Gelation Process to Prepare Highly Spherical Millimeter-Sized Silica Aerogel Beads*. International Journal of Applied Ceramic Technology, 2015. **12**: p. E244-E248. doi:10.1111/ijac.12403
- [89] Yun, S., Luo, H. and Gao, Y., *Superhydrophobic silica aerogel microspheres from methyltrimethoxysilane: rapid synthesis via ambient pressure drying and excellent absorption properties*. RSC Adv., 2014. **4**(9): p. 4535-4542. doi:10.1039/c3ra46911e
- [90] Alnaief, M. and Smirnova, I., *In situ production of spherical aerogel microparticles*. The Journal of Supercritical Fluids, 2011. **55**(3): p. 1118-1123. doi:10.1016/j.supflu.2010.10.006
- [91] Chen, Q., Wang, H. and Sun, L., *Preparation and Characterization of Silica Aerogel Microspheres*. Materials (Basel), 2017. **10**(4). doi:10.3390/ma10040435
- [92] Hayase, G. and Ohya, Y., *Marshmallow-like silicone gels as flexible thermal insulators and liquid nitrogen retention materials and their application in containers for cryopreserved embryos*. Applied Materials Today, 2017. **9**: p. 560-565. doi:10.1016/j.apmt.2017.10.004
- [93] Hayase, G., Kanamori, K., Fukuchi, M., Kaji, H. and Nakanishi, K., *Facile Synthesis of Marshmallow-like Macroporous Gels Usable under Harsh Conditions for the Separation of Oil and Water*. Angew. Chem. Int. Ed., 2013. **52**(7): p. 1986-1989. doi:10.1002/anie.201207969
- [94] Wang, J. and Wang, H., *Ultra-hydrophobic and mesoporous silica aerogel membranes for efficient separation of surfactant-stabilized water-in-oil emulsion separation*. Sep. Purif. Technol., 2019. **212**: p. 597-604. doi:10.1016/j.seppur.2018.11.078
- [95] Li, Z., Huang, S., Shi, L., Li, Z., Liu, Q. and Li, M., *Reducing the flammability of hydrophobic silica aerogels by doping with hydroxides*. J. Hazard. Mater., 2019. **373**: p. 536-546. doi:10.1016/j.jhazmat.2019.03.112
- [96] Li, Z., Cheng, X., Shi, L., He, S., Gong, L., Li, C. and Zhang, H., *Flammability and oxidation kinetics of hydrophobic silica aerogels*. J. Hazard. Mater., 2016. **320**: p. 350-358. doi:10.1016/j.jhazmat.2016.07.054
- [97] Hayase, G., Kanamori, K., Hasegawa, G., Maeno, A., Kaji, H. and Nakanishi, K., *A superamphiphobic macroporous silicone monolith with marshmallow-like flexibility*. Angew. Chem. Int. Ed. Engl., 2013. **52**(41): p. 10788-91. doi:10.1002/anie.201304169

- [98] Kistler, S.S., *Coherent Expanded Aerogels*. Rubber Chem. Technol., 1932. **5**(4): p. 600-603. doi:10.5254/1.3539386
- [99] Al-sharuee, I.F., *Thermal Conductivity Performance of Silica Aerogel after Exposition on Different Heating under Ambient Pressure*. Baghdad Science Journal, 2019. **16**(3(Suppl.)). doi:10.21123/bsj.2019.16.3(Suppl.).0770
- [100] Nadargi, D.Y., Latthe, S.S. and Venkateswara Rao, A., *Effect of post-treatment (gel aging) on the properties of methyltrimethoxysilane based silica aerogels prepared by two-step sol-gel process*. J. Sol-Gel Sci. Technol., 2008. **49**(1): p. 53-59. doi:10.1007/s10971-008-1830-0
- [101] Kwon, Y.-G., Choi, S.-Y., Kang, E.-S. and Baek, S.-S., *Ambient-dried silica aerogel doped with TiO<sub>2</sub> powder for thermal insulation*. Journal of Materials Science, 2000. **35**(24): p. 6075-6079. doi:10.1023/A:1026775632209
- [102] Schmidt, M. and Schwertfeger, F., *Applications for silica aerogel products*. J. Non-Cryst. Solids, 1998. **225**: p. 364-368. doi:10.1016/s0022-3093(98)00054-4
- [103] Dong, W., Faltens, T., Pantell, M., Simon, D., Thompson, T. and Dong, W., *Acoustic Properties of Organic/Inorganic Composite Aerogels*. MRS Online Proceedings Library, 2009. **1188**(1): p. 173-183. doi:10.1557/PROC-1188-LL07-02
- [104] Cai, J.Y., Lucas, S., Wang, L.J. and Cao, Y., *Insulation Properties of the Monolithic and Flexible Aerogels Prepared at Ambient Pressure*. Advanced Materials Research, 2011. **391-392**: p. 116-120. doi:10.4028/www.scientific.net/AMR.391-392.116
- [105] Yan, P., Zhou, B. and Du, A., *Synthesis of polyimide cross-linked silica aerogels with good acoustic performance*. RSC Adv., 2014. **4**(102): p. 58252-58259. doi:10.1039/c4ra08846h
- [106] Dourbash, A., Buratti, C., Belloni, E. and Motahari, S., *Preparation and characterization of polyurethane/silica aerogel nanocomposite materials*. J. Appl. Polym. Sci., 2016. **134**(8). doi:10.1002/app.44521
- [107] Eskandari, N., Motahari, S., Atoufi, Z., Hashemi Motlagh, G. and Najafi, M., *Thermal, mechanical, and acoustic properties of silica-aerogel/UPVC composites*. J. Appl. Polym. Sci., 2016. **134**(14). doi:10.1002/app.44685
- [108] Merli, F., Anderson, A.M., Carroll, M.K. and Buratti, C., *Acoustic measurements on monolithic aerogel samples and application of the selected solutions to standard window systems*. Applied Acoustics, 2018. **142**: p. 123-131. doi:10.1016/j.apacoust.2018.08.008
- [109] Buratti, C., Merli, F. and Moretti, E., *Aerogel-based materials for building applications: Influence of granule size on thermal and acoustic performance*. Energy and Buildings, 2017. **152**: p. 472-482. doi:10.1016/j.enbuild.2017.07.071
- [110] Moretti, E., Merli, F., Cuce, E. and Buratti, C., *Thermal and Acoustic Properties of Aerogels: Preliminary Investigation of the Influence of Granule Size*. Energy Procedia, 2017. **111**: p. 472-480. doi:10.1016/j.egypro.2017.03.209
- [111] Hüsing, N., Schwertfeger, F., Tappert, W. and Schubert, U., *Influence of supercritical drying fluid on structure and properties of organically modified silica aerogels*. J. Non-Cryst. Solids, 1995. **186**: p. 37-43. doi:10.1016/0022-3093(95)00031-3
- [112] Venkateswara Rao, A., Kulkarni, M.M., Amalnerkar, D.P. and Seth, T., *Surface chemical modification of silica aerogels using various alkyl-alkoxy/chloro silanes*. Appl. Surf. Sci., 2003. **206**(1): p. 262-270. doi:10.1016/S0169-4332(02)01232-1
- [113] Ingale, S.V., Wagh, P.B., Tripathi, A.K., Kamble, V.S., Kumar, R. and Gupta, S.C., *Physico-chemical properties of silica aerogels prepared from TMOS/MTMS mixtures*. J. Porous Mater., 2011. **18**(5): p. 567-572. doi:10.1007/s10934-010-9410-4
- [114] Mahadik, D.B., Venkateswara Rao, A., Parale, V.G., Kavale, M.S., Wagh, P.B., Ingale, S.V. and Gupta, S.C., *Effect of surface composition and roughness on the apparent*

- surface free energy of silica aerogel materials*. Appl. Phys. Lett., 2011. **99**(10). doi:10.1063/1.3635398
- [115] Gutzov, S., Danchova, N., Karakashev, S.I., Khristov, M., Ivanova, J. and Ulbikas, J., *Preparation and thermal properties of chemically prepared nanoporous silica aerogels*. J. Sol-Gel Sci. Technol., 2014. **70**(3): p. 511-516. doi:10.1007/s10971-014-3315-7
- [116] Hossain, M.D., Hassan, M.K., Yuen, A.C.Y., He, Y., Saha, S. and Hittini, W., *Flame behaviour, fire hazard and fire testing approach for lightweight composite claddings – a review*. Journal of Structural Fire Engineering, 2021. **12**(3): p. 257-292. doi:10.1108/jsfe-09-2020-0027
- [117] Hull, T.R., *Challenges in fire testing: reaction to fire tests and assessment of fire toxicity*, in *Advances in Fire Retardant Materials*. 2008. p. 255-290. doi:10.1533/9781845694701.2.255
- [118] DIN EN 13501-1:2018 (2018): *Fire classification of construction products and building elements - Part 1: Classification using data from reaction to fire tests*. Beuth Verlag, Berlin, 2018. doi:10.31030/2870379
- [119] ASTM E84-23d (2023): *Standard Test Method for Surface Burning Characteristics of Building Materials*. West Conshohocken, PA, ASTM International, 2023. doi:10.1520/E0084-23D
- [120] ISO 5660-1:2015 (2015): *Reaction-to-fire tests - Heat release, smoke production and mass loss rate - Part 1: Heat release rate (cone calorimeter method) and smoke production rate (dynamic measurement)*. International Organization for Standardization, Geneva, 2015.
- [121] Windisch, H., *Thermodynamik*. 2023. doi:10.1515/9783111080192
- [122] Yang, H., Jiang, Y., Liu, H., Xie, D., Wan, C., Pan, H. and Jiang, S., *Mechanical, thermal and fire performance of an inorganic-organic insulation material composed of hollow glass microspheres and phenolic resin*. J. Colloid Interface Sci., 2018. **530**: p. 163-170. doi:10.1016/j.jcis.2018.06.075
- [123] Tychanicz-Kwiecień, M., Wilk, J. and Gil, P., *Review of High-Temperature Thermal Insulation Materials*. J. Thermophys Heat Transfer, 2019. **33**(1): p. 271-284. doi:10.2514/1.T5420
- [124] Hung Anh, L.D. and Pásztor, Z., *An overview of factors influencing thermal conductivity of building insulation materials*. Journal of Building Engineering, 2021. **44**. doi:10.1016/j.jobe.2021.102604
- [125] Jelle, B.P., *Traditional, state-of-the-art and future thermal building insulation materials and solutions – Properties, requirements and possibilities*. Energy and Buildings, 2011. **43**(10): p. 2549-2563. doi:10.1016/j.enbuild.2011.05.015
- [126] Lou, F., Dong, S., Zhu, K., Chen, X. and Ma, Y., *Thermal Insulation Performance of Aerogel Nano-Porous Materials: Characterization and Test Methods*. Gels, 2023. **9**(3). doi:10.3390/gels9030220
- [127] Caps, R. and Fricke, J., *Radiative Heat Transfer in Silica Aerogel*, in *Aerogels*, J. Fricke, Editor. 1986, Springer: Berlin, Heidelberg. p. 110-115. doi:10.1007/978-3-642-93313-4\_13
- [128] Hrubesh, L.W. and Pekala, R.W., *Thermal properties of organic and inorganic aerogels*. J. Mater. Res., 1994. **9**(3): p. 731-738. doi:10.1557/jmr.1994.0731
- [129] Demilecamps, A., Alves, M., Rigacci, A., Reichenauer, G. and Budtova, T., *Nanostructured interpenetrated organic-inorganic aerogels with thermal superinsulating properties*. J. Non-Cryst. Solids, 2016. **452**: p. 259-265. doi:10.1016/j.jnoncrsol.2016.09.003
- [130] Cao, L., Fu, Q., Si, Y., Ding, B. and Yu, J., *Porous materials for sound absorption*. Composites Communications, 2018. **10**: p. 25-35. doi:10.1016/j.coco.2018.05.001

- [131] Bujoreanu, C., Nedeff, F., Benchea, M. and Agop, M., *Experimental and theoretical considerations on sound absorption performance of waste materials including the effect of backing plates*. Applied Acoustics, 2017. **119**: p. 88-93. doi:10.1016/j.apacoust.2016.12.010
- [132] Peng, L., Song, B., Wang, J. and Wang, D., *Mechanic and Acoustic Properties of the Sound-Absorbing Material Made from Natural Fiber and Polyester*. Advances in Materials Science and Engineering, 2015. **2015**: p. 1-5. doi:10.1155/2015/274913
- [133] Lawrence E. Kinsler, Austin R. Frey, Alan B. Coppens and Sanders, J.V., *Fundamentals of Acoustics*. 4th ed. 2000: John Wiley & Sons.
- [134] Rahimabady, M., Statharas, E.C., Yao, K., Sharifzadeh Mirshekarloo, M., Chen, S. and Tay, F.E.H., *Hybrid local piezoelectric and conductive functions for high performance airborne sound absorption*. Appl. Phys. Lett., 2017. **111**(24). doi:10.1063/1.5010743
- [135] *Foundations of Engineering Acoustics*. 1st ed, ed. F. Fahy. 2001, London: Academic Press. 443. doi:10.1016/b978-0-12-247665-5.X5000-0
- [136] Budtova, T., Lokki, T., Malakooti, S., Rege, A., Lu, H., Milow, B., Vapaavuori, J. and Vivod, S.L., *Acoustic Properties of Aerogels: Current Status and Prospects*. Adv. Eng. Mater., 2022. **25**(6). doi:10.1002/adem.202201137
- [137] Kuczumarski, M.A. and Johnston, J.C., *Acoustic Absorption in Porous Materials*. 2011, NASA Glenn Research Center.
- [138] Emergen Research, *Acoustic Insulation Market By Type (Glass Wool, Rock Wool, Foamed Plastics, and Elastomeric), By End-Use (Building & Construction, Transportation, Oil & Gas, Petrochemical, Energy and Utilities, Industrial, and OEM), and By Region Forecast to 2030*. 2022 [Retrieved April 10, 2024]; Available from: <https://www.emergenresearch.com/industry-report/acoustic-insulation-market>.
- [139] Mordor Intelligence, *AEROGEL MARKET SIZE & SHARE ANALYSIS - GROWTH TRENDS & FORECASTS (2024 - 2029)*. 2024 [Retrieved July 26, 2024]; Available from: <https://www.mordorintelligence.com/industry-reports/aerogel-market/companies>.
- [140] Aspen Aerogels Inc., *Solving the World's Toughest Sustainability Challenges | Aspen Aerogels*. 2024 [Retrieved July 26, 2024]; Available from: <https://www.aerogel.com>.
- [141] Cabot Corporation, *Aerogels*. 2024 [Retrieved July 26, 2024]; Available from: <https://www.cabotcorp.com/solutions/products-plus/aerogel>.
- [142] Steffens, K., Bialuschewski, D. and Milow, B., *Tuning density and morphology of organic-inorganic hybrid-silica aerogels through precursor dilution for lightweight applications*. J. Sol-Gel Sci. Technol., 2024. **112**(3): p. 768-775. doi:10.1007/s10971-024-06572-w
- [143] Emmerling, A. and Fricke, J., *Small angle scattering and the structure of aerogels*. J. Non-Cryst. Solids, 1992. **145**: p. 113-120. doi:10.1016/s0022-3093(05)80439-9
- [144] Schubert, U., *Chemistry and Fundamentals of the Sol-Gel Process*, in *The Sol-Gel Handbook*, D. Levy and M. Zayat, Editors. 2015, Wiley-VCH Verlag GmbH & Co. KGaA: Weinheim. p. 1-28. doi:10.1002/9783527670819.ch01
- [145] Venkateswara Rao, A., Kulkarni, M.M., Amalnerkar, D.P. and Seth, T., *Superhydrophobic silica aerogels based on methyltrimethoxysilane precursor*. J. Non-Cryst. Solids, 2003. **330**(1-3): p. 187-195. doi:10.1016/j.jnoncrysol.2003.08.048
- [146] Wei, G., Wang, L., Xu, C., Du, X. and Yang, Y., *Thermal conductivity investigations of granular and powdered silica aerogels at different temperatures and pressures*. Energy and Buildings, 2016. **118**: p. 226-231. doi:10.1016/j.enbuild.2016.03.008
- [147] Wei, G., Liu, Y., Zhang, X., Yu, F. and Du, X., *Thermal conductivities study on silica aerogel and its composite insulation materials*. Int. J. Heat Mass Transfer, 2011. **54**(11-12): p. 2355-2366. doi:10.1016/j.ijheatmasstransfer.2011.02.026

- [148] Dai, Y.-J., Tang, Y.-Q., Fang, W.-Z., Zhang, H. and Tao, W.-Q., *A theoretical model for the effective thermal conductivity of silica aerogel composites*. Appl. Therm. Eng., 2018. **128**: p. 1634-1645. doi:10.1016/j.applthermaleng.2017.09.010
- [149] Long, M., *Sound Transmission Loss*, in *Architectural Acoustics*. 2014. p. 345-382. doi:10.1016/b978-0-12-398258-2.00009-x
- [150] Arunkumar, M.P., Pitchaimani, J., Gangadharan, K.V. and Lenin Babu, M.C., *Sound transmission loss characteristics of sandwich aircraft panels: Influence of nature of core*. Journal of Sandwich Structures & Materials, 2016. **19**(1): p. 26-48. doi:10.1177/1099636216652580
- [151] Iswar, S., Galmarini, S., Bonanomi, L., Wernery, J., Roumeli, E., Nimalshantha, S., Ben Ishai, A.M., Lattuada, M., Koebel, M.M. and Malfait, W.J., *Dense and strong, but superinsulating silica aerogel*. Acta Mater., 2021. **213**. doi:10.1016/j.actamat.2021.116959
- [152] Fricke, J., *Aerogels — highly tenuous solids with fascinating properties*. J. Non-Cryst. Solids, 1988. **100**(1-3): p. 169-173. doi:10.1016/0022-3093(88)90014-2
- [153] Pekalaa, R.W., Hrubesh, L.W., Tillotson, T.M., Alviso, C.T., Poco, J.F. and LeMay, J.D., *A Comparison of Mechanical Properties and Scaling Law Relationships for Silica Aerogels and their Organic Counterparts*. MRS Proceedings, 1990. **207**: p. 197. doi:10.1557/PROC-207-197
- [154] Wong, J.C.H., Kaymak, H., Brunner, S. and Koebel, M.M., *Mechanical properties of monolithic silica aerogels made from polyethoxydisiloxanes*. Microporous Mesoporous Mater., 2014. **183**: p. 23-29. doi:10.1016/j.micromeso.2013.08.029
- [155] Steffens, K., Bialuschewski, D. and Milow, B., *Improving the properties of flexible hybrid-silica aerogels: addition of pores for a more lightweight material*, in *7th International Seminar on Aerogels*. 2022: Hamburg, Germany.
- [156] Steffens, K., Bialuschewski, D. and Milow, B., *Improving the properties of flexible hybrid-silica aerogels*, in *FEMS Junior EUROMAT 2022*. 2022: Coimbra, Portugal.
- [157] Loy, D.A., Baugher, B.M., Baugher, C.R., Schneider, D.A. and Rahimian, K., *Substituent Effects on the Sol–Gel Chemistry of Organotrialkoxysilanes*. Chem. Mater., 2000. **12**(12): p. 3624-3632. doi:10.1021/cm000451i
- [158] Malfait, W.J., Zhao, S., Verel, R., Iswar, S., Rentsch, D., Fener, R., Zhang, Y., Milow, B. and Koebel, M.M., *Surface Chemistry of Hydrophobic Silica Aerogels*. Chem. Mater., 2015. **27**(19): p. 6737-6745. doi:10.1021/acs.chemmater.5b02801
- [159] Nguyen, B.N., Meador, M.A.B., Tousley, M.E., Shonkwiler, B., McCorkle, L., Scheiman, D.A. and Palczer, A., *Tailoring Elastic Properties of Silica Aerogels Cross-Linked with Polystyrene*. ACS Applied Materials & Interfaces, 2009. **1**(3): p. 621-630. doi:10.1021/am8001617
- [160] Friebolin, H., *Basic one- and two-dimensional NMR spectroscopy*. 4. completely rev. and updated ed ed. 2005, Weinheim: Wiley-VCH.
- [161] Breitmaier, E., *Vom NMR-Spektrum zur Strukturformel organischer Verbindungen*. 3., vollst. überarb. und erw. Aufl ed. 2005, Weinheim: Wiley-VCH.
- [162] Malfait, W.J., Ebert, H.-P., Brunner, S., Wernery, J., Galmarini, S., Zhao, S. and Reichenauer, G., *The poor reliability of thermal conductivity data in the aerogel literature: a call to action!* J. Sol-Gel Sci. Technol., 2024. doi:10.1007/s10971-023-06282-9
- [163] Jiang, D.D., Yao, Q., McKinney, M.A. and Wilkie, C.A., *TGA/FTIR studies on the thermal degradation of some polymeric sulfonic and phosphonic acids and their sodium salts*. Polym. Degrad. Stab., 1999. **63**(3): p. 423-434. doi:10.1016/s0141-3910(98)00123-2

- [164] Jeon, B.J., Hah, H.J. and Koo, S.M., *Surface modification of silica particles with organoalkoxysilanes through two-step (acid-base) process in aqueous solution*. Journal of Ceramic Processing Research, 2002. **3**(3): p. 216-221.
- [165] Neugebauer, A., Chen, K., Tang, A., Allgeier, A., Glicksman, L.R. and Gibson, L.J., *Thermal conductivity and characterization of compacted, granular silica aerogel*. Energy and Buildings, 2014. **79**: p. 47-57. doi:10.1016/j.enbuild.2014.04.025
- [166] Cabot Corporation, *Datasheet - ENOVA® IC3110 AEROGEL*. 2021 [Retrieved September 19, 2024]; Available from: <https://www.cabotcorp.jp/-/media/files/product-datasheets/datasheet-enova-ic3110pdf.pdf>.
- [167] Emmerling, A. and Fricke, J., *Scaling Properties and Structure of Aerogels*. J. Sol-Gel Sci. Technol., 1997. **8**(1/2/3): p. 781-788. doi:10.1023/a:1018381923413
- [168] Scherer, G.W., Smith, D.M., Qiu, X. and Anderson, J.M., *Compression of aerogels*. J. Non-Cryst. Solids, 1995. **186**(1/2/3): p. 316-320. doi:10.1016/0022-3093(95)00074-7
- [169] Fener, R. and Niemeyer, P., *Flexible Komposite auf Basis von Aerogelen*, European Patent EP3042884B1, 2015.



## 7 Appendix

### 7.1 Nomenclature

#### 7.1.1 Abbreviations

AcOH	Acetic acid
AIBN	Azobis(isobutyronitril)
APD	Ambient pressure drying
CTAC	Cetyltrimethylammonium chloride
DEGDE	Diethylene glycol diethyl ether
DMDMS	Dimethyldimethoxysilane
EDET	2,2'-(ethylenedioxy)diethanethiol
EDX	Energy-dispersive X-ray spectroscopy
EPS	Expanded polystyrene
EtOH	Ethanol
FT-IR	Fourier-transform infrared spectroscopy
HFM	Heat flow meter
IPA	Isopropanol
JRC	Joint Research Centre
MTMS	Methyltrimethoxysilane
NMR	Nuclear magnetic resonance spectroscopy
PUR	Polyurethane
PVB	Polyvinylbutyrale
SCD	Supercritical drying
SEM	Scanning electron microscope
STA	Simultaneous Thermal Analysis
TEOS	Tetraethyl orthosilicate
TGA	Thermogravimetric analysis
TL	Transmission loss
TMAOH	Tetramethylammonium hydroxide
TMOS	Tetramethyl orthosilicate
VMDMS	Vinylmethyldimethoxysilane
VPA	Vinylphosphonic acid

VTMS	Vinyltrimethoxysilane
WHO	World Health Organization
XPS	Extruded polystyrene

### 7.1.2 Symbols

$D_{SEM}$	Particle diameter
$D_{TL}$	Sound transmission loss
$K_n$	Knudsen number
$l_g$	Mean free path
$p_c$	Capillary pressure
$\dot{Q}$	Heat flow
$S_r$	Radial shrinkage
$\theta_c$	Water drop contact angle
$\theta_p$	Contact angle in pore
$\rho_{bulk}$	Bulk density
$\rho_{env}$	Envelope density
$\rho_{skel}$	Skeletal density
$\sigma_{lg}$	Liquid gas interfacial tension
$D$	Pore diameter
$E$	Energy
$E$	Young's modulus
$R$	Pore radius
$\alpha$	Sound absorption coefficient
$\varepsilon$	Strain
$\lambda$	Thermal conductivity
$v$	sound velocity
$\Phi$	Porosity

## 7.2 List of Figures

Figure 1: Global market forecast for building thermal insulation, by region [4]. Source: Joint Research Centre (JRC) representation with data from Visiongain, 2017.....	1
Figure 2: Market value of acoustic insulation worldwide from 2017 to 2024 (in billion U.S. dollars), by region. [8].....	2
Figure 3: Common silicon alkoxide precursors tetramethyl orthosilicate (TMOS) and tetraethyl orthosilicate (TEOS). .....	5
Figure 4: Polar groups on the pore surface result in reversible shrinkage (“spring-back”) of the sample during/after drying. Reprinted from [37], with the permission from Elsevier.....	7
Figure 5: Chemical structure of precursors methyltrimethoxysilane (MTMS) and dimethyldimethoxysilane (DMDMS). .....	9
Figure 6: Chemical structure of precursors vinyltrimethoxysilane (VTMS) and vinylmethyldimethoxysilane (VMDMS). .....	10
Figure 7: Illustration of two-step thiol-ene click reactions for radical addition of VPA to VTMS containing monolithic aerogel.....	12
Figure 8: MTMS-based aerogel with notable flexibility allows easy handling. Reprinted from [42], with permission from Elsevier.....	16
Figure 9: Heat transport mechanisms in aerogel structures due to solid heat conduction, gaseous heat conduction and radiation. Figure in the style of [126]. .....	21
Figure 10: Scheme demonstrating sound reflection, sound absorption and sound transmission. The total incident sound energy is represented as incoming sound. ....	23
Figure 11: Schematic presentation of typical sound-absorbing mechanism in porous sound-absorbing materials. Reprinted from [134], with the permission of AIP Publishing LLC.....	24
Figure 12: Building thermal insulation global market forecast, by material type. [4] Source: JRC representation with data from Visiongain, 2017.....	25
Figure 13: Scanning electron microscope images derived from reference sample <b>a</b> and modified samples ( <b>b – i</b> ). The left column represents the “all”-series and the right column the “water”-series. The particle size decreased with increasing dilution.....	30
Figure 14: Image of 5.0 $\mu$ L water droplet on sample <b>a</b> . All calculated water drop contact angles are listed in Table 2. Further images of samples <b>b – i</b> are shown in the appendix (cf. Figure A 2).....	31
Figure 15: Thermal conductivity of samples in the temperature range of 0 – 60°C. The thermal conductivity is increased with increasing temperature. Diluted samples and standard ones did not differ much from each other. ....	32

Figure 16: Uniaxial stress-strain curve (left) and sample images of compression testing at 0% and 60% strain (right). After testing the samples spring back to their original height. More detailed single stress-strain curves are shown in the appendix (cf. Figure A 3) .....	33
Figure 17: Frequency-dependent sound absorption coefficient $\alpha$ of pure aerogel samples in the range of 50 – 2000 Hz. The absorption coefficient increased with increasing frequencies as expected.....	35
Figure 18: Frequency-dependent sound transmission loss of pure aerogel samples in the range of 50 – 2000 Hz. At 500 Hz the measurements of low frequency and high frequency were combined, resulting in small deviations at this point. The sample <b>d</b> showed the highest transmission loss values. The first resonance frequency of samples <b>a – b</b> could be observed at ~ 100 Hz and at 300 – 400 Hz for samples <b>c – g</b> . .....	36
Figure 19: Scanning electron microscope images derived from reference sample <b>a_f</b> and modified samples ( <b>b_f</b> , <b>c_f</b> , <b>f_f</b> , <b>g_f</b> ). The left column represents the “all”-series and the right column the “water”-series. ....	38
Figure 20: Photograph of 5.0 $\mu$ L water droplet on reference sample <b>a_f</b> . A water drop contact angle of 132° is determined for this sample. ....	38
Figure 21: Thermal conductivity of composite samples <b>a_f – c_f</b> in the temperature range of 0 – 60°C. The thermal conductivity increased with increasing temperature as expected. All samples showed similar values in the range of the measurement precision. ....	39
Figure 22: Uniaxial stress-strain-curve of composite samples <b>a_f – c_f</b> , <b>f_f</b> and <b>g_f</b> . More detailed single stress-strain curves are shown in the appendix (cf. Figure A 6). ....	40
Figure 23: Frequency-dependent sound absorption coefficient $\alpha$ of composite aerogel samples in the range of 50 – 2000 Hz. The absorption coefficient increased with increasing frequencies, as expected. ....	41
Figure 24: Frequency-dependent sound transmission loss of composite aerogel samples in the range of 50 – 2000 Hz. At 500 Hz, the measurements of low frequency and high frequency were combined, resulting in small deviations. The sample <b>a_f</b> with the highest mass showed the highest transmission loss values. The first resonance frequency of the samples could be observed at 200 – 300 Hz. ....	42
Figure 25: Comparison of envelope density for pure and composite aerogels. The higher the dilution, the lower the densities, as it was expected. Composite samples showed at the same dilution identical densities within their errors. ....	43

---

Figure 26: Comparison of thermal conductivity at 25°C for pure and composite aerogels. The change in densities did not influence the measured thermal conductivities, neither for pure aerogels (~ 32.5 mW m <sup>-1</sup> K <sup>-1</sup> ) nor for composite samples (~ 34.5 mW m <sup>-1</sup> K <sup>-1</sup> ).....	44
Figure 27: Comparison of Young's modulus E for pure and composite aerogels. Samples with lower densities showed lower Young's moduli in general. ....	44
Figure 28: Comparison of sound absorption (left) and transmission loss (right) of pure and composite aerogels in the measured range from 50 – 2000 Hz. The sound absorption coefficient for pure and composite samples did not differ a lot for the measured range. The sound transmission loss was measured for all samples in the same range. ....	45
Figure 29: SEM images of <b>V50</b> , <b>V50_Thiol</b> , and <b>V50_VPA</b> . The microstructure did not change with functionalization. Images of the <b>V05</b> - and <b>V10</b> -series can be found in the Appendix (Figure A 8 and Figure A 9). ....	48
Figure 30: <sup>13</sup> C-NMR spectra of samples <b>V50</b> , <b>V50_Thiol</b> , and <b>V50_VPA</b> (left) and expected chemical structures within the aerogel network (right).....	51
Figure 31: Digital image of sample <b>V50_VPA</b> after water drop contact angle measurement. The sample showed hydrophilic properties, so that no contact angle could be measured. ....	52
Figure 32: Uniaxial stress-strain-curve of sample-series <b>V05</b> , <b>V10</b> , and <b>V50</b> . More detailed single stress-strain curves are shown in the appendix (cf. Figure A 10). ....	53
Figure 33: Temperature profile during flame treatment. The outer temperature is measured at the side of the flame and the inner temperature within the monolith. The data was collected in an interval of 1 s. All samples reached high temperatures at the outside (> 600°C), at the inside only non-VPA-functionalized samples burned and therefore reached high temperatures there. ....	55
Figure 34: Photographic image of sample <b>V0</b> before fire testing. ....	56
Figure 35: Photographic images of samples <b>V0</b> , <b>V50</b> , <b>V50_Thiol</b> , and <b>V50_VPA</b> during and after fire testing. From left to right column: ignition, burning, right after burning (2x).....	56
Figure 36: Photographic images of samples <b>V50</b> (left) and <b>V50_VPA</b> (right) after fire treatment showing the inside of the samples. While the non-functionalized sample <b>V50</b> was totally black on the inside, the functionalized sample <b>V50_VPA</b> just showed a black surface and the inside was unaffected. ....	57
Figure 37: TGA- and DSC-curves of STA measurement for samples <b>V50</b> , <b>V50_Thiol</b> , and <b>V50_VPA</b> measured in inert gas conditions (argon). Residual masses of 88%, 74%, and 72% of its initial mass were obtained, respectively. ....	58

Figure 38: TGA-curves of samples <b>V05_VPA</b> , <b>V10_VPA</b> , and <b>V50_VPA</b> measured in inert gas conditions (nitrogen). The obtained curves followed the trend that higher vinyl content and, therefore, higher VPA content resulted in higher residual masses. ....	59
Figure 39: SEM images of samples <b>V0</b> , <b>V0_dil</b> , <b>V50</b> , <b>V50_dil</b> , <b>V100</b> and <b>V100_dil</b> . The microstructure is strongly influenced by the VTMS concentration as well as the dilution. The higher the VTMS concentration and the level of dilution, the smaller the particles. Since samples had no time for aging, the interparticle necks are not as pronounced as for monolithic samples with longer aging. ....	62
Figure 40: Particle size distribution particles synthesized with different VTMS and water concentrations. With increasing VTMS concentration, the particles got bigger, as well as with increasing dilution. Samples <b>V100</b> and <b>V100_dil</b> exceeded the device's measurement range of up to 2000 $\mu\text{m}$ . ....	63
Figure 41: Digital microscope images of sample <b>V100</b> (left) and <b>V100_dil</b> (right) at 20x magnification. The images demonstrate the bigger particles above 2000 $\mu\text{m}$ , which could not be measured with the particle size analyzer (marked red). ....	64
Figure 42: Thermal conductivity of particles compared to mat-shaped monoliths with different precursor-to-water ratios and different VTMS concentrations. Particles, in general, showed higher thermal conductivities than monoliths. ....	65
Figure 43: Thermal conductivity measured with HotDisk-method as a function of added granulate-emulsion mass. With increasing granulate content, the thermal conductivity increased. ....	68
Figure 44: Stress-strain curve of samples <b>AAC_0</b> – <b>AAC_15.0</b> . During compression, the composite samples broke. This can be observed in the poor shapes of the measured curves. During decompression, the samples reached 0 kPa stress at 15 – 20% residual strain, indicating that they did not recover to their original height. More detailed single stress-strain curves are shown in the appendix (cf. Figure A 15). ....	69
Figure 45: Schematic representation of the synthesis of pure aerogel samples. For composites, the prepared non-woven fabric is added to the screw container before addition of sol. Created with BioRender.com. ....	71
Figure 46: Schematic representation of the synthesis of vinyl-containing monolithic aerogel samples. Created with BioRender.com. ....	74
Figure 47: Schematic representation of the functionalization of vinyl-containing aerogel samples in a two-step process via thiol-ene click reaction mechanism. Created with BioRender.com. ....	74

- 
- Figure 48: Scheme of emulsion-gelation process. The sol acts as water-phase (W) and the n-hexane as oil-phase (O) in a (W/O)-emulsion. Created with BioRender.com. .... 76
- Figure 49: Photographs of HFM measurement frame for determination of thermal conductivity for particles made of expanded polystyrene. Left: frame with particles inside the HFM device; right: top-view of the particle-filled frame with inner dimensions of 120 x 120 x 20 mm<sup>3</sup>. ... 79
- Figure 50: Experimental setup for measuring the monolith's reaction to fire (left). Two sensors were used to measure the temperature during fire treatment at the surface and the inside of the monolith (right). .... 81

### 7.3 List of Tables

Table 1: Envelope and skeletal density of samples with their respective calculated porosity and measured radial shrinkage. The error of all skeletal density measurements is $\pm 0.01 \text{ g cm}^{-3}$ .	29
Table 2: Mean particle size calculated from SEM images and water drop contact angle determined by drop shape analyzer.	31
Table 3: Young's modulus $E$ calculated in the linear range of stress-strain-curves from 0 to 10% strain for samples <b>a – i</b> .	34
Table 4: Envelope and skeletal density of samples with their respective calculated porosity and measured radial shrinkage. The error of all skeletal density measurements is $\pm 0.01 \text{ g cm}^{-3}$ .	37
Table 5: Young's modulus $E$ calculated in the linear range of stress-strain-curves from 0 to 10% strain for samples <b>a_f – c_f</b> and <b>f_f – g_f</b> .	40
Table 6: Envelope and skeletal density of unfunctionalized VTMS containing samples with their respective calculated porosity and measured radial shrinkage. The error of all skeletal density measurements is $\pm 0.01 \text{ g cm}^{-3}$ .	46
Table 7: Envelope and skeletal density of VTMS containing samples after the first functionalization step with their respective calculated porosity. The error of all skeletal density measurements is $\pm 0.01 \text{ g cm}^{-3}$ .	47
Table 8: Envelope and skeletal density of VTMS-containing samples after the second functionalization step with their respective calculated porosity and measured radial shrinkage. The error of all skeletal density measurements is $\pm 0.01 \text{ g cm}^{-3}$ .	47
Table 9: Elemental analysis from energy-dispersive X-ray spectroscopy (EDX) measurements of samples <b>V50</b> , <b>V50_Thiol</b> , and <b>V50_VPA</b> .	49
Table 10: Adjusted values from elemental analysis via EDX (Exp.) and calculated theoretical composition (Theor.) of the samples <b>V50</b> , <b>V50_Thiol</b> , and <b>V50_VPA</b> at estimated reaction rates of 100%. The difference (Diff.) of experimental to theoretical value was calculated.	50
Table 11: Water drop contact angle determined by drop shape analyzer for sample-series <b>V05</b> , <b>V10</b> , and <b>V50</b> .	52
Table 12: Thermal conductivity of sample series <b>V05</b> , <b>V10</b> , and <b>V50</b> at 20°C measured with HotDisk method.	53
Table 13: Young's modulus $E$ calculated in the linear range of stress-strain curves from 0 to 10% strain for sample-series <b>V05</b> , <b>V10</b> , and <b>V50</b> .	54
Table 14: Bulk and skeletal density of samples with their yield. The error of all skeletal density measurements is $\pm 0.02 \text{ g cm}^{-3}$ .	61
Table 15: Particle size distribution and its D-values calculated from Figure 40.	63



---

Table 16: Envelope and skeletal density of samples <b>AAC_0</b> – <b>AAC_20.0</b> with their respective calculated porosity and measured radial shrinkage. The error of the skeletal density measurements is $\pm 0.01 \text{ g cm}^{-3}$ . .....	67
Table 17: Young’s modulus $E$ calculated in the linear range of stress-strain curves from 0 to 10% strain for samples <b>AAC_0</b> – <b>AAC_15.0</b> . .....	69
Table 18: Synthesis recipes for 380 g (~ 350 mL) of total solution for reference sample ( <b>a</b> ) and modified samples ( <b>b</b> – <b>i</b> ). Samples <b>b</b> , <b>d</b> , <b>f</b> , and <b>h</b> represent the “dilution all”-series; samples <b>c</b> , <b>e</b> , <b>g</b> , and <b>i</b> represent the “water”-series. ....	72
Table 19: Synthesis recipes for 200 g (~ 180 mL) of total solution for reference sample ( <b>a_f</b> ) and modified samples ( <b>b_f</b> , <b>c_f</b> , <b>f_f</b> , <b>g_f</b> ). Samples <b>b_f</b> and <b>f_f</b> represent the “all”-series; samples <b>c_f</b> and <b>g_f</b> represent the “water”-series. ....	73
Table 20: Synthesis recipes for 525 g (~ 500 mL) of total solution for vinyl-based monoliths with substitution of 5, 10, and 50 mol% of MTMS for VTMS. All samples were gelated and aged for one day. ....	75
Table 21: Synthesis recipes for ~ 20 mL of total solution for reference sample and modified samples. ....	77
Table 22: Synthesis recipes for ~ 100 mL of total solution for reference sample ( <b>AAC_0</b> ) and modified samples( <b>AAC_2.5</b> , <b>AAC_5.0</b> , <b>AAC_10.0</b> , <b>AAC_15.0</b> , <b>AAC_20.0</b> ). The sol was distributed into five closed containers for gelation. ....	78

## 7.4 Experimental Results

### 7.4.1 Dilution of Precursors

#### 7.4.1.1 Pure Aerogels



Figure A 1: Samples with increasing dilution of the precursor system (left to right). The sample dimensions are around 35 mm in diameter.

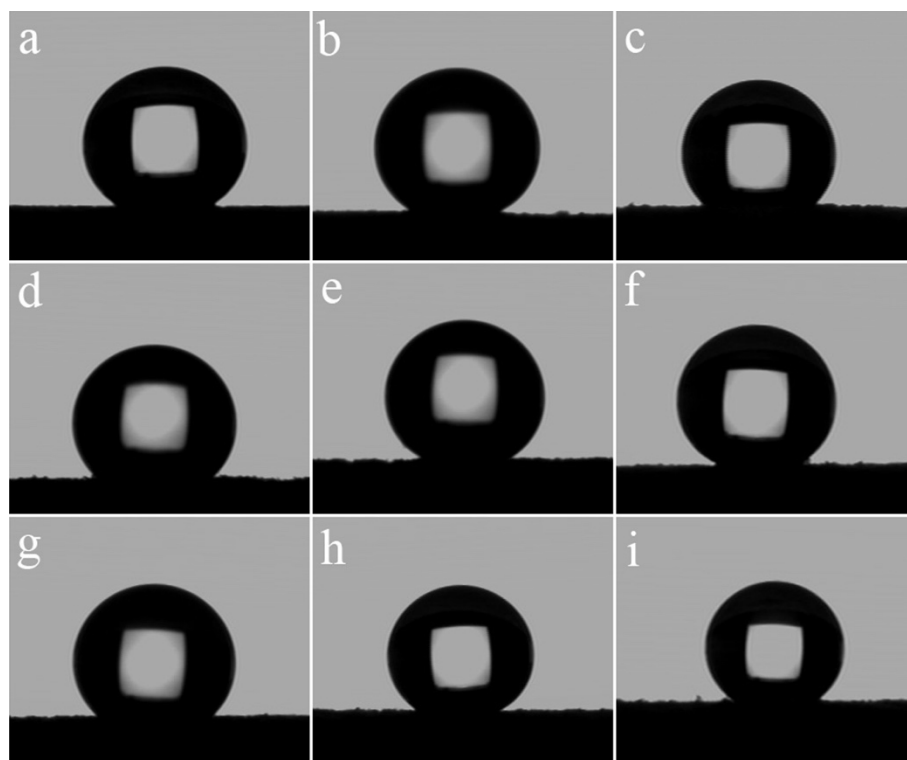


Figure A 2: Image of 5.0  $\mu\text{L}$  water droplet on samples a - i.

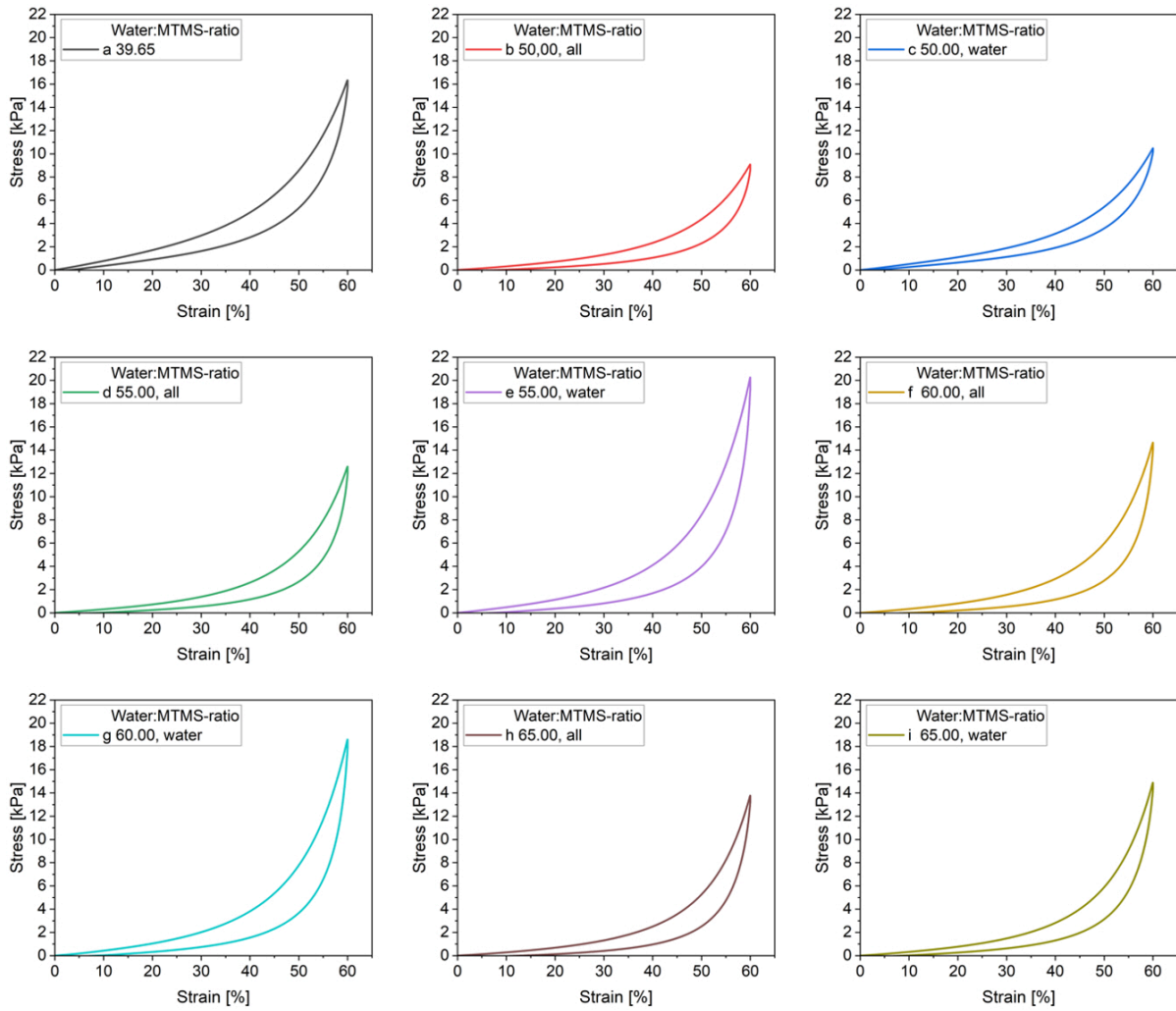


Figure A 3: Detailed single stress-strain-curves of samples *a* – *i* from Figure 16.

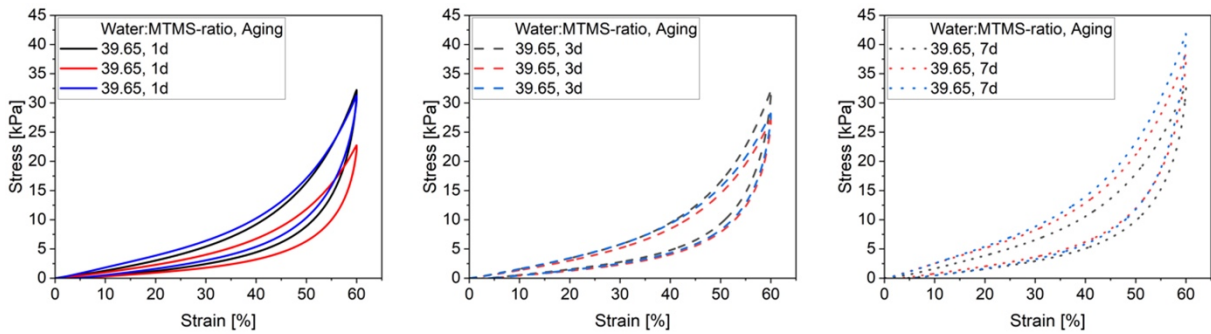


Figure A 4: Stress-strain-curves of reference samples *a* with one, three and seven days of aging respectively. Each curve represents one sample tested.

## 7.4.1.2 Aerogel Composites

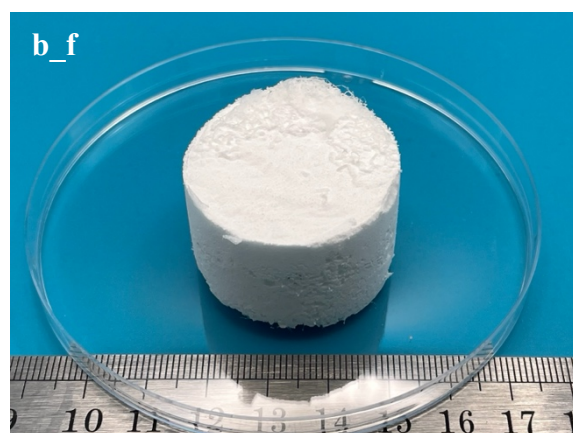


Figure A 5: Photographic image of sample fiber reinforced composite sample *b\_f*.

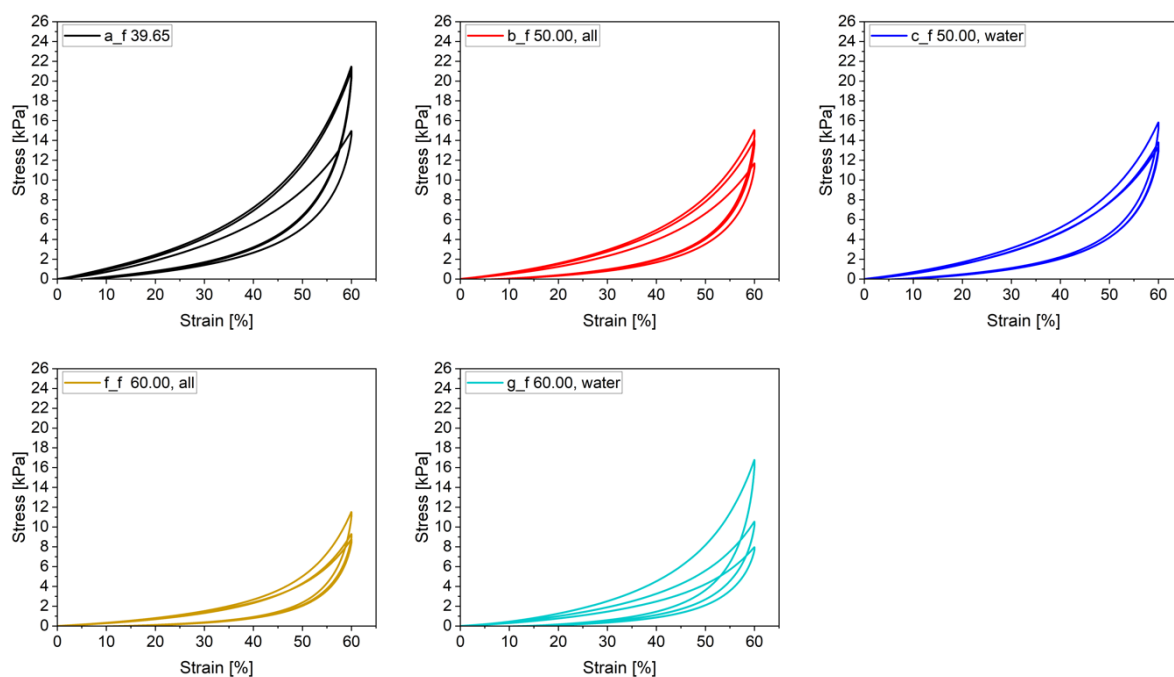


Figure A 6: Detailed single stress-strain-curves of samples *a\_f* – *g\_f* from Figure 22.

## 7.4.2 Vinyl Modification of Hybrid Aerogels

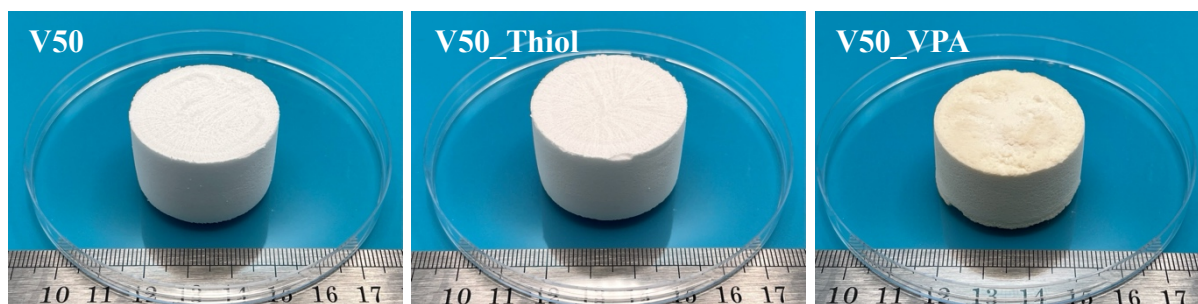


Figure A 7: Photographic images of samples *V50*, *V50\_Thiol* and *V50\_VPA*.

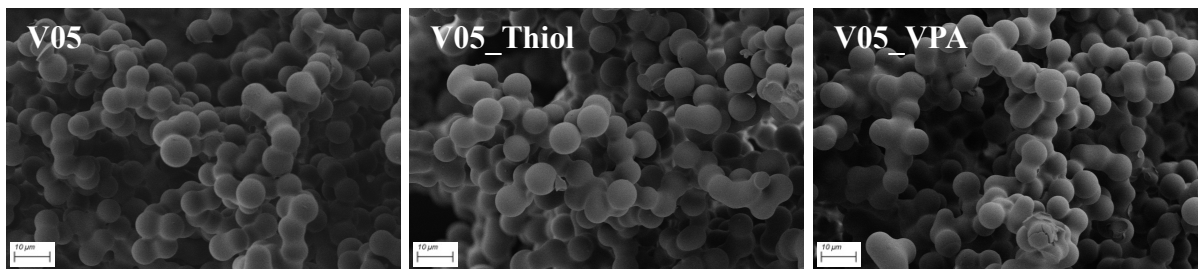


Figure A 8: SEM images of *V05*, *V05\_Thiol* and *V05\_VPA*.

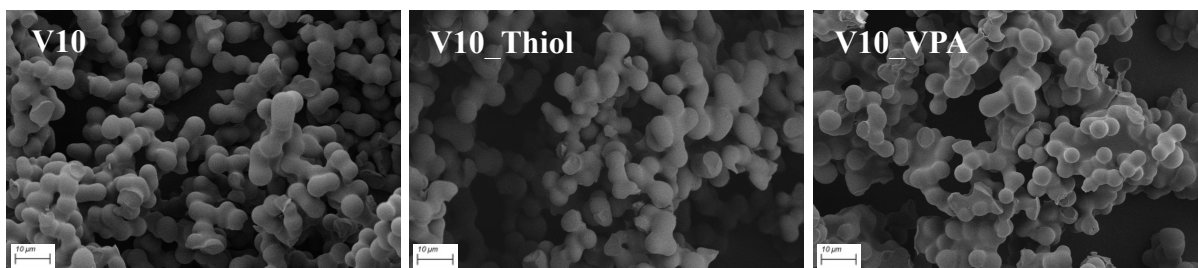


Figure A 9: SEM images of *V10*, *V10\_Thiol* and *V10\_VPA*.

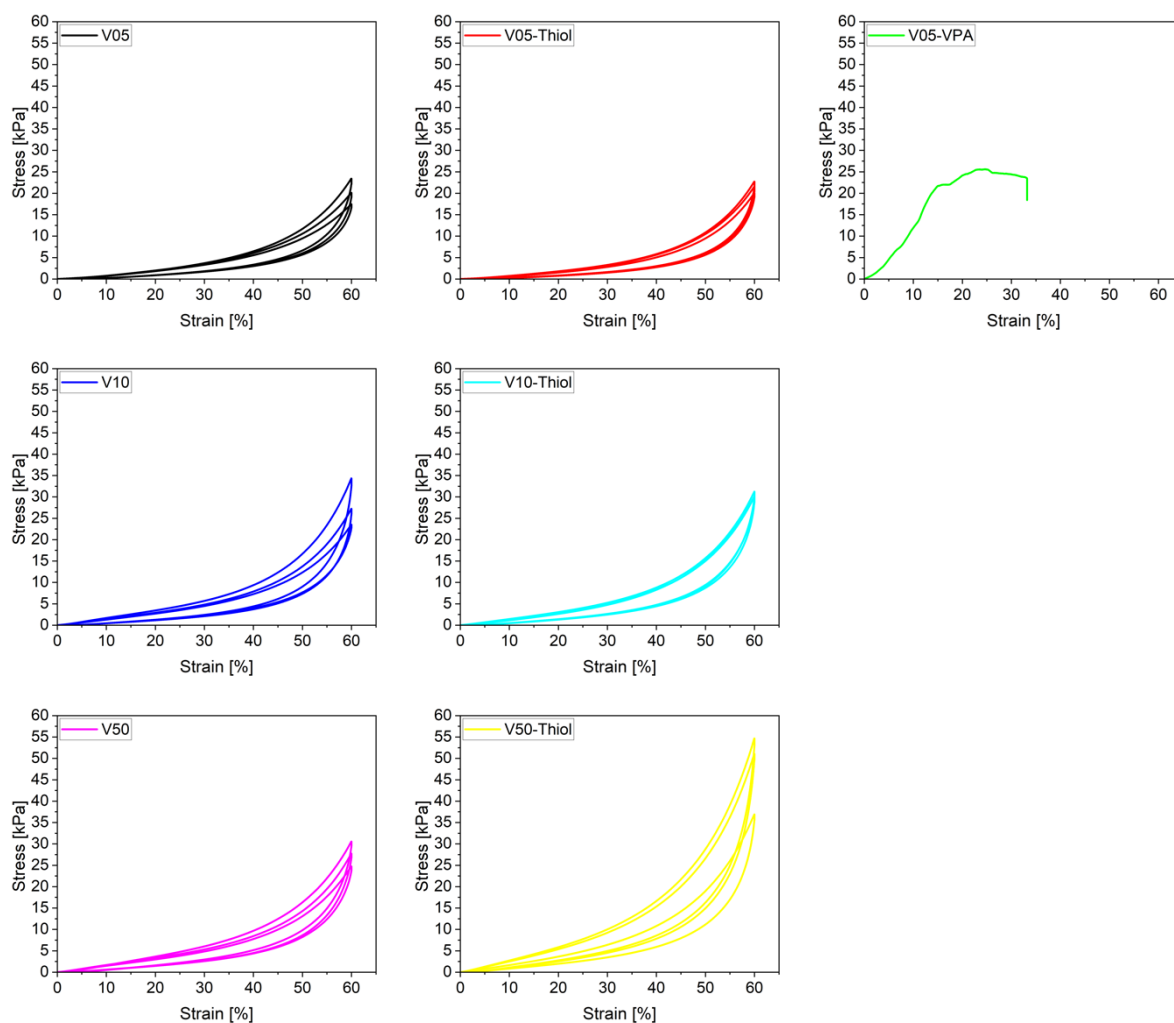


Figure A 10: Detailed single stress-strain-curves of sample series *V05*, *V10* and *V50* from Figure 32.

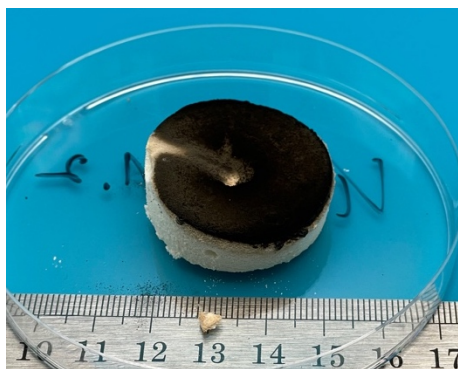


Figure A 11: Photographic image of sample V50\_VPA after fire testing (cut in half before ignition). Still the protective layer formed and no change after fire testing could be observed.

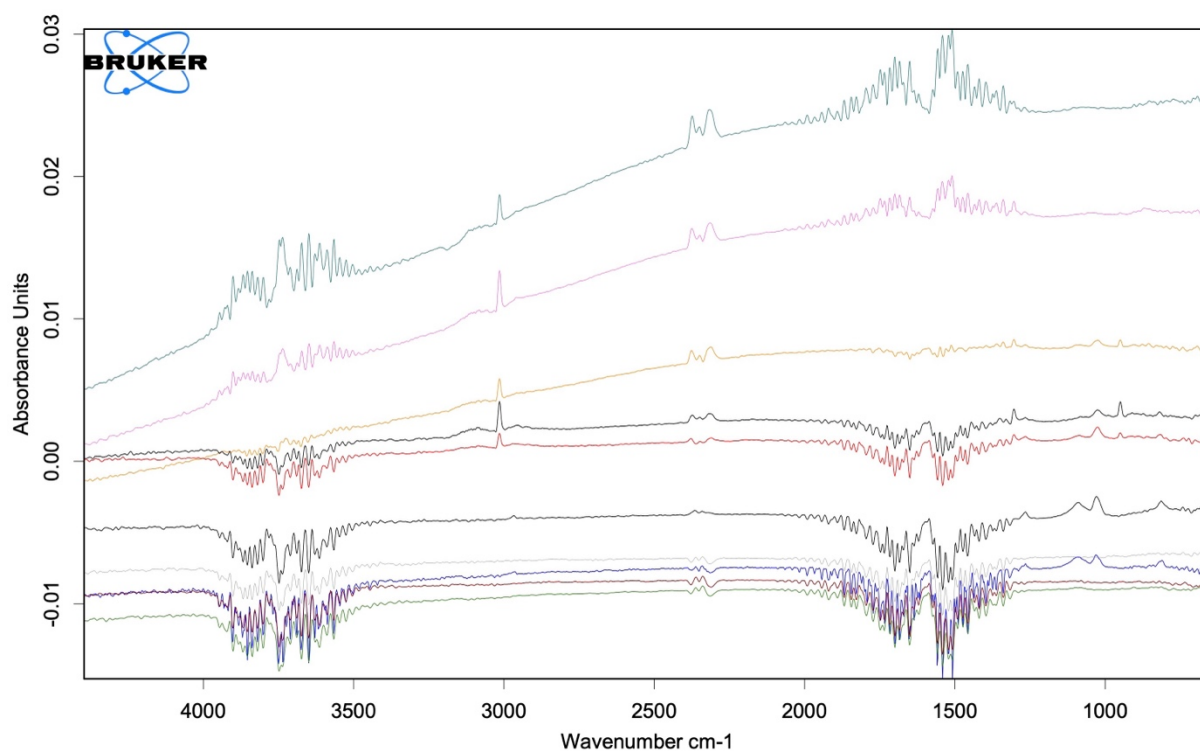


Figure A 12: Resulting IR-signals from sample V50\_VPA during STA measurement at several temperatures (80 – 800°C). It was not possible to identify specific combustion products.

### 7.4.3 Synthesis of Particles

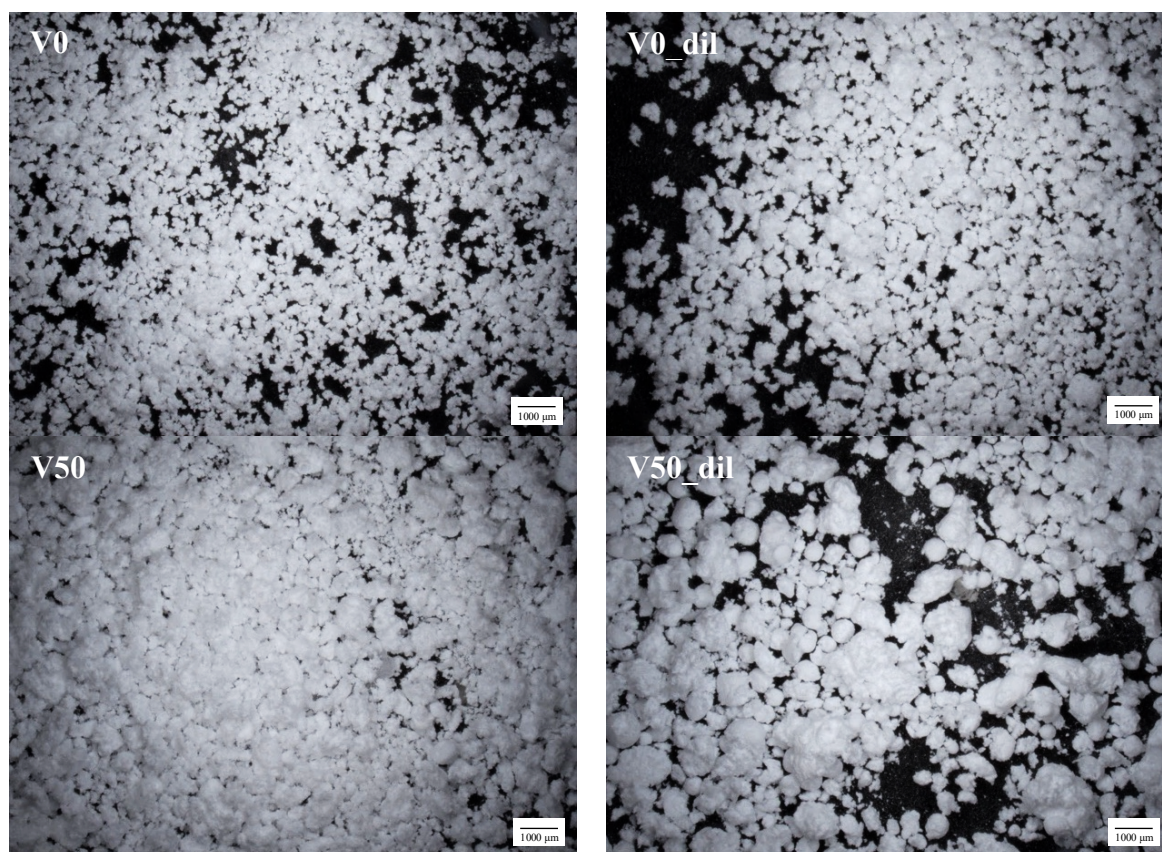


Figure A 13: Digital microscopic images of samples V0, V0\_dil, V50 and V50\_dil at 20x magnification.

### 7.4.4 Silica Aerogel-Aerogel Composites

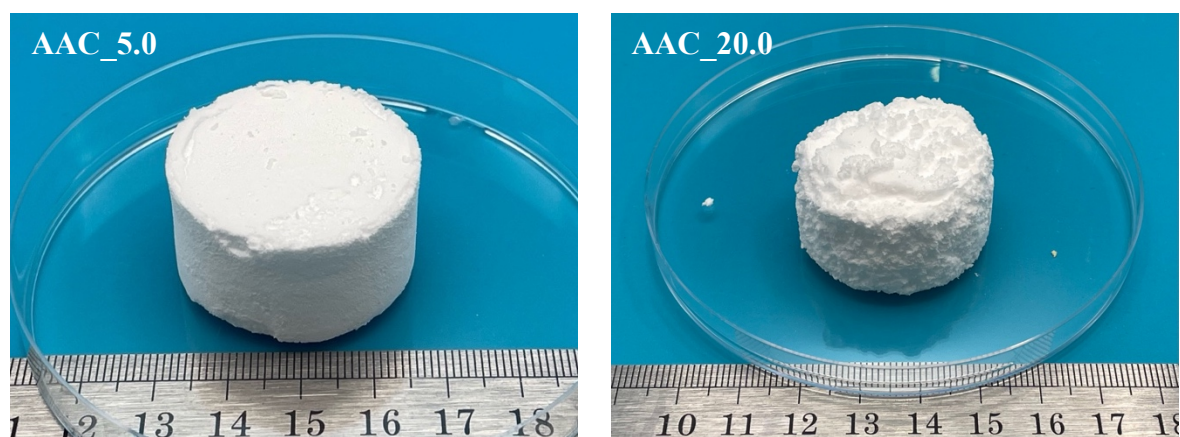


Figure A 14: Sample image of AAC\_5.0 and AAC\_20.0.

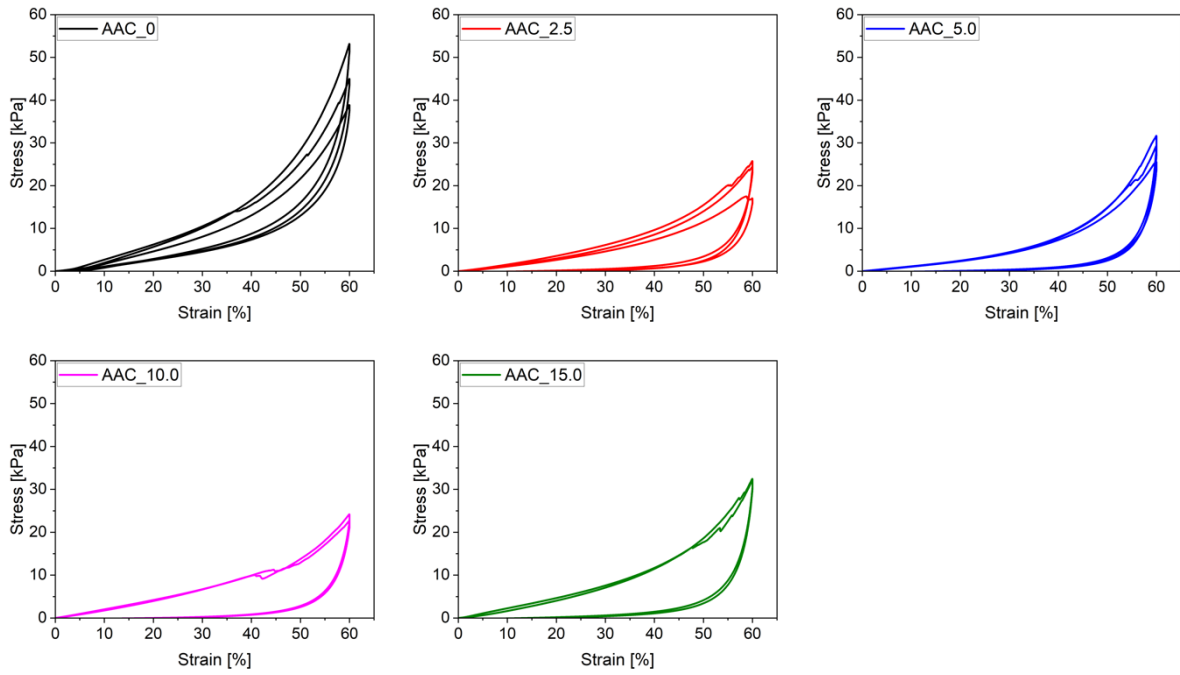


Figure A 15: Detailed single stress-strain-curves of sample series AAC\_0 – AAC\_15.0 from Figure 44.

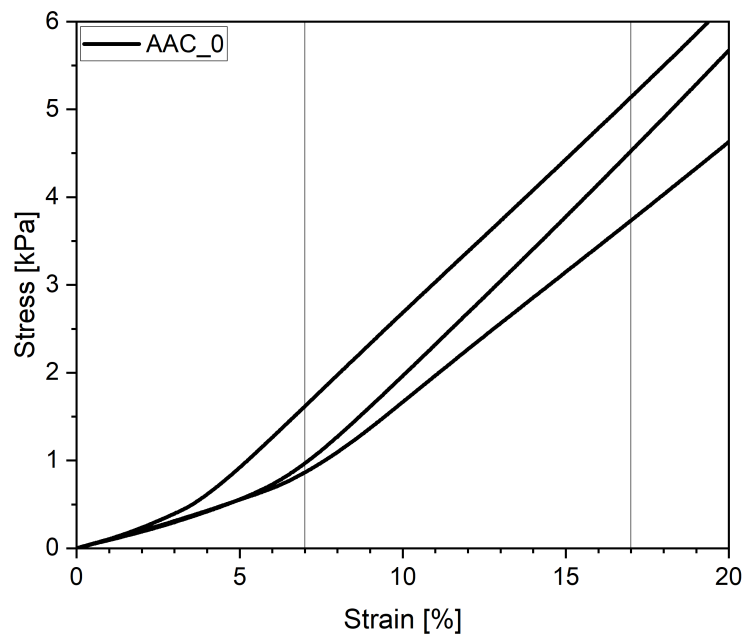


Figure A 16: Detailed stress-strain curve of sample AAC\_0 with focus on the lower strain range for calculation of the Young's modulus.



## 7.5 Eidesstattliche Erklärung

Hiermit versichere ich an Eides statt, dass ich die vorliegende Dissertation selbstständig und ohne die Benutzung anderer als der angegebenen Hilfsmittel und Literatur angefertigt habe. Alle Stellen, die wörtlich oder sinngemäß aus veröffentlichten und nicht veröffentlichten Werken dem Wortlaut oder dem Sinn nach entnommen wurden, sind als solche kenntlich gemacht. Ich versichere an Eides statt, dass diese Dissertation noch keiner anderen Fakultät oder Universität zur Prüfung vorgelegen hat; dass sie - abgesehen von unten angegebenen Teilpublikationen und eingebundenen Artikeln und Manuskripten - noch nicht veröffentlicht worden ist sowie, dass ich eine Veröffentlichung der Dissertation vor Abschluss der Promotion nicht ohne Genehmigung des Promotionsausschusses vornehmen werde. Die Bestimmungen dieser Ordnung sind mir bekannt. Darüber hinaus erkläre ich hiermit, dass ich die Ordnung zur Sicherung guter wissenschaftlicher Praxis und zum Umgang mit wissenschaftlichem Fehlverhalten der Universität zu Köln gelesen und sie bei der Durchführung der Dissertation zugrundeliegenden Arbeiten und der schriftlich verfassten Dissertation beachtet habe und verpflichte mich hiermit, die dort genannten Vorgaben bei allen wissenschaftlichen Tätigkeiten zu beachten und umzusetzen. Ich versichere, dass die eingereichte elektronische Fassung der eingereichten Druckfassung vollständig entspricht.

Teilpublikationen:

Christiane Gillner, Boris Dilba, Sören Keuchel, Olgierd Zaleski, Christian Wischmann, Daniele Usai, Wolfgang Gleine, Adam Dzierbinski, Pascal Vöpel, Kai Steffens, Danny Bialuschewski, Barbara Milow, *Numerische Untersuchung eines neuartigen Kabinenwandkonzeptes*. Tagungsband - Proceedings "Fortschritte der Akustik - DAGA 2024": DAGA 2024 - 50. Jahrestagung für Akustik, 18. - 21. März 2024, Hannover

Kai Steffens, Danny Bialuschewski und Barbara Milow, *Tuning density and morphology of organic-inorganic hybrid-silica aerogels through precursor dilution for lightweight applications*. J. Sol-Gel Sci. Technol., 2024. **112**(3): S. 768-775. doi:10.1007/s10971-024-06572-w

Datum, Name und Unterschrift

05.10.2024

Kai Steffens

---

### **7.6 Zugänglichkeit von Daten und Materialien**

Die Dissertation beinhaltet die Gewinnung von Primärdaten oder die Analyse solcher Daten oder die Reproduzierbarkeit der in der Dissertation dargestellten Ergebnisse setzt die Verfügbarkeit von Datenanalysen, Versuchsprotokollen oder Probenmaterial voraus. Die Daten sind auf den Laufwerken des Rechenzentrums der Universität zu Köln gesichert (inklusive Backups), sowie die hergestellten Proben archiviert, und den Personen der Abteilung Nanostrukturierte Zelluläre Materialien (AK Milow) zugänglich (entsprechend den Vorgaben der Erstbetreuerin).

## 7.7 *Curriculum Vitae*

### PERSÖNLICHE DATEN

Kai Steffens

\*18.08.1996 in Mechernich

kaisteffens@icloud.com

### AUSBILDUNG

Promotion: Chemie, 2021 - 2024

Universität zu Köln, Institut für Anorganische Chemie, AK Prof. Milow - Köln

- Entwicklung neuer Syntheseroutinen von silicabasierten Aerogelverbundwerkstoffen

Master of Science: Materials Science and Sustainability Methods, 2018 – 2020

Hochschule Bonn-Rhein-Sieg - Rheinbach

- Abschlussarbeit: Thermooxidative Alterung von Polyalphaolefinen

Bachelor of Science: Chemie mit Materialwissenschaften, 2015 – 2018

Hochschule Bonn-Rhein-Sieg - Rheinbach

- Abschlussarbeit: Einfluss verschiedener Syntheseparameter auf die Eigenschaften unterkritisch getrockneter RF-Aerogele
- Nachhaltigkeits-Zertifikat "Blaue Schiene" des Fachbereichs Angewandte Naturwissenschaften

Allgemeine Hochschulreife: 2007 – 2015

Gymnasium Am Turmhof – Mechernich

### AUSLANDSAUFENTHALTE

Forschungsaufenthalt: 01/2023 – 02/2023

Universität Nagoya & Universität Kyoto – Nagoya/Kyoto, Japan

- Gemeinsame Forschung mit den Arbeitsgruppen von Prof. Nakanishi und Prof. Kanamori
- Dauer: 3 Wochen

### WISSENSCHAFTLICHE FACHKONFERENZEN & WORKSHOPS

- Posterpräsentation, "10th NRW Nano Conference" in Dortmund
- Posterpräsentation, "6th International Seminar on Aerogels" in Hamburg
- Posterpräsentation, "Junior Euromat 2022" in Coimbra, Portugal
- Posterpräsentation, "Cologne Graduate School PhD Symposium" in Köln
- Posterpräsentation, "2nd PhD Workshop & 30th ATC Conference" in Frankfurt am Main
  
- Workshop "Applied Industrial Innovation Management"
- Workshop "Python for Non-Programmers and Scientific Libraries"
- Workshop "Leadership Starter Kit"